VIBRATION AND STRUCTURAL RESPONSE OF HYBRID WIND TURBINE BLADES

A Thesis

by

NORIMICHI NANAMI

Submitted to the Office of Graduate Studies of
Texas A&M University
in partial fulfillment of the requirements for the degree of

MASTER OF SCIENCE

December 2010

Major Subject: Mechanical Engineering

Vibration and Structural Response of Hybrid Wind Turbine Blades

VIBRATION AND STRUCTURAL RESPONSE OF HYBRID WIND TURBINE BLADES

A Thesis

by

NORIMICHI NANAMI

Submitted to the Office of Graduate Studies of
Texas A&M University
in partial fulfillment of the requirements for the degree of

MASTER OF SCIENCE

Approved by:

Chair of Committee,	Ozden Ochoa
Committee Members,	Alan Palazzolo
	Thomas Strganac
Head of Department,	Dennis O'Neal

December 2010

Major Subject: Mechanical Engineering

ABSTRACT

Vibration and Structural Response of Hybrid Wind Turbine Blades. (December 2010)

Norimichi Nanami, B.E., Nihon University, Japan

Chair of Advisory Committee: Dr. Ozden Ochoa

Renewable energy is a serious alternative to deliver the energy needs of an increasing world population and improve economic activity. Wind energy provides better environmental and economic benefits in comparison with the other renewable energy sources. Wind energy is capable of providing 72 TW (TW = 10^{12} W) of electric power, which is approximately four and half times the world energy consumption of 15.8 TW as reported in 2006. Since power output extracted from wind turbines is proportional to the square of the blade length and the cube of the wind speed, wind turbine size has grown rapidly in the last two decades to match the increase in power output. As the blade length increases, so does its weight opening up design possibilities to introduce hybrid glass and carbon fiber composite materials as lightweight structural load bearing alternatives.

Herein, we investigate the feasibility of introducing modular composite tubulars as well as hybrid sandwich composite skins in the next generation blades. After selecting a target energy output, 8 MW with 80 m blade, airfoil geometry and the layup for the skin as well as internal reinforcements are proposed. They are incorporated into the computational blade via linear shell elements for the skin, and linear beam elements for

the composite tubulars to assess the relationship between weight reduction and structural performance. Computational simulations are undertaken to understand the static and dynamic regimes; specifically, displacements, stresses, and vibration modes. The results showed that the composite layers did not exhibit any damage. However, in the balsa core of the sandwich skin, the von Mises stress exceeded its allowable at wind speeds ranging from 11.0 m/sec to 12.6 m/sec. In the blades with composite tubular reinforcement, two different types of damage are observed: a. Stress concentrations at the tubular-skin attachments, and b. Highest von Mises stress caused by the flapping bending moment. The vibration studies revealed a strong coupling mode, bending and twist, at the higher natural frequencies of the blade with tubular truss configuration. The weight saving measures in developing lighter blades in this study did not detract from the blades structural response for the selected load cases.

ACKNOWLEDGEMENTS

First of all, I would like to thank Dr. Ozden Ochoa for giving me an opportunity to conduct this research. I have been greatly pleased to work under her guidance. Also, she has inspired and motivated me to work towards my academic goals. Working with her has been one of the most fantastic academic experiences for me.

I would also like to thank Dr. Alan Palazzolo and Dr.Thomas Straganac for serving on my committee and taking their valuable time to discuss this research with me.

Thanks also go to my past and present lab mates, Melanie, Douglas, Seung Min, Vince, Hieu, Mandar, Ozgu, and Jeungwoo, for providing their help and guidance during my master's program.

I can never forget my friends, Matt, and Kee Han, who have been influence on my research. They have always been with me, and I don't have enough words to appreciate them.

I really appreciate my Texas family, the Pilant family, provided valuable suggestions with the thesis and helped me to adapt to life in US. I cannot find any words to describe their hospitality during my time at College Station.

Finally, I dedicate this master's research to my parents who have physically and mentally supported me to study in the US. I would not have been able to complete my master's program without their encouragement and support through my academic career. I express my deepest respect and gratitude for their support and understanding.

TABLE OF CONTENTS

Page

Page

LIST OF FIGURES

FIGURE Page

FIGURE Page

FIGURE Page

LIST OF TABLES

1. INTRODUCTION

1.1 Overview

Renewable energy is a variable alternative to supply the energy needs of an increasing world population and improve economic activity. The Energy Information Administration (EIA) [1] estimates that between 2006 and 2030, global energy consumption will increase by 44%. In 2006, the Organization for Economic Co-operation and Development (OECD) member countries accounted for 51% of world energy consumption with their energy use expected to increase by 0.6% annually. Energy use of the emerging non-OECD nations is expected to grow at 2.3% per year over the same time period [1].

Although construction expense, unstable availability of wind, bird strike, and noise have been limitations, wind energy still provides better environmental and economic benefits in comparison with the other energy sources [2-4]. Wind energy is capable of providing 72 TW (TW = 10^{12} W) of electric power which is approximately four and half times the world energy consumption of 15.8 TW in 2006 [1,5]. The U.S. Department of Energy (DOE) reports that if wind energy contributed 20% of the US electricity supply, it would reduce carbon dioxide emissions from electricity generation by 25%, cumulative water use in the electric sector by 8%, and natural gas use by 11% through 2030 [6]. In fact, development of wind turbines will be a significant key factor to satisfy the prospective energy demand.

This thesis follows the style and format of *Journal of Composite Materials.*

Wind turbine size has grown rapidly in the last two decades resulting in proportionally greater power output (Figure 1.1). Electrical power extracted from a wind turbine is proportional to the square of the blade tip radius (Figure 1.2) and to the cube of the wind speed (u_w). The rotor diameter in Figure 1.1 is twice the blade length which is referred as tip radius. Furthermore, the electrical power is dependent on a power coefficient of a wind turbine which indicates an efficiency to extract the electrical power from the power contained in the air stream. The theoretical maximum value of the power coefficient is approximately equal to 0.593, which is known as the Betz limit [7]. As stated by Eggleston *et al.* [8], practically the maximum power coefficient of wind turbines with the smooth airfoil blades is about 0.45, and the power coefficient of 0.3 to 0.35 can be viewed as a good design. Since wind speed increases with elevation, the increasing wind turbine tower height (Figure 1.1) enables expanding the blade tip radius to improve energy production. In addition to the wind turbines presented in Figure 1.1, the most powerful wind turbines with a blade tip radius of 63 m are already in operation, and generate 7.5 MW nominal power output [9].

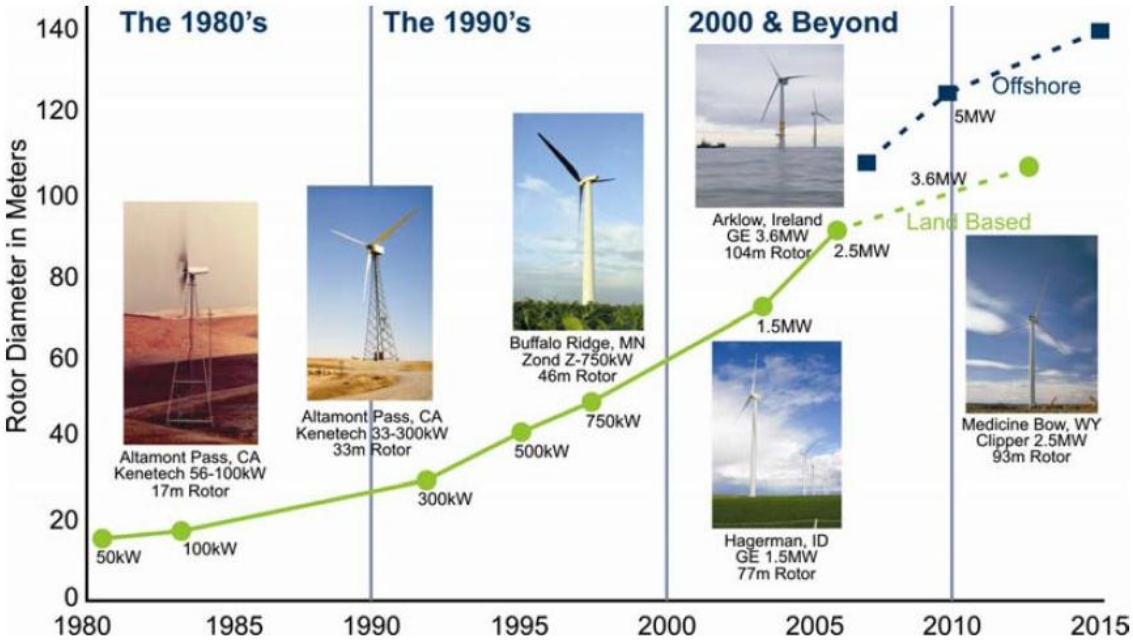

Figure 1.1. Development path and growth of wind turbine power output [6].

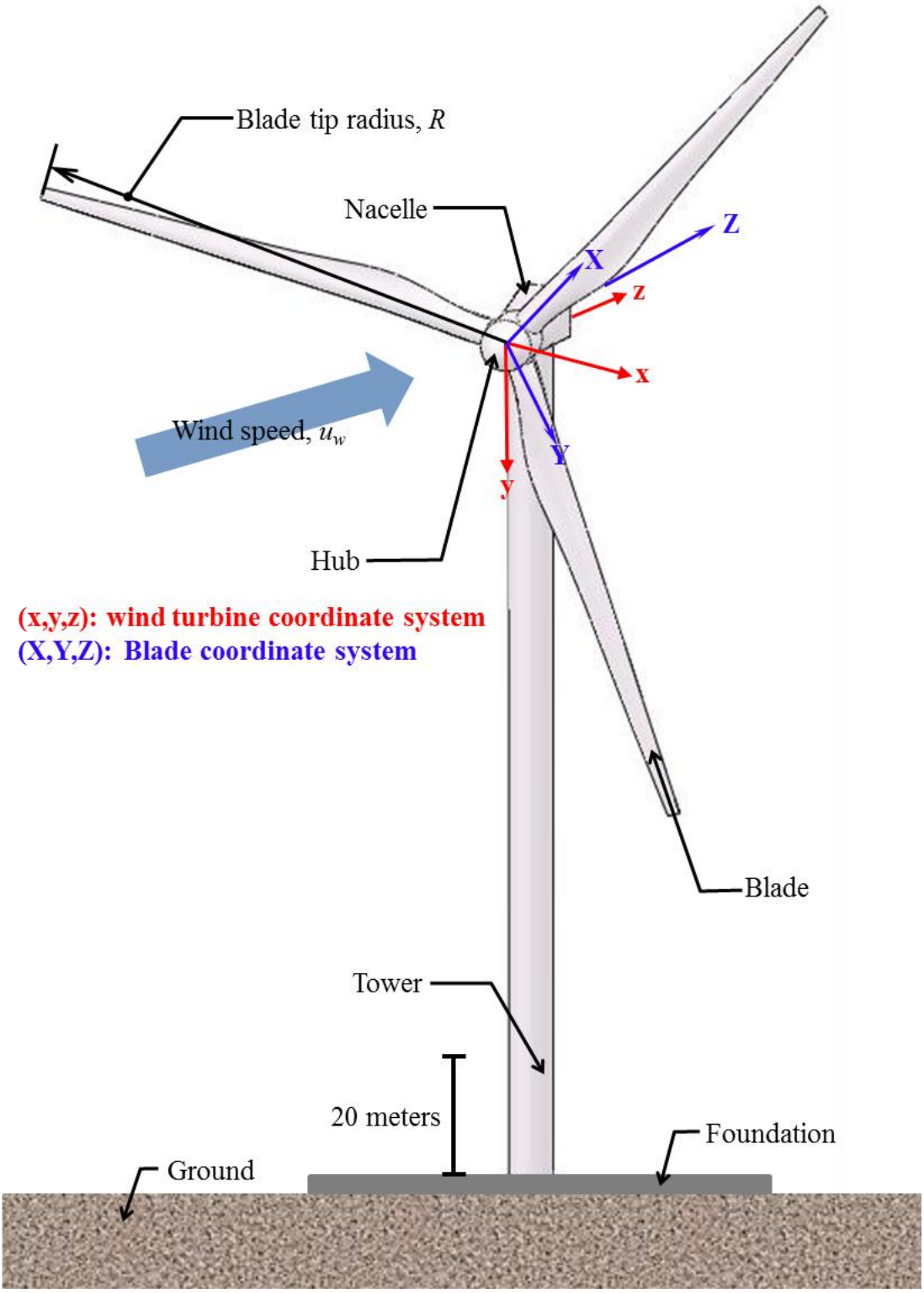

Figure 1.2. Schematic of a typical HAWT.

Wind turbines are composed of a foundation, tower, nacelle, hub, and two or three blades. Figure 1.2 shows a schematic of a typical horizontal-axis wind turbine (HAWT) as an upwind land-based construction. The global (x,y,z) coordinate system as well as the blade (X,Y,Z) coordinate system originates the center of the hub. The blades are attached to the hub at an angle to the plane of rotation (x-y plane). The hub includes the blade pitch control unit which can actively adjust this angle to mitigate the aerodynamic forces [7]. The z-axis is designated as the rotational axis of the blades, which turn in a counterclockwise direction. The foundation is designed to prevent the tower from overturning under extreme wind conditions. The tower supports the nacelle, hub, and blades. Mechanical and electrical components such as gearbox, generator, brake, drive train, and control unit are all housed in the nacelle.

As blade length increases, blade weight increases exponentially. Data depicting this behavior can be found in technical reports available in open literature [6, 10-12]. In commercial blade designs, the weight scale is at an exponent of about 2.53 [12]. Therefore, hybrid carbon and glass fiber reinforced composite materials are of significant interest to save weight and increase specific stiffness and strength.

Utilization of carbon fibers (CF) in large wind turbine blades enables a thinner and more efficient blade profile along with a stiffer and more slender blade, and reduced weight. This also results into an increased in material costs. It is observed that even with composite materials, these blades are extremely heavy, also reinforcement architecture such as tape and fabric laminates affect the material damping and damage tolerance

[13,14]. Therefore, the focus of this research is to reduce blade weight without compromising static and dynamic behavior.

1.2 Literature Review

1.2.1 Wind Turbine Blade Design

A typical blade is composed of cylindrical and airfoil cross-sections (Figure 1.3). The cylindrical section is located near the blade root, where the blade is attached to the hub by means of metallic bolts [15]. The blade is internally reinforced to maintain the original shape of the airfoil during operation. The airfoil sections belong to the rest of the blade and determine the aerodynamic performance. The selection of appropriate cross-section profile, taper angle, and twist angle plays an important role in sustaining aerodynamic forces. Although existing laminar airfoils such as NACA (National Advisory Committee for Aeronautics) airfoils were historically used for the blade design until the 1980s, low-drag airfoils are being developed at various institutes such as National Renewable Energy Laboratory (NREL) in the US, Delft University of Technology in Netherland, Riso National Laboratory in Denmark, etc. to specifically measure the performance of wind turbines [16-22].

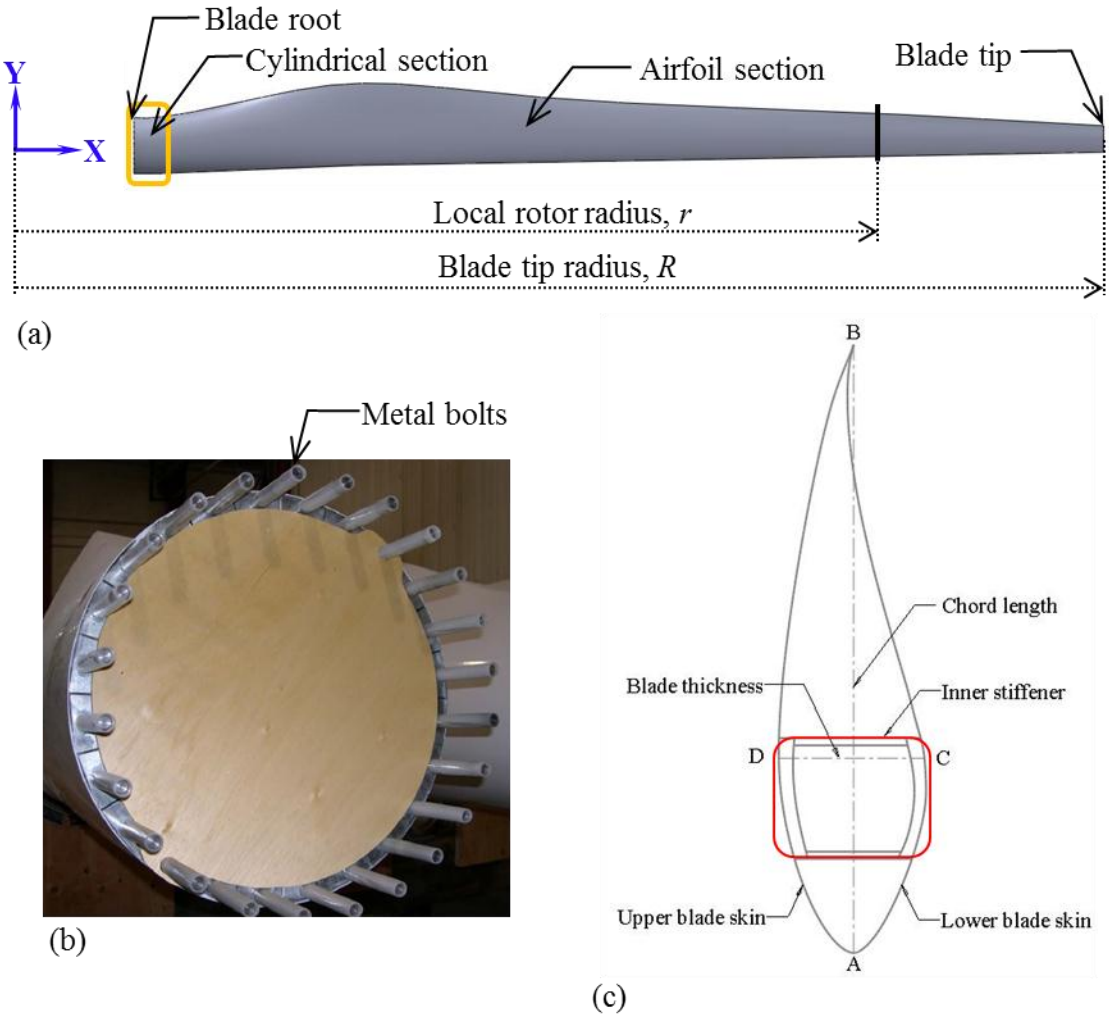

Figure 1.3. Geometrical description of the blade: (a) wind turbine blade, (b) the cylindrical section [15], and (c) airfoil cross-section.

Typically, the blade has an upper and a lower blade skin, and internal stiffeners (Figure 1.3(c)). The skins are usually of sandwich constructions to resist buckling. Either glass fiber reinforced polymers (GFRP) or carbon fiber reinforced polymers (CFRP) are utilized for the face of sandwich constructions while polymeric foams, balsa wood, or

honeycomb type are taken as the core materials [23]. For instance, the thickness ratio of the core to the face in such sandwich constructions is 10:1 [24].

Internal construction of the blades may take the form of a box girder, coupled double box, spar cap box, single shear web, or double shear webs [4,10,23,25-27]. Figure 1.4 presents the cross-section of a typical design where the box girder is the internal stiffener. The box girder and the blade skin are manufactured separately and then bonded together in a separate process.

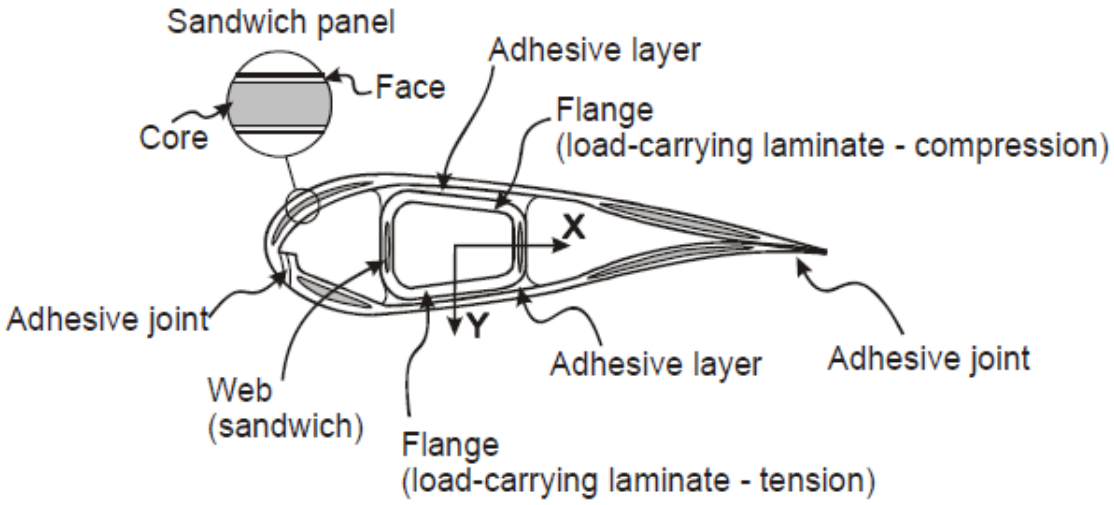

Figure 1.4. Typical design detail of the box girder [10].

In spar cap and shear web construction (Figure 1.5), the spar caps are manufactured with the blade skin and then bonded to the shear webs. They are located between the excess of the blade root and the vicinity of the blade tip. Spar caps play the

same role as the flanges of the box girder. Similarly, shear webs resist the flapping shear deformation [23]. Spar cap laminates are generally UD glass fiber/polyester, and glass laminates are reinforced polymer (GRP) shear webs. The skin is made of continuous strand mats (CSM) of glass. The skin toward the trailing edge is sandwich constructions consisting of PVC foam as core and CSM as face sheets [4]. Also, some hybrid carbon fiber and glass fiber (CF/GF) reinforcement of either tape and/or fabric composite is employed in the construction of the spar caps [24,28].

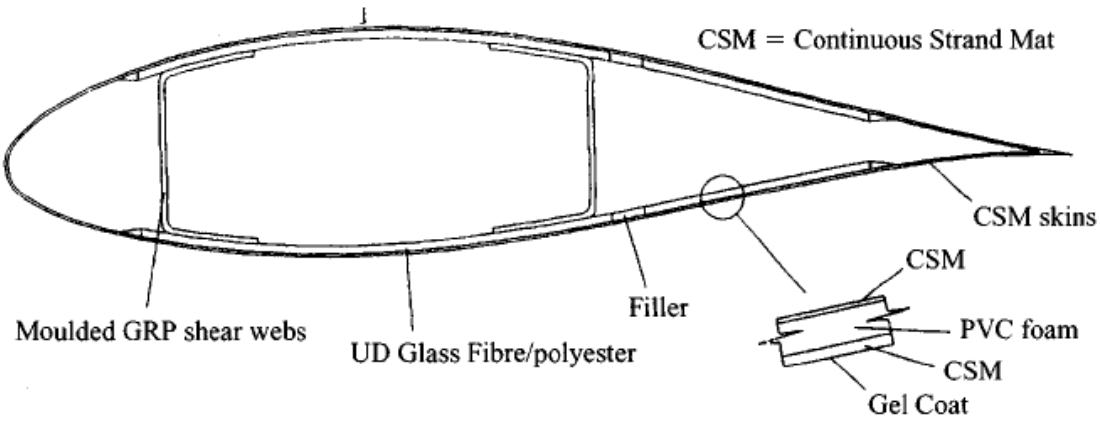

Figure 1.5. Example design of spar caps and shear webs construction [4].

The chord length and blade thickness (Figure 1.3(c)) are based on the size of the blade tip radius. For example, blade tip radii of 5 MW offshore wind turbines range from 50 m to 70 m (Figure 1.1) [6]. Tip blade radius of 80 m and 95 m is, respectively, expected to define 8 MW and 12 MW [29]. Griffin [11,30,31] reported non-dimensional

chord length and twist angle distributions for blades with 40 m to 60 m blade tip radii with NREL S818/825/826 airfoil family. Chord length is normalized with respect to the blade tip radius, and the chord length at the local rotor radius is presented. Blade thickness at the local rotor radius can be determined by the corresponding chord length multiplied by a specific fraction. However, this fraction for the blade thickness varies based on airfoil selection [16,18]. In addition, 5 m tapered and twisted blades with NREL S809 airfoil are manufactured and tested to generate reasonable data of a wind turbine [32].

Today wind turbine blade manufacturers develop their proprietary technology design concept and manufacturing process. Due to the complex shape of the blade, various techniques such as modified filament winding, prepregs with vacuum assisted resin transfer molding (VARTM) and resin infusion molding are adapted to manufacture large blades [10]. Compared with the other wet lay-up approach, the latter two technologies provide manufacturing advantages such as controlling and obtaining constant material properties with high specific stiffness and strength [10].

1.2.2 FEA Blade Models: Geometry and Load

Generally, the blade is modeled with shell elements with offset nodes, shell elements with mid-plane nodes, or combined shell/solid elements. Their aspect ratios for linear and quadratic elements are below 2 and 12, respectively. The shell elements with offset nodes are physically located on the outer surface of the blade skin representing the actual blade. The shell elements with mid-plane nodes correspond to the mid-planes of

the various laminates in the cross-section leading to discontinuous skin surface. In the combined shell/solid model, the solid elements are used to model sandwich cores in the skin and web. They are also used to model adhesive bonds between the skin and spar cap, upper skin and the lower skin, and the web and spar cap. The shell elements are employed for other material parts such as sandwich faces in the skin and web, and spar caps. This blade model is extremely beneficial for the local blade analyses to save running and modeling time. The experimental and numerical comparison of results for blade displacements and rotations reveals the combined shell/solid model with the best agreement for flapping-bending and torsion cases. All three computational blade models give the same results in the edgewise-bending behavior and are in good agreement with the experimental results [33, 34]. Laird *et al.* [35] used layered shell elements with mid-plane nodes in their FEA models and got more accurate solutions in torsion cases.

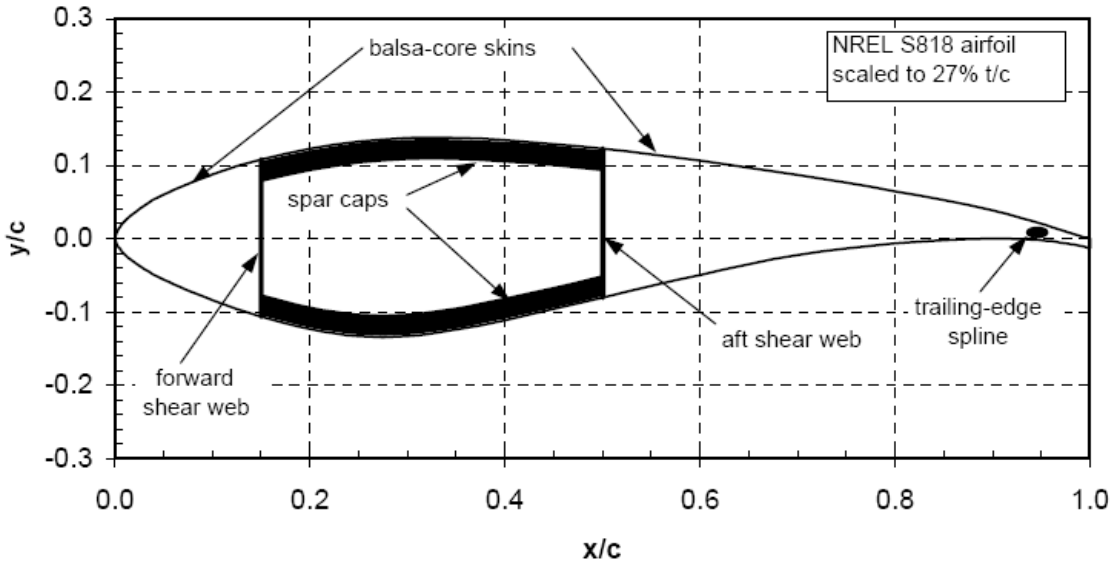

Figure 1.6. Architecture of computational blade model [11,30,31].

Griffin [11,30,31] selected the computational blade geometry as shown in Figure 1.6 for his analyses. The blade skin toward the leading and trailing edge and shear webs is sandwich constructions utilizing triaxial glass fabric (GF) and balsa core. This triaxial fabric of 1.27 mm is employed for the face sheet with 25%, 25%, and 50% distribution of +45°, -45°, and 0° fibers, respectively. Thickness of balsa cores in the forward blade skin and aft blade skin are about 0.5% and 1% of the chord length, respectively. Balsa cores in the shear webs are 1% of the chord in thickness. The spar caps are E-glass/epoxy laminate, and this stacking sequence results in a spar cap laminate with 70% UD and 30% off-axis fibers by weight. The thicknesses of the spar caps are 0%, 5%, or 10% of the blade thickness.

Bending loads due to aerodynamic forces and gravitational loads due to the rotation of the blade have more impact on the design loads than inertia, operation, and torsional loads [23]. Aerodynamic loading conditions are defined by wind turbine standards such as IEC 61400-1 [36]. The loads are obtained at the point when the blade is brought to a standstill due to high wind speed. For this case, the 50-year extreme gust wind speed is considered. The loading conditions are derived from computational fluid dynamics simulations or formulas for aerodynamics, and then are applied in static analyses [24,31]. Also, aerodynamic forces for the rotating blade are employed in the blade analyses [37].

1.2.3 Analytical Results

De Goeij *et al.* [27] concluded from their FEA results that the highest strains appeared near the leading edge of the CF/GF hybrid composite blade due to reversed fiber angle orientations. They suggested that one more layer with distinct fiber orientation can be added to the initial laminate in the blade skin to avoid this phenomenon.

The flexural rigidity and torsional rigidity of the composite blade were estimated based on simple bending theory for a cantilever in conjunction with FEA. Estimation of the rigidity is used to model the equivalent beam of the blade, and dynamic response of the blade beam model is predicted under fluctuating load conditions such as wind gusts. Also, tower strikes could be considered since the blade striking the tower might be damaged unless the blade provides sufficient rigidity against its deflection [38,39]. Mohamed and Wetzel [28] calculated flapwise and edgewise flexural rigidity for the hybrid composite blade by applying the equivalent beam model. The area moments of inertia were obtained based on the actual blade geometry at the local rotor radius, and material properties were extracted from modeling of laminates employed in the blade.

Buckling resistance of the blade is provided in references [23,26,40-42]. Berggreen *et al.* [40-42] investigated buckling strength of glass/epoxy panels utilized in the blade. The ultimate failure loads of the panels generally decreased as imperfections of the panel increased. Local buckling and instant failure of panels arose from large and deep delaminations. The smaller delaminations closer to the surface of the panels showed stable growth. Jensen *et al.* [26] studied structural behaviors of a 34 m wind

turbine blade in the elastic and plastic phase. They identified the failure modes causing ultimate collapse. Flapping bending caused a non-linear deformation, which is called ovalization, in the box girder. The crushing pressure generated by the ovalization strongly increased the web deflections. Additionally, the rotational stiffness of the corners of the box girder was significantly important to avoid ovalization, the so-called Brazier effect, and also provided rich buckling resistances to the flanges. Similarly, the rotational stiffness of the joints between the spar caps and webs was crucial in the blade design. Since the flanges of the box girder and spar caps in the main spar design were usually made as monolithic composite laminates, the long blade may not have very large stiffened monolithic shallow shell caps. The unstiffened parts are sensitive to failure in local buckling. Also, the presence of imperfection produced throughout the manufacturing process dominated the local buckling mode of failure [23].

Vibration modes of the blade are described by Burton *et al.* [4]. Transverse modes of the blade are in the flapwise and edgewise directions as well as torsional modes. The domain of the exciting frequencies for the typical blades with high torsional stiffness is known to be lower than the torsional natural frequency of the blade.

Mezyk *et al.* [37] investigated the influences of four different lay-up - S-type and E-type fiber glass, Technora, and Kevlar - to dynamic properties of a blade with NACA 63-212 airfoil. Its undamped natural frequencies were obtained from modal analyses. In comparison among these materials, a lower density material has higher undamped natural frequencies and larger deflections. Saravanos *et al.* [43] predicted damped natural frequencies for the glass/epoxy blade with beam element in FEA. They predicted

and measured modal frequencies and modal loss factors for 35m wind turbine blades. A good correlation between predicted data and experimental data is achieved.

1.3 Objective and Approach

The objective of this research is to explore computationally concepts to reduce overall weight of a hybrid composite wind turbine blade. The feasibility of introducing modular composite tubulars to replace the traditional shear webs will be considered with various airfoil and composite architecture for 80 m tip radius blade. Computational simulations are undertaken to understand the static and dynamic regimes. Specifically, displacements, stresses, and vibration modes are assessed.

2. COMPUTATIONAL APPROACH

Computational techniques are practical means to predict static and dynamic behaviors of the blade during the design stage leading to savings in time, testing, and construction costs. Computational simulations in this research are performed in ABAQUS, a general-purpose finite element analysis (FEA) software.

2.1 Element Selection

The blade is represented with shell elements that follow the mid-plane shell formulation. For simplicity, beam elements are adopted for composite tubulars to allow and accelerate parametric studies.

2.1.1 Shell Elements

The shell element library in ABAQUS is categorized as having general-purpose, thin-only, and thick-only shell elements. General-purpose shell elements can provide solutions for both thick and thin shell problems. Thin-only and thick-only shell elements are valid for use with thin and thick shell problems, respectively. Typically, sandwich composite constructions have very low transverse shear stiffness since their core is softer than their face [44]. Therefore, general-purpose shell elements have been selected for this research.

Of the two types of general-purpose shell elements, conventional and continuum, available in ABAQUS, this research uses conventional shell elements. Shell thicknesses

in blade models are significantly smaller than other global in-plane dimensions. Global in-plane dimensions are identified as the blade tip radius, chord length, blade thickness, or the radius of curvature. Conventional shell elements discretize a reference surface by defining the element's planar dimensions, its normal surface, and its original curvature. Although the nodes of the shell element do not exist throughout the shell thickness, this thickness is defined through section properties. Also, the stresses throughout the shell thickness are assumed to be negligible.

Conventional shell elements can be utilized for both thin and thick shell problems. Thin shell problems described by classical (Kirchhoff) shell theory assume that transverse shear deformation is small enough to be negligible; i.e. the transverse shear strains are equal to 0, the Kirchhoff constraint. Upon thick shell problems described by shear flexible (Mindlin) shell theory (Appendix A), their transverse shear deformation affects the solution significantly. Since an additional kinematic constraint is involved in the Mindlin shell theory, this theory is acceptable for both thick and thin shell problems.

The validity of using shell theory can be checked with a slenderness ratio definition. For linear elastic materials, the slenderness ratio is defined as

$$\frac{K_{\alpha\alpha}\, l^2}{D_{(\alpha+3)(\alpha+3)}} \tag{2.1}$$

where $K_{\alpha\alpha}$ denotes transverse stiffness matrix, $D_{(\alpha+3)(\alpha+3)}$ a section stiffness matrix, α =1or 2 (no sum on α), and l is a characteristic length on the surface of the shell

structures. Note that the characteristic length (l) is independent of the element's characteristic length. The ratio can be used as a guideline to determine whether the assumption that plane sections must remain plane has been satisfied. If the ratio is greater than 100, shell theory is generally adequate. However, shell theory will probably not give sufficiently accurate results if the ratio has smaller values than 100. The $K_{\alpha\alpha}$ and $D_{(\alpha+3)(\alpha+3)}$ can be given through a data check analysis [44].

Consequently, the blades of various geometric and material specifications are represented with three-dimensional linear shell elements (S3R and S4R) of ABAQUS, which are conventional shell elements under the general-purpose shell element category suitable for nonlinear geometrical analyses. S3R is a 3-node, trilateral, stress/displacement, shell element. S4R is a 4-node, quadrilateral, stress/displacement, shell element. These elements have three displacement and three rotational degrees of freedom (DOF). These elements allow finite strain, arbitrarily large rotations, and transverse shear deformation, and use reduced integration to form their element stiffness; their mass and force matrixes are integrated exactly.

2.1.2 Beam Elements

Two kinds of beam theory are well known: Euler-Bernoulli beam theory and Timoshenko beam theory. In the Euler-Bernoulli beam theory, it is assumed that the traverse plane sections of the beam remain plane and normal to its longitudinal axis before and after its bending. This beam theory is valid for small deformation problems that disregard shear deformations. However, first-order shear deformations are taken into

account in the Timoshenko beam theory (Appendix A). This beam theory is suitable for both small and large deformation problems. Therefore, composite tubulars are represented with linear Timoshenko beam elements (B31H). The elements are employed with hybrid formulation to overcome the difficulty associated with computing the axial and shear forces due to large rotations.

2.2 Material Behaviors

2.2.1 Elastic Properties

Elastic properties of materials have to be entered in computational analyses. Since the shell elements are capable of defining each ply in laminates, overall laminate stiffness can be calculated before or during the analyses. Homogenized elastic properties of typical composite materials such as GF/epoxy and CF/epoxy have been documented in the literature [45-47]. A linear elastic stress-strain constitutive relationship, the Generalized Hooke's law, is incorporated in these materials.

However, because ABAQUS does not allow stacking plies in the beam elements, the overall elastic properties for the laminated tubulars need to be incorporated in the simulations. Thus, the effective properties of the tubulars are obtained based on 3D constitutive equations and classical laminated plate theory (Appendix B).

2.2.2 Damage Initiation

For ductile isotropic materials such as balsa wood, the von Mises yield criterion is employed to evaluate their initial damage [48]. Due to the simulations based on the

shell theory, the von Mises stress for in-plane problems is shown in Equation (2.2). When the von Mises stress exceeds the allowable strength of the materials, the materials are found to be initially damaged.

$$\sigma_y = \sqrt{\hat{\sigma}_{11}^{\ 2} + \hat{\sigma}_{22}^{\ 2} - \hat{\sigma}_{11}\hat{\sigma}_{22} + 3\hat{\tau}_{12}^{\ 2}} \tag{2.2}$$

where σ_y denotes the von Mises stress and $\hat{\sigma}_{11}, \hat{\sigma}_{22}, \hat{\tau}_{22}$ the components of the effective stress tensor.

Many local failure modes are possible in composite materials prior to their final failures. The first local failure can be considered as damage initiation. The damage is progressive, and additional local failures are demonstrated until the final failures. For simplicity of simulation, this research focuses on damage initiation.

To predict damage initiation, Hashin failure criteria are selected for fiber-reinforced composite materials to identify different damage modes: fiber tension, fiber compression, matrix tension, and matrix compression (Appendix C) [44,49,50]. The in-plane stress fields in the local material coordinates are used in these criteria.

2.3 Static Analyses

2.3.1 Loading and Constraint Conditions

The three rotations and three displacements are constrained at the blade root as shown in Figure 2.1. Lift and drag forces are dependent on wind speed. Their maximum values usually occur at nominal wind speed (12-15 m/sec). The Z component of forces resulting from lift and drag forces (dP_Z) is applied to the lower surface of the blade, and

the Y component of the resultant forces (dP_Y) is applied both to the lower and upper surfaces (Figure 2.1).

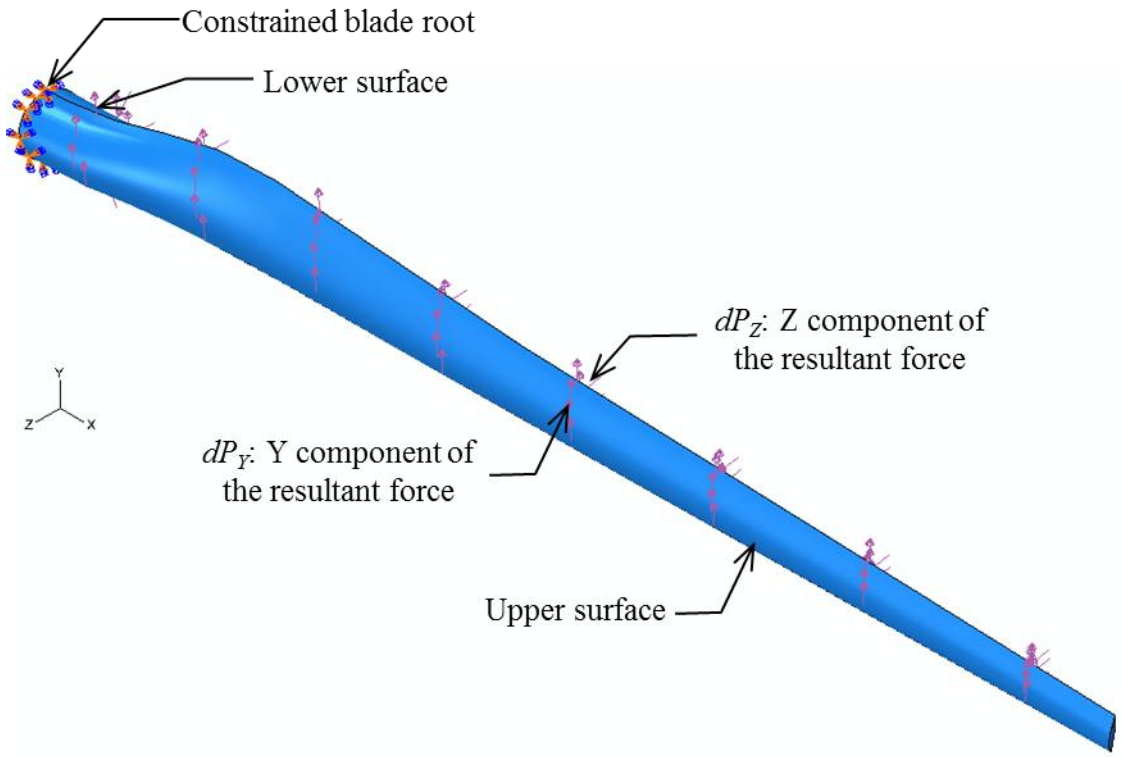

Figure 2.1. Boundary conditions for static analyses in the blade models.

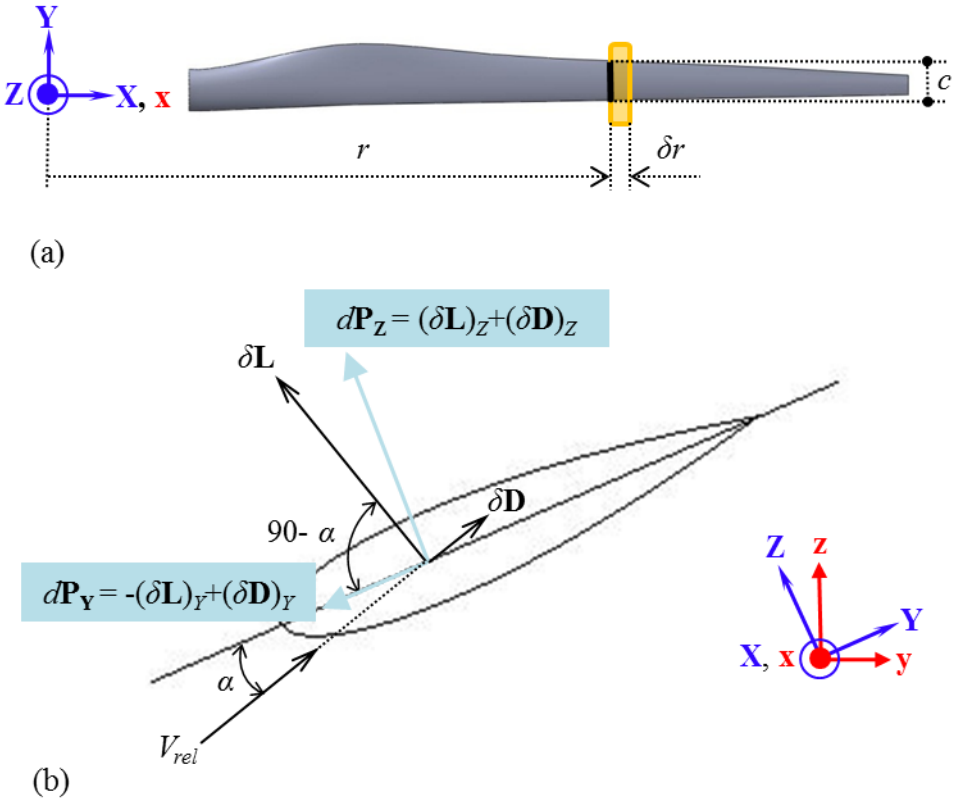

Figure 2.2. (a) An infinitesimal blade element, and (b) forces on the airfoil.

Lift and drag forces of an infinitesimal blade element are calculated using two-dimensional airfoil characteristics. Velocity along the blade length and three-dimensional effects are ignored. When the X-axis of the blade is aligned with the x-axis of the wind turbine (Figure 1.2), lift ($\delta\mathbf{L}$) and drag ($\delta\mathbf{D}$) forces for the rotating blade with an angle of attack (α) appear as shown in Figure 2.2. The contribution of lift forces along the y-axis enables the blade to rotate, and the decomposed component of the drag forces along the y-axis acts on the blade to resist its rotation. Resultant relative wind velocity

(V_{rel}) for the rotating blade can be represented by Equation (2.3) where u_{ta} is tangential air flow velocity, it acts in the direction opposed to the tangential velocity of the blade (u_{ta}) [4]. Wind speed (u_w) is aligned to the z-axis of the wind turbine.

$$V_{rel} = \sqrt{u_w^2 + u_{ta}^2} \tag{2.3}$$

Lift forces normal to a resultant relative wind velocity (V_{rel}) and drag forces parallel to a resultant relative wind velocity are given by

$$\frac{\delta L}{c\delta r} = \frac{1}{2}\rho_{air} V_{rel}^2 C_l \tag{2.4}$$

and

$$\frac{\delta D}{c\delta r} = \frac{1}{2}\rho_{air} V_{rel}^2 C_d \tag{2.5}$$

where c is a chord of the infinitesimal blade element, δr blade length of the infinitesimal blade element, ρ_{air} an air density, C_l a lift coefficient, and C_d a drag coefficient [4]. Air density is selected to reflect tower height. Lift coefficients and drag coefficients are obtained from plots of lift coefficient vs. an angle of attack and plots of drag coefficient vs. lift coefficient. The procedure and plots are presented in [17,18,32].

The tangential speed of the blade (u_{tb}) is liner speed of the rotating blade with a constant angular velocity (Ω) and varies along the local rotor radius. The ratio of tangential velocity of the blade to wind speed is known as the speed ratio (λ) of the blade at the local rotor radius of r and is presented in Equation (2.6a).

$$\lambda = \frac{u_{tb}}{u_w} = \frac{r\Omega}{u_w} \tag{2.6a}$$

When the local rotor radius (r) corresponds to the blade tip radius (R), Equation (2.6a) is named the tip speed ratio (TSR) [8].

$$\text{TSR} = \frac{R\Omega}{u_w} \tag{2.6b}$$

Hau [25] reported a TSR of 10 for a two-bladed wind turbine and a TSR of 7-8 for three-bladed wind turbines. Herein, the TSR is assumed to be a constant value, and the speed ratio linearly increases along the local rotor radius. For a given wind speed and TSR value, angular velocity of the blade can be determined from Equation (2.6b). The tangential velocity of the blade along the local blade radius can be given by Equation (2.6a).

When pitch angle and pre-twist angles of the blade is ignored, lift and drag forces are decomposed with respect to the Y- and Z-axis. The resultant of each decomposed component along the Y- and Z-axis are, respectively:

$$dP_Z = \frac{\delta L}{c\delta r}\cos\alpha + \frac{\delta D}{c\delta r}\sin\alpha \tag{2.7}$$

and

$$dP_Y = -\frac{\delta L}{c\delta r}\sin\alpha + \frac{\delta D}{c\delta r}\cos\alpha \tag{2.8}$$

2.3.2 Flexural Rigidity

Simple cantilever beam representation of the blade is used to estimate its flexural rigidity (*EI*) as shown in Equation (2.9) in conjunction with computational simulations. The primary assumptions in bending theory of a cantilever are that the traverse plane sections remain plane and normal to the longitudinal axis before and after bending [51]. Radius of curvature (R_c) is defined as a function of the blade length and out-of-plane displacement as shown in Equation (2.10). Substituting Equation (2.10) into Equation (2.9) and using $\theta_w = dw/dX$ obtains the beam flexural rigidity as presented in Equation (2.11).

$$\frac{1}{R_c} = \frac{M_b}{EI} \tag{2.9}$$

where E is the Young's modulus, I the 2nd moment of inertia, and M_b the bending moment.

$$\frac{1}{R_c} = \frac{\dfrac{d^2 w}{d X^2}}{\left[1+\left(\dfrac{d w}{d X}\right)^2\right]^{3/2}} \tag{2.10}$$

where w is the out-of-plane displacement, and X the axial distance.

$$EI = \frac{M_b(X)}{d\theta_w / dX}\left[1+\theta_w^{\,2}\right]^{3/2} \tag{2.11}$$

2.4 Vibration Analyses

The natural frequencies and corresponding mode shapes are obtained for undamped and non-rotational blades. Linear perturbation scheme and Lanczos method (Appendix D) are utilized to extend the eigenvalues.

It is very difficult to study the dynamic response of the blade since its aerodynamic environment is so complex and unsteady. It is useful to analyze the dynamic behavior of the blade by representing it as a uniform hinged-beam. The hinge spring stiffness of the blade is estimated by treating the blade as an equivalent uniform-hinged beam [8]. The relationship between the hinge spring stiffness (K_s) and mass moment of inertia (I_b) is simply expressed in Equation (2.12).

$$K_s = I_b \omega_{NR}^2 \tag{2.12}$$

where ω_{NR} is the non-rotating natural frequency.

3. BLADE CASE STUDIES

This section describes details of two blade models developed to understand static and dynamic behaviors of the blade. First, a pre-twisted and tapered 5.53 m blade without any internal reinforcements is considered to focus on adequately describing its skin. Next, an 80 m blade with traditional spar cap and shear web configuration, designed to satisfy the future energy demand, is described in Section 3.2. In the subsequent efforts, partial blade models are developed to assess changes introduced by replacing shear webs with tubulars. All models are analyzed in ABAQUS with S3R and S4R shell elements.

3.1 Case I: P20KW-L5.5M Blade

As a preliminary study, the geometric configuration of the 19.8 kW (P20KW) wind turbine blade developed by the National Renewable Energy Laboratory (NREL) is analyzed [32]. The blade tip radius is 5.53 m (L5.5M). The blade is mounted on a hub on a 12.2 m tall column. Blade dimensions and airfoil shape are given in Figure 3.1. Airfoil geometry corresponding to the span station is created in SolidWorks as described below.

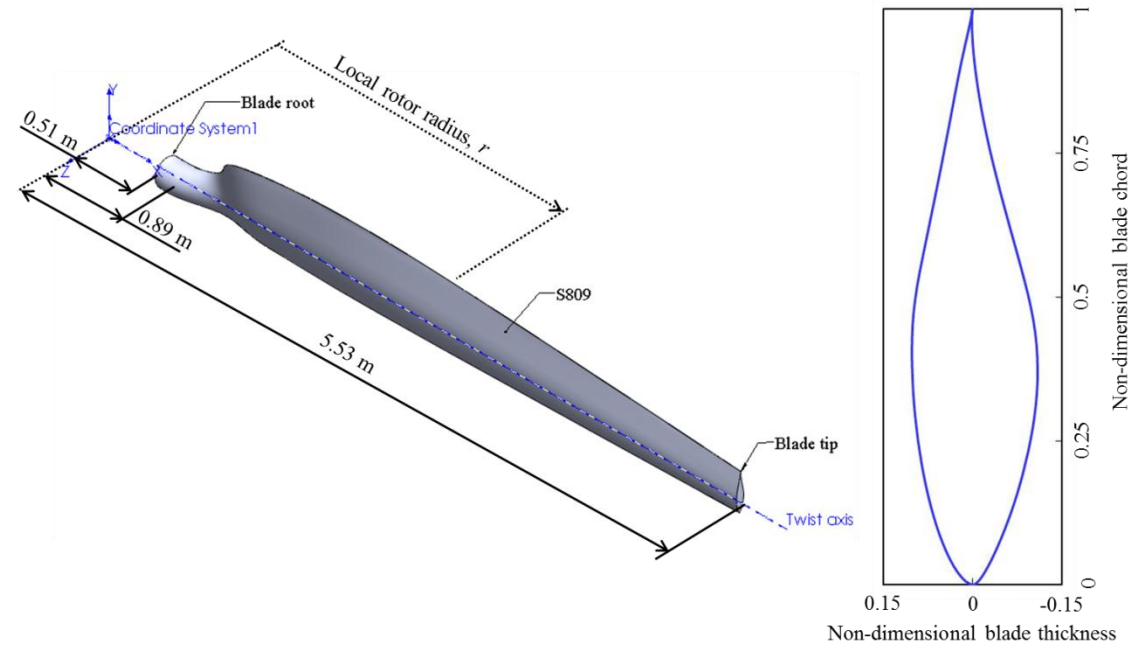

(a) (b)

Figure 3.1. (a) 19.8 kW wind turbine blade, and (b) S809 airfoil shape.

As suggested by Giguere and Selig [32], the S809 airfoil is considered where a blade thickness is assigned as 21% of the chord length. The blade is attached at a local rotor radius (r) of 0.51 m. Its root with the cylindrical section extends to r = 0.89 m, and the S809 airfoil transition begins at r = 0.89 m as noted in Figure 3.1. Normalized chord length (c/R) for the blade model is presented in Figure 3.2(a). The ratio of the blade thickness (t) to chord length (c) is presented in Figure 3.2(b). Note that the geometrical root section for $0.51 < r < 0.89$ is $t/c = 1$, and the non-dimensional blade thickness (t/c) is rapidly decreased between r = 0.89 m and r = 1.26 m due to a transition from the circular attachment to the S809 airfoil shape. The blade is twisted along the local rotor

radius as shown in Figure 3.2(c). This twist convention is positive in a counterclockwise direction, and the twist axis is located at 30% of the chord length in the airfoil section.

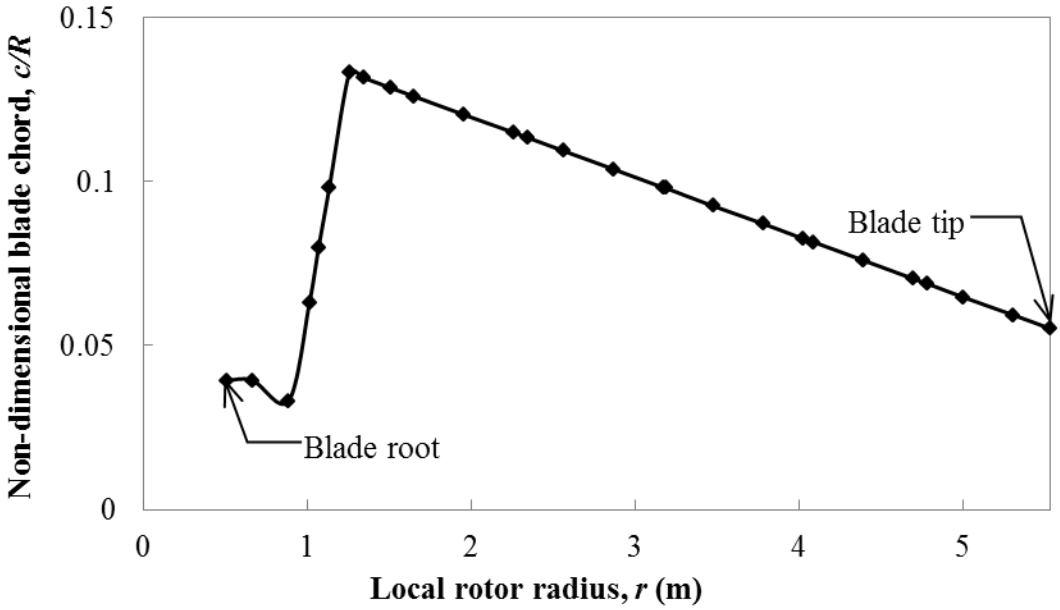

(a)

Figure 3.2. Geometrical details of the 5.53 m blade: (a) non-dimensional chord distribution, (b) non-dimensional thickness distribution, and (c) pre-twist angle distribution [32].

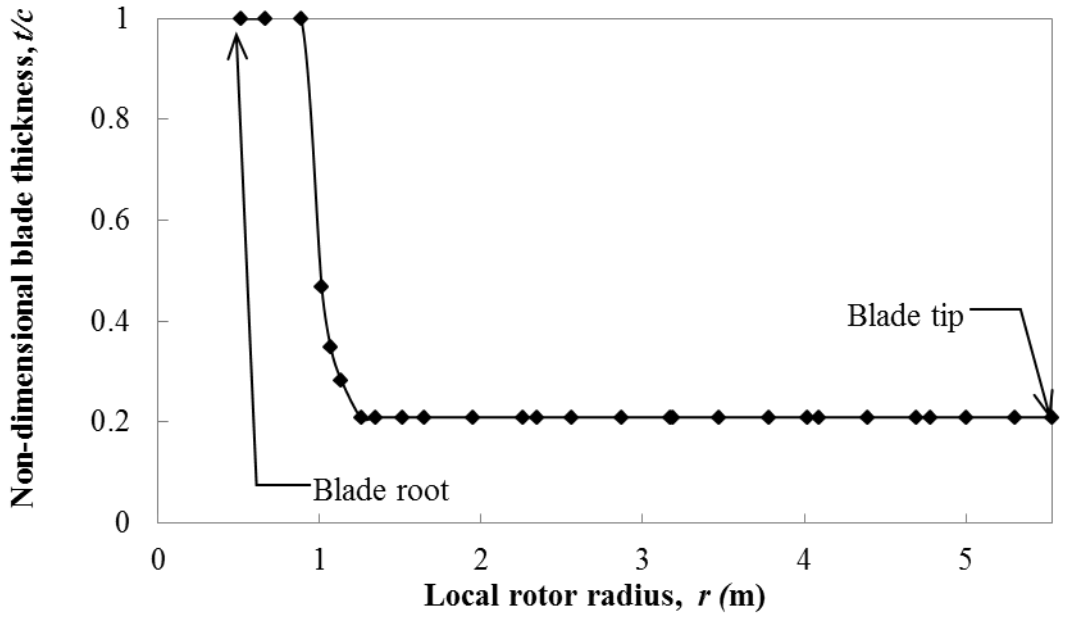

(b)

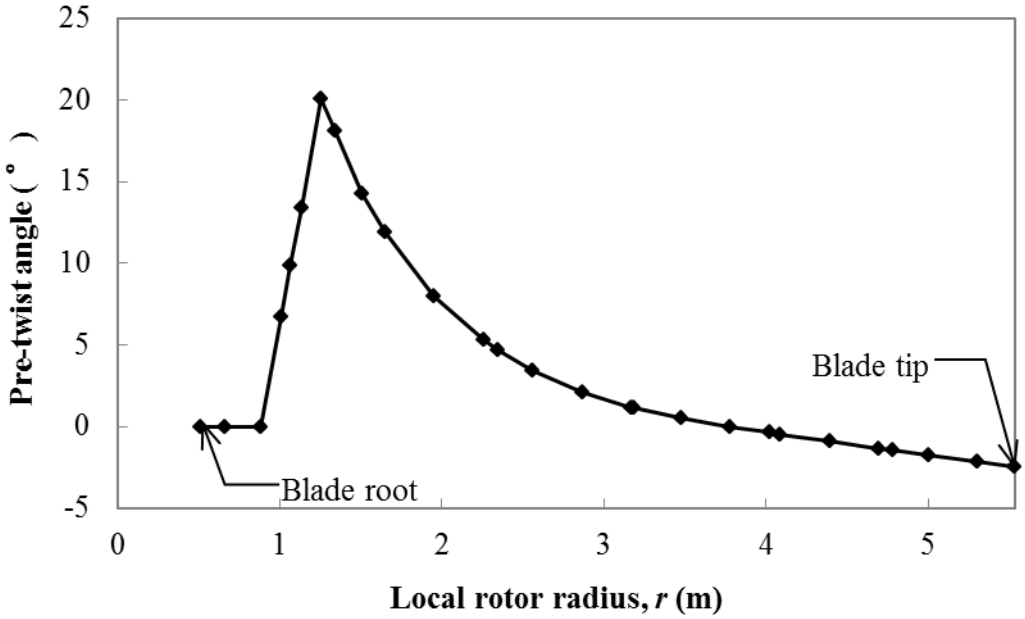

(c)

Figure 3.2. Continued.

The laminate for the blade skin construction, taken from a Technical University of Denmark (DTU) report, has thirteen layers of unidirectional (UD) E-glass/epoxy prepreg (1.24 mm thick) and six fabric E-glass layers (0.48 mm thick), for a total laminate thickness of 19 mm [40]. The stacking sequence is $[\pm 45/0_3/\pm 45/0_2/\pm 45/0_{1.5}]_s$. Material properties used in these computational analyses are given in Table 3.1. The weight of the blade model is 209 kg.

Table 3.1. Blade skin material properties [46].

	UD E-glass/epoxy	**±45° fabric/epoxy**
ρ_m (kg/m^3)	2,100	2,100
E_1 (GPa)	39	10.76
E_2 (GPa)	8.6	10.76
E_3 (GPa)	8.6	8.6
G_{12} (GPa)	3.8	7.52
G_{13} (GPa)	3.8	7.52
G_{23} (GPa)	3.07	3.07
v_{12}	0.28	0.416
v_{13}	0.28	0.416
v_{23}	0.4	0.4

For simplicity, only lift forces are conducted when pre-twist angles and an angle of attack for the blade are discounted. The resultant relative wind velocity is equivalent to the nominal wind speed of 14 m/sec. Air density is taken as 1.22 kg/m^3. The lift coefficient of the S809 is 1.06 [32]. The surface lift force is calculated to be 127 Pa.

3.2 Case II: P8MW-L80M Blade

This blade, selected for an 8 MW (P80MW) class wind turbine, has a blade tip radius of 80 m (L80M) and is positioned at a 140 m hub-height. The blade geometry in Figure 3.3(a) is modeled in SolidWorks. In the blade model, the pre-twist angle distribution is neglected for simplicity. The thick-airfoil family (NREL S817, S816, S818) is employed for its excellent aerodynamic performance as reported [16,18]. The corresponding cross-sections are shown in Figure 3.3(b). The non-dimensional blade incorporated with this airfoil family has already been designed to predict computationally its aerodynamic characteristics [16,18].

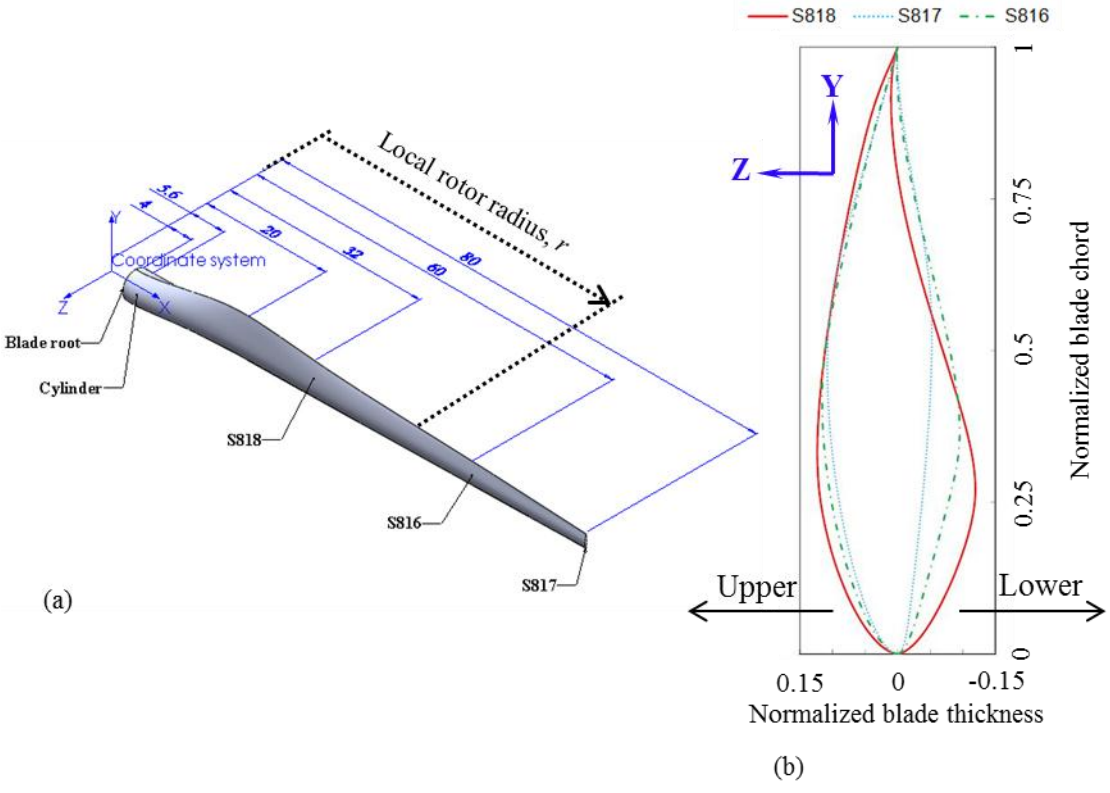

Figure 3.3. 80 m blade: (a) dimensions of the blade, and (b) airfoil shapes.

3.2.1 Blade Geometry Specifics

The span station determined as a function of *r/R* describes the non-dimensional local rotor radius, i.e., *r/R* = 0 indicates the hub center, and *r/R* = 1 denotes the blade tip. The non-dimensional chord (*c/R*) distribution along the span station is taken from Griffin [11,30,31]. Note that Griffin's blades are designed for wind turbines with blade tip radii of 40-60 m, and he modifies blade thicknesses based on computational aerodynamics in order to obtain high power performance of wind turbines [11,30,31]. The blade cross-section shape and ratio of the blade thickness to the chord length (*t/c*) along the span station are provided in Somers *et al.* [16,18]. These non-dimensional specifications of Griffin [11,30,31] and Somers *et al.* [16,18] are summarized in Table 3.2, and the 80 m blade model for this research is extrapolated based on the specifications.

Table 3.2. Extracted geometrical specifications [11,16,18,30,31].

Span station, *r/R*	**Cross-section**	**Chord length, *c/R***	**Blade thickness, *t/c***
0.05	Cylinder	0.055	1
0.07	Cylinder	0.055	1
0.25	S818	0.08	0.24
0.4	S818	0.0692	0.24
0.75	S816	0.044	0.21
1	S817	0.026	0.16

In the 80 m blade model, the first internal reinforcement construction is composed of spar caps and shear webs (SW model) as presented in Figure 3.4. To improve buckling stability in the blade, the recommended positions for the forward and

aft shear webs are, respectively, 15% and 45% of the chord length measured from Point A to Point B in Figure 3.4 [11,30,31]. Spar caps are located between the forward and aft shear webs. Dorsally the spar cap width is a constant from the blade root to 25% of the blade tip radius, and this width is linearly decreased further to the blade tip [11,30,31].

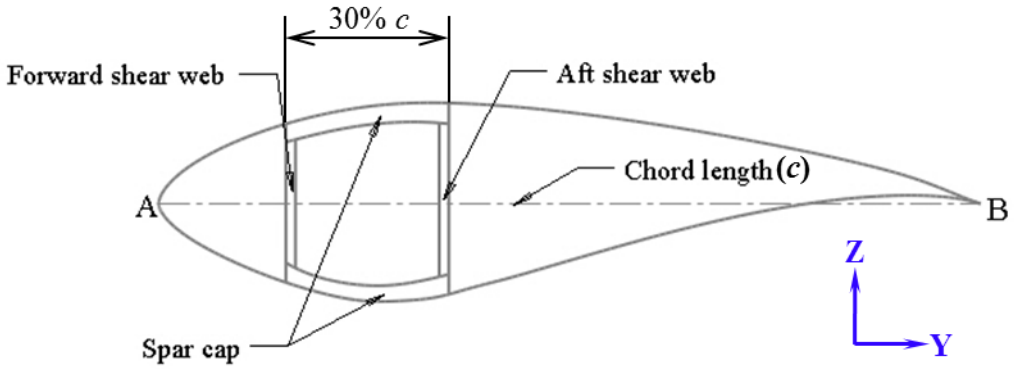

Figure 3.4. Spar cap/shear web configuration.

3.2.2 Material Properties

The materials used in the blade model are unidirectional glass fiber (UD-GF), GF fabric, carbon fiber fabric, and balsa wood. Material properties and allowable strength are presented in Tables 3.3 and 3.4, respectively [13,24,46,47]. Note that in Table 3.3, the properties of fabric layers are homogenized. While von Mises stress is utilized for isotropic materials to investigate damage mechanisms, Hashin damage indicators are utilized for the composite materials.

Table 3.3. Material elastic properties [13,24].

	UD-GF	**Fabric GF**	**Fabric CF**	**Balsa**
ρ_m (kg/m^3)	2,100	2,100	1,600	155
E_1 (GPa)	46	21	47	4.1
E_2 (GPa)	13	21	47	4.1
E_3 (GPa)	13	8.55	10	4.1
G_{12} (GPa)	5	3.7	3.78	0.166
G_{13} (GPa)	5	3.5	3.5	0.166
G_{23} (GPa)	4.6	3.5	3.5	0.166
v_{12}	0.3	0.183	0.33	0.3
v_{13}	0.3	0.0305	0.33	0.3
v_{23}	0.42	0.075	0.07	0.3

Table 3.4. Allowable material strength in MPa [24,46,47].

	UD-GF	**Fabric GF**	**Fabric CF**	**Balsa**
X_T	1,080	367	627	7
X_C	620	549	572	5.4
Y_T	39	367	627	7
Y_C	128	549	572	5.4
S_L	89	97.1	80	1.6
S_T	64	274.5	286	2.7

3.2.3 Loads

Air density (ρ) is assigned as 1.208 kg/m^3 for 140 m hub-height. The TSR of the blade is assumed to be constant at 7 [25]. Wind speed of 20 m/sec, which represents the lower limit of the cut-out wind speed, is considered. Resultant relative wind speed (V_{rel}) along the local rotor radius can be found to calculate lift and drag forces as shown in Table 3.5.

The remaining parameters used in Equations (2.5) to (2.8) are determined as follows: The graph of lift and drag coefficient is utilized to obtain the limit angle of attack (α_l). This graph describes the low-drag lift coefficient range for given C_l and C_d values. The upper limit of C_l of this range is selected, and its corresponding angle of attack is taken [18]. Since tangential velocity of the blade is not constant along the local rotor radius, lift and drag forces are obtained at locations (Nodes) creating eight sections as presented in Table 3.5. Afterwards, lift and drag forces are decomposed into the Y- and Z-axis components (dP_Y and dP_z) as presented in Table 3.5. Note that values of dP_Y in Table 3.5 are one-half of dP_Y values calculated in Equation (2.8) since the Y component of the resultant force (dP_Y) is applied to two surfaces of the blade. In each section, the corresponding nodal forces are averaged to obtain the resultant forces which are presented in Figure 3.5. The distribution of the resultant force components are presented in Figure 3.5.

Table 3.5. Load at nine nodes along the rotor radius.

Node No.	r **(m)**	V_{rel} **(m/sec)**	α_l **(°)**	C_l	C_d	dP_y **(Pa)**	dP_z **(Pa)**
1	4	21.2	6.5	0	0.3	41	9
2	5.6	22.3	6.5	0	0.3	45	10
3	20	40.3	6.5	1.2	0.012	-61	1,170
4	32	59.5	6.5	1.2	0.012	-133	2,550
5	46	82.9	7	1	0.008	-237	4,130
6	60	107	7	1	0.008	-393	6,860
7	70	124	5	0.9	0.007	-333	8,350
8	75	133	5	0.9	0.007	-381	9,550
9	80	141	5	0.9	0.007	-432	10,800

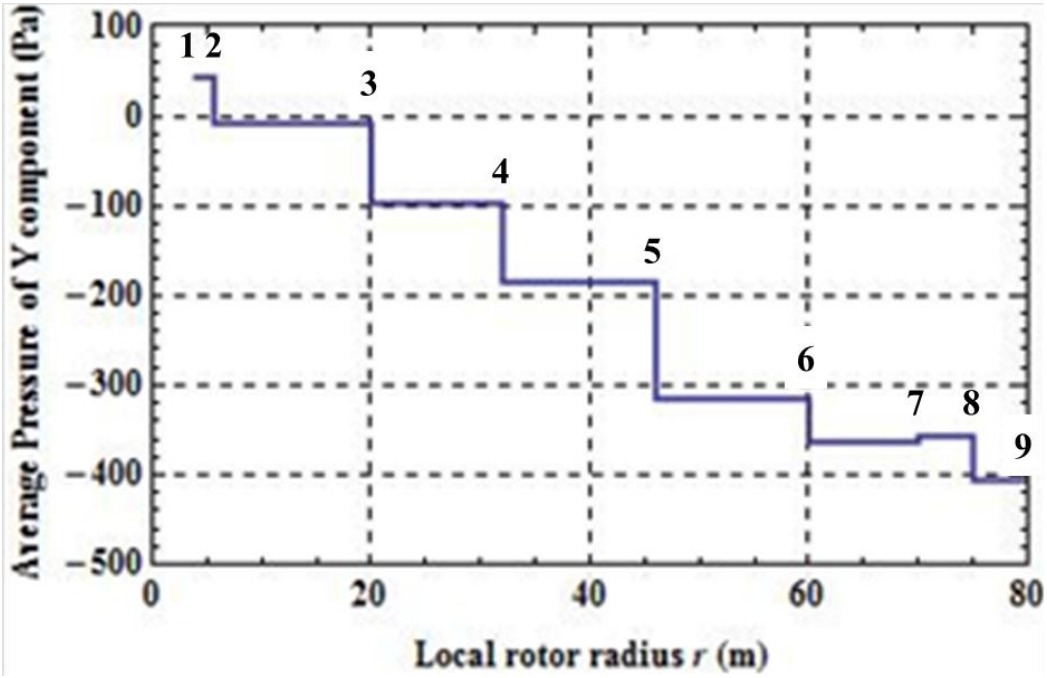

(a)

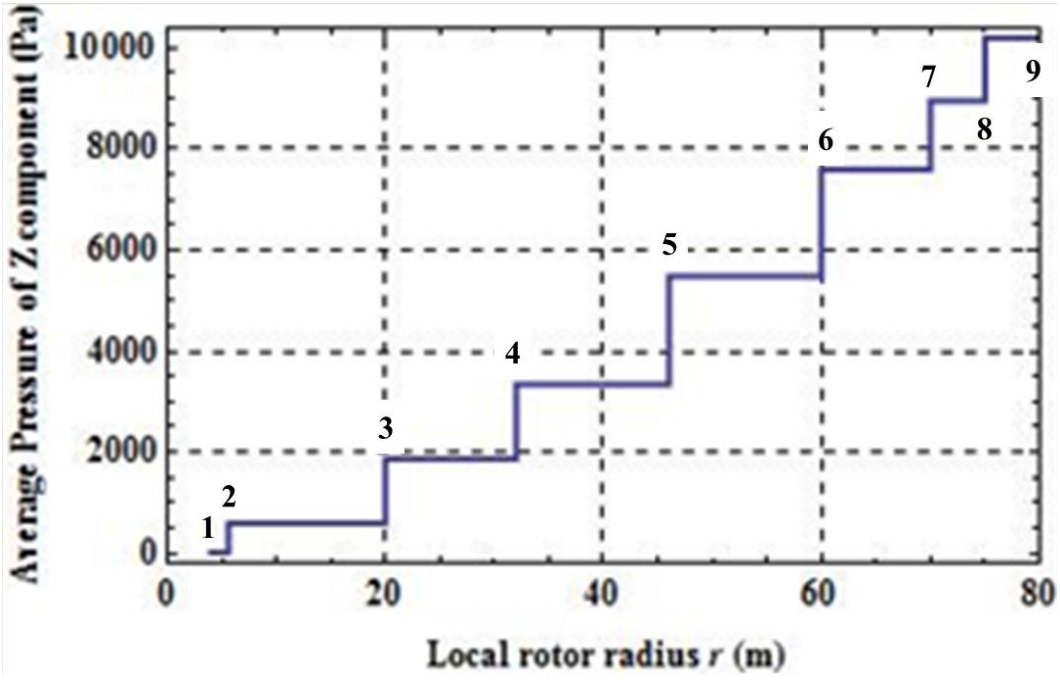

(b)

Figure 3.5. Surface force distributions: (a) Y component (dP_y), and (b) Z component (dP_z).

3.2.4 Composite Layup

Herein, we describe the laminate stacking sequence and corresponding layer thicknesses in each model. The five models described here offer potential weight saving considering either by replacing sandwich construction with monolithic laminate and/or changing laminate thickness and hybridization of reinforcement types.

3.2.4.1 SW-91 Model

The root section of the blade consists of GF fabric layers. In the airfoil section, the blade skin and shear web are treated as sandwich constructions of GF layers with balsa wood as core. The thickness ratio of the face laminate to the core is 10 [24]. GF fabric layers are employed for the face laminate in the skin, and the face in the webs is laminated with 0°, 45°, and -45° UD-GF layers. Hybrid glass/carbon composite laminates which contain 15% CF fabric and 85% UD-GF layer reinforcement by thickness are used for the spar caps. Properties of both the blade skin and spar cap laminates are assigned to the blade skin between the forward and aft shear web as shown in Figure 3.6, and these properties creates the asymmetric section stiffness matrix.

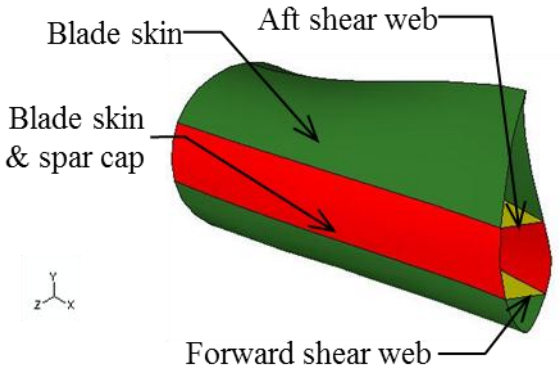

Figure 3.6. Locations of laminates in the partial blade (5.6 m < r < 20 m).

The composite lay-up employed in this model is summarized in Tables 3.6 and 3.7. Note that the blade skin laminate between the forward and aft shear web also reflects the spar cap layers in the simulation. Again, material properties and their allowable strength are presented in Tables 3.3 and 3.4, respectively.

Table 3.6. Lay-up for blade root and skin.

Ply	**Blade root**		**Blade skin**	
	Material	**Thickness (%)**	**Material**	**Thickness (%)**
1	GF fabric	25	GF fabric	4.5
2	GF fabric	25	Balsa	91
3	GF fabric	25	GF fabric	4.5
4	GF fabric	25	-	-

Table 3.7. Lay-up for spar cap and shear web.

Ply	Spar cap		Shear web	
	Material	**Thickness (%)**	**Material**	**Thickness (%)**
1	CF fabric	2.5	GF fabric	2.25
2	UD-GF	19.2	45º UD-GF	1.125
3	CF fabric	2.5	-45º UD-GF	1.125
4	UD-GF	13.3	Balsa	91
5	CF fabric	2.5	-45º UD-GF	1.125
6	UD-GF	10	45 º UD-GF	1.125
7	UD-GF	10	GF fabric	2.25
8	CF fabric	2.5	-	-
9	UD-GF	13.3	-	-
10	CF fabric	2.5	-	-
11	UD-GF	19.2	-	-
12	CF fabric	2.5	-	-

Since the composite blade root is connected to the hub with large bolts, this section usually experiences high stresses. Therefore, laminates at the blade root section are much thicker than at the rest of the blade. The blade is divided into eight regions to incorporate a gradual taper in laminate thickness as presented in Table 3.8.

The resulting total weight and inertia values of SW-91 Model are presented in Table 3.9. The weight of shear webs in this model is 10.8 tons.

Table 3.8. Thickness distribution in SW-91 Model.

Range of local rotor radius, *r* (m)	**Blade root (m)**	**Blade skin (m)**	**Spar cap (m)**	**Shear web (m)**
4-5.6	0.4	-	-	0.2
5.6-20	-	0.2	0.06	0.2
20-32	-	0.2	0.06	0.2
32-46	-	0.15	0.06	0.15
46-60	-	0.15	0.06	0.15
60-70	-	0.1	0.03	0.1
70-75	-	0.05	0.015	0.05
75-80	-	0.05	0.015	0.05

Table 3.9. Inertia properties of SW-91 Model.

	SW-91 Model
Blade weight (tons)	90.9
Moment of inertia for torsion, I_{xx} (kgm^2)	2.96×10^5
Moment of inertia for edge, I_{yy} (kgm^2)	9.13×10^7
Moment of inertia for flapping, I_{zz} (kgm^2)	9.14×10^7

3.2.4.2 SW-86 Model

In this model, the balsa core is removed from the blade skin in the spar cap section of SW-91 Model as shown in Figure 3.7. Every detail of geometry, materials and loads are kept the same. The total weight and moment of inertia about the X-, Y-, and Z-axis of SW-86 Model are presented in Table 3.10.

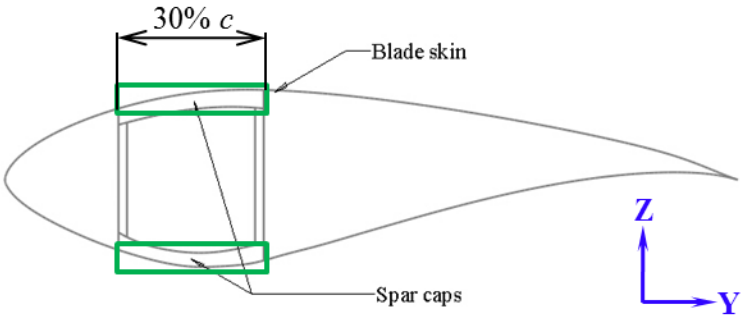

Figure 3.7. Locations for the core removal in the skin of SW-86 Model.

Table 3.10. Inertia properties of SW-86 Model.

	SW-86 Model
Blade weight (tons)	86.2
Moment of inertia for torsion, I_{xx} (kgm^2)	2.90×10^5
Moment of inertia for edge, I_{yy} (kgm^2)	8.51×10^7
Moment of inertia for flapping, I_{zz} (kgm^2)	8.52×10^7

3.2.4.3 SW-77 Model

For all sandwich laminates of SW-91 Model, the thickness ratio of the face to the core is reduced from 10 to 3.3 (Table 3.11). However, their face thicknesses are kept the same as SW-91 Model. As the core thickness is reduced, thicknesses of sandwich constructions are also decreased as shown in Table 3.12. The rest of all geometry, material, and load details are maintained to SW-91 Model. The blade weight and inertia values of SW-77 Model are presented in Table 3.13. The weight of shear web in this model is 7.6 tons.

Table 3.11. Skin and shear web laminates in SW-77 Model.

Ply	Blade skin		Shear web	
	Material	**Thickness (%)**	**Material**	**Thickness (%)**
1	GF fabric	11.6	GF fabric	5.8
2	Balsa	76.8	45º UD-GF	2.9
3	GF fabric	11.6	-45º UD-GF	2.9
4	-	-	Balsa	76.8
5	-	-	-45º UD-GF	2.9
6	-	-	45 º UD-GF	2.9
7	-	-	GF fabric	5.8

Table 3.12. Thickness distribution in SW-77 Model.

Range of local rotor radius, *r* (m)	**Blade skin (m)**	**Shear web (m)**
4-5.6	-	0.08
5.6-20	0.08	0.08
20-32	0.08	0.08
32-46	0.06	0.06
46-60	0.06	0.06
60-70	0.04	0.04
70-75	0.02	0.02
75-80	0.02	0.02

Table 3.13. Inertia properties of SW-77 Model.

	SW-77 Model
Blade weight (ton)	76.9
Moment of inertia for torsion, I_{xx} (kgm^2)	2.45×10^5
Moment of inertia for edge, I_{yy} (kgm^2)	7.45×10^7
Moment of inertia for flapping, I_{zz} (kgm^2)	7.46×10^7

3.2.4.4 SW-63 Model

Laminate thicknesses of SW-63 Model are determined based on Griffin's blade model [11,30,31]. Thicknesses for each face of sandwich constructions in the skin and shear web are taken as a constant of 2 mm. Thickness of the balsa core is as follows: In the forward skin (blue dash line box in Figure 3.8), 0.5% of chord length at the local airfoil is used for the core thickness. In the middle skin adhering to the spar cap (light blue solid line box in Figure 3.8), there are no balsa cores. In the aft skin (red dash line box in Figure 3.8), 1% of the chord length at the local airfoil is used. In the laminate of shear webs, balsa core thickness is 1% of the airfoil chord length. The thickness of the spar cap corresponds to 5% of the local maximum cross-section thickness. In this model, shear webs are constructed in its airfoil section only. Thus, the shear webs located in blade root section of SW-91 Model are removed. All geometry, materials, and loads used in this model are the same as SW-91 Model (Tables 3.6 and 3.7).

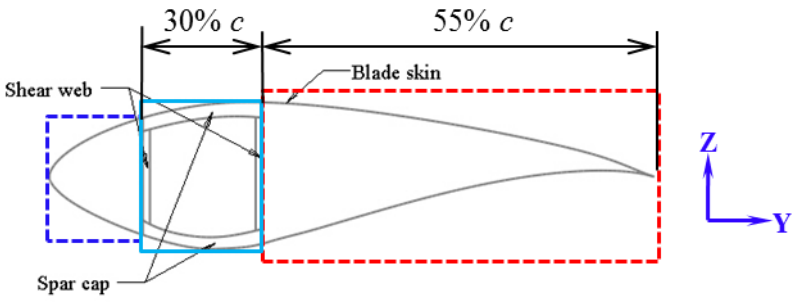

Figure 3.8. Sections of the blade skin in SW-63 Model.

The core thicknesses and laminate thickness of the spar cap are assigned as a step function. The blade is divided into eight sections. Blade thicknesses are first obtained at nine locations which form sections along the local rotor radius. Over each section of the blade, the equivalent section thickness of the core and spar cap is assigned which is obtained by averaging the thicknesses at the two ends of a section. The core thicknesses in the skin and shear web and the laminate thickness of the spar cap are presented in Table 3.14. Inertia properties of SW-63 Model are presented in Table 3.15. The weight of shear web in this model is calculated to be 2.8 tons.

Table 3.14. Thickness distribution of the balsa core and spar cap in SW-63 Model.

Range of local rotor radius, *r* (m)	**Balsa core thickness (m)**			**Spar cap (m)**
	Forward blade skin	**Aft blade skin**	**Shear web**	
4-5.6	-	-	-	-
5.6-20	0.027	0.054	0.054	0.148
20-32	0.030	0.060	0.060	0.072
32-46	0.025	0.050	0.050	0.059
46-60	0.020	0.040	0.040	0.044
60-70	0.016	0.032	0.032	0.032
70-75	0.013	0.026	0.026	0.024
75-80	0.011	0.023	0.023	0.019

Table 3.15. Inertia properties of SW-63 Model.

	SW-63 Model
Blade weight (ton)	63.0
Moment of inertia for torsion, I_{xx} (kgm^2)	1.87×10^5
Moment of inertia for edge, I_{yy} (kgm^2)	5.09×10^7
Moment of inertia for flapping, I_{zz} (kgm^2)	5.09×10^7

3.2.4.5 CT Model

Since SW-91 Model is the heaviest in all SW Models, the shear webs in SW-91 Model are replaced by composite tubular (CT) as described in Appendix E to introduce weight savings. In SW-91 Model, the weight of the shear webs is 10.8 tons, and the tubular construction in the CT Model reduces this weight by a factor of five. Reinforcement tubular geometry is set at 0.1 m in diameter with a wall thickness of 0.01 m. The tubulars are attached to the skins at intervals of approximately 2 m. GF laminate stacking with [0/90/30/-30] is employed for the tubulars as shown in Table E.4. Inertia properties of the CT Model are presented in Table 3.16.

Table 3.16. Inertia properties of the CT Model.

	CT Model
Blade weight (ton)	82.1
Moment of inertia for torsion, I_{xx} (kgm^2)	2.84×10^5
Moment of inertia for edge, I_{yy} (kgm^2)	8.50×10^7
Moment of inertia for flapping, I_{zz} (kgm^2)	8.51×10^7

4. RESULTS AND DISCUSSION

4.1 Case I: P20KW-L5.5M Blade Results

The closed-form solutions based on the blade equivalent cantilever beam are employed to verify computational procedure (Appendix F). As described in Section 3.1, the pressure forces are applied to the lower blade skin along the Z-axis, and the root is fully constrained. The skin laminate consists of nineteen E-glass epoxy layers arranged as $[\pm 45/0_3/\pm 45/0_2/\pm 45/0_{1.5}]_s$, and its total thickness is 19 mm.

4.1.1 Static Analysis Results

4.1.1.1 Displacements

All results provided in Section 4.1.1 are obtained at the loads associated with the resultant relative wind speed of 14 m/sec. The blade is mainly deformed along the Z-axis, where the pressure load is applied. Therefore, the largest displacement component (U3) is presented in Figure 4.1:

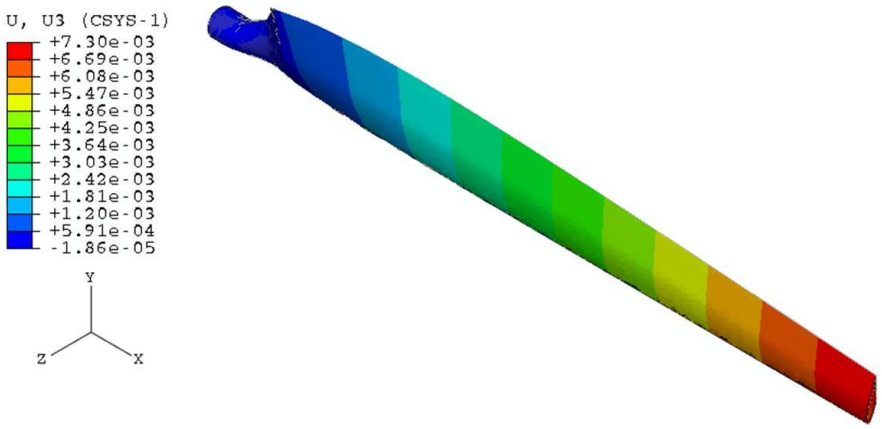

Figure 4.1. U3 (UZ) displacement contour of the 5.53 m blade.

Note that the maximum displacement at the tip is 7.3×10^{-3} m, which is less than 0.2% of the blade length. It decreases linearly along the X-axis, and becomes zero at the blade root. It is plausible to reduce the laminate thickness in order to save weight and still be in the small displacement range.

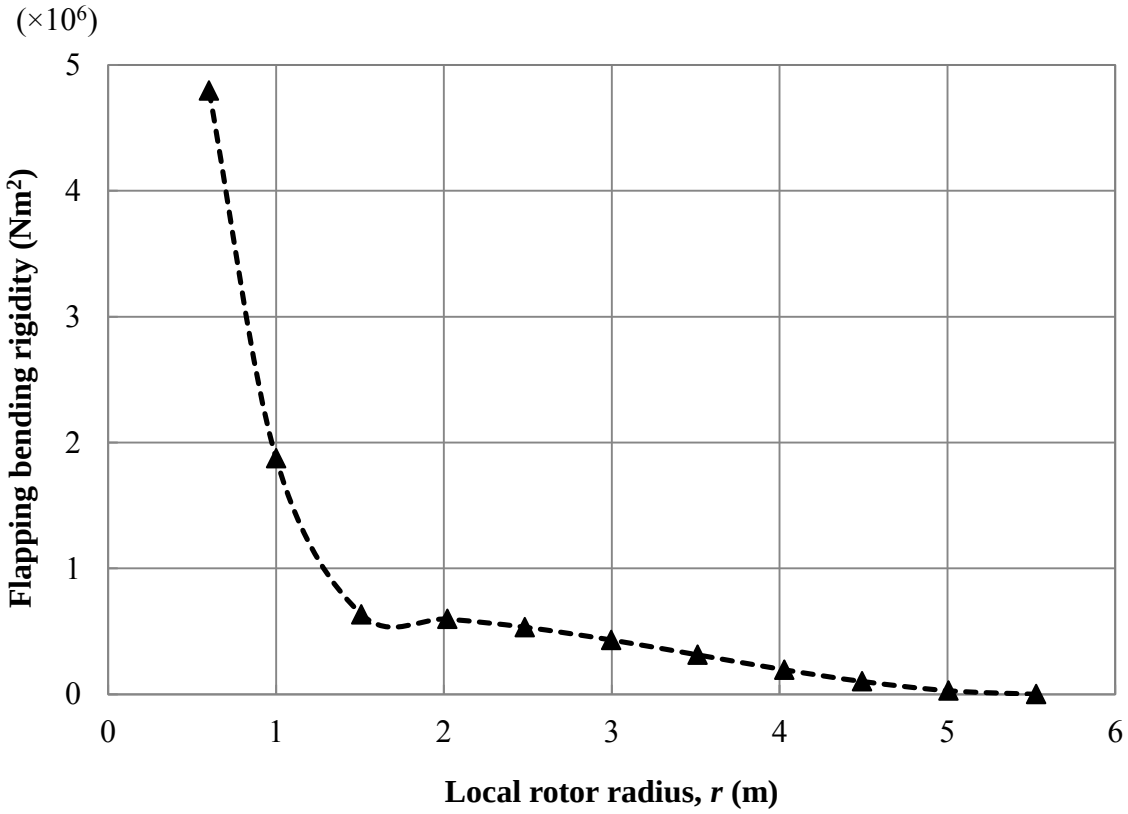

Figure 4.2. Flapping bending rigidity distribution of the 5.53 m blade.

The next parameter of interest is the flapping flexural rigidity along the X-axis. It is evaluated as described in Section 2.3.1. The bending rigidity of the blade is dependent

on the flapping bending moment distribution, which is evaluated as a function of U3 displacement at the nodes of the trailing edge. The bending rigidity, as presented in Figure 4.2, is calculated at intervals of 0.5 m, and extends to the blade tip. The root section and the transition section from the cylinder to airfoil are much stiffer than the airfoil section. The rigidity around the root is approximately 10^4 times the rigidity in the vicinity of the tip.

Further examination of tip displacements is undertaken for the selected nodes presented in Figure 4.3. The corresponding tip displacements about the three global axes are displayed in Figure 4.4.

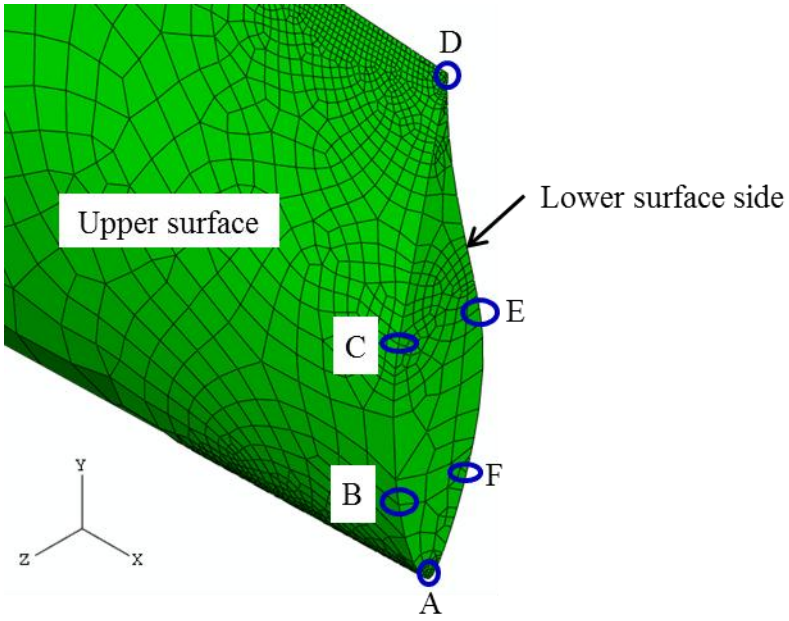

Figure 4.3. Selected nodes at the blade tip for the 5.53 m blade.

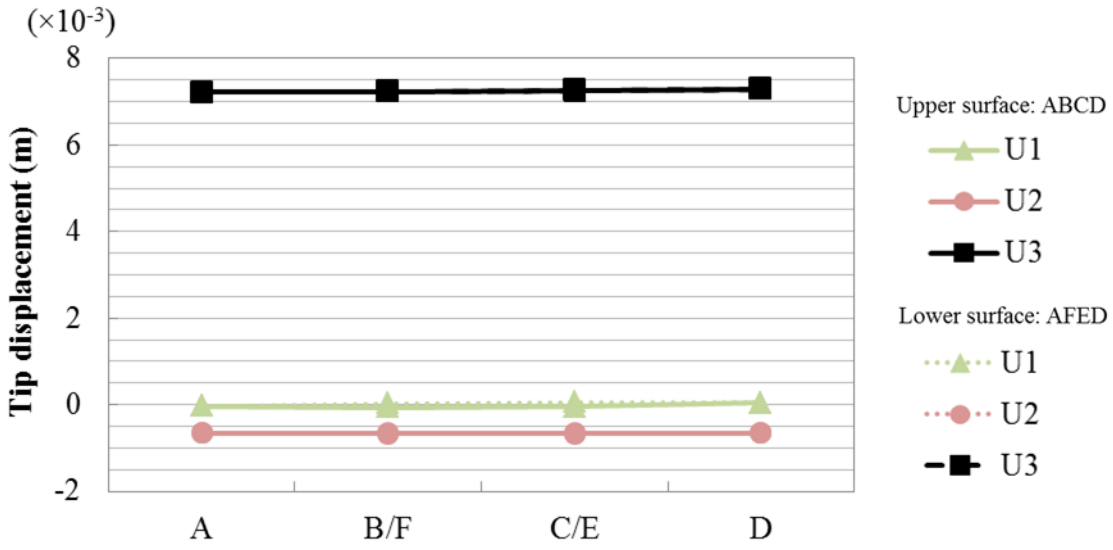

Figure 4.4. Tip displacements of the 5.53 m blade.

Figure 4.4 shows that the deformed cross-section maintains its original shape under loading. The upper surface is under compression, and the lower surface is stretched under tension. The displacements, U1 and U2, arise due to the asymmetric cross-section of the airfoil and the pre-twist in the blade.

4.1.1.2 Stresses

The distance of the outer layer from the centroid of the blade cross-section is greater than that of the inner layer. Also, thickness of the layers is much smaller compared to the distance from the centroid. Thus, the outer layer has higher section modulus than the inner layer. Higher stresses appear in the outermost layer compared to the innermost layer. In stress contours, the S11, S22, and S12 stresses are obtained with

respect to the material coordinate system orientated at 0°, where the vector (3-axis) is normal, and coming out of the surfaces (Figure 4.5).

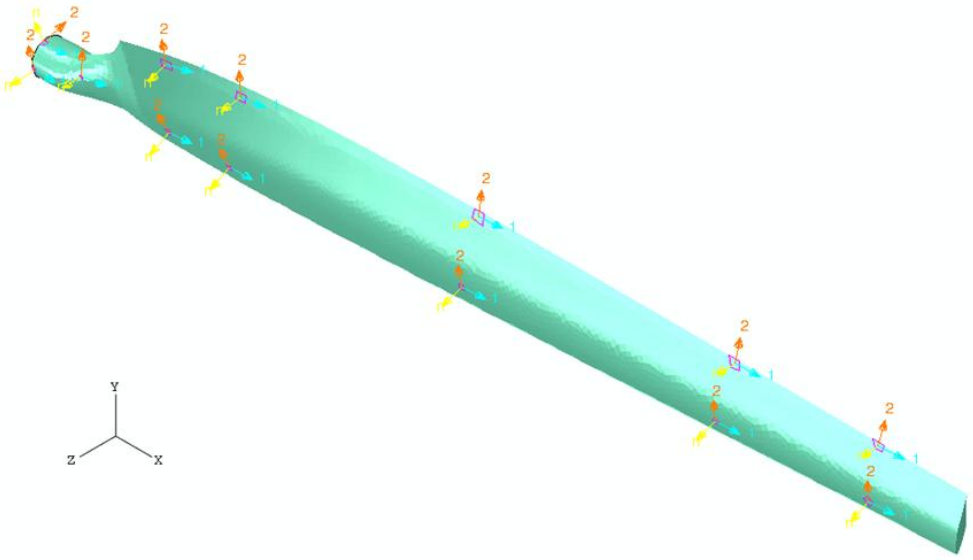

Figure 4.5. Material coordinate system orientated at 0°.

The skin laminate consists of fabric and UD tape layers. The highest stresses in the fabric and 0° layer of the upper surface skin laminate are presented in Figures 4.6 and 4.7, respectively. Note that the skin laminate stack sequence is $[\pm 45/0_3/\pm 45/0_2/\pm 45/0_{1.5}]_s$ and consists of nineteen layers. We designate layers as Layer-1, the innermost layer (±45° fabric layer) to Layer-19, the outermost layer (again ±45° GF fabric layer). Thus, the second layer from the top is Layer-18, (0° GF layer):

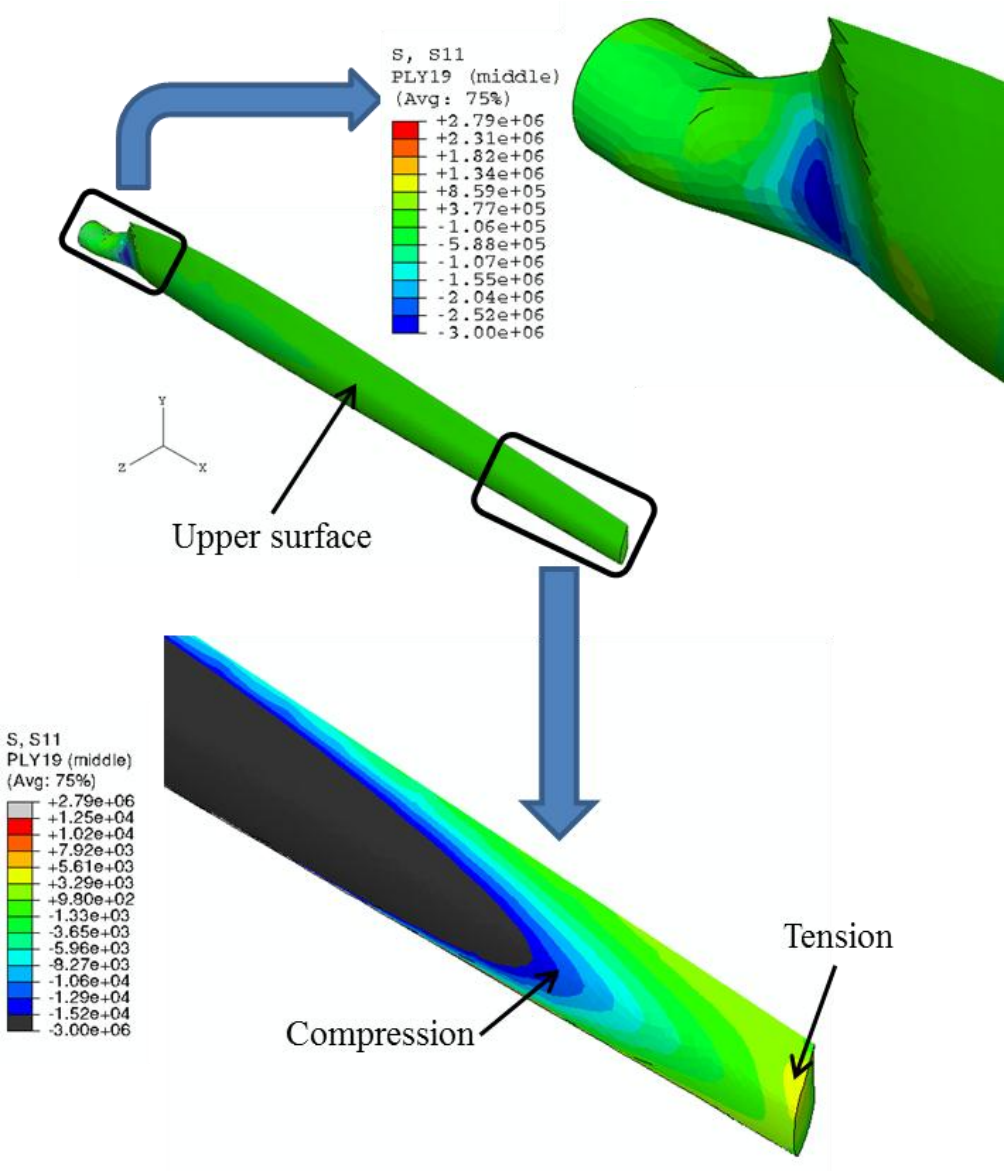

(a)

Figure 4.6. Stress contours of the outermost fabric layer (Layer-19) of the upper surface skin in the 5.53 m blade: (a) S11 contour, (b) S22 contour, and (c) S12 contour.

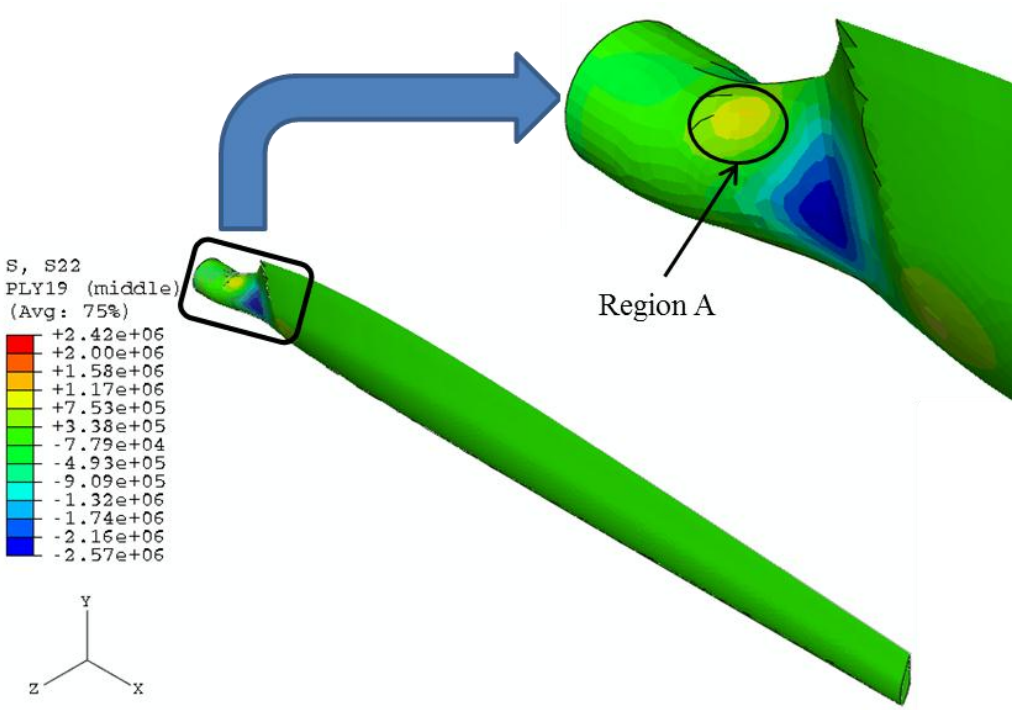

(b)

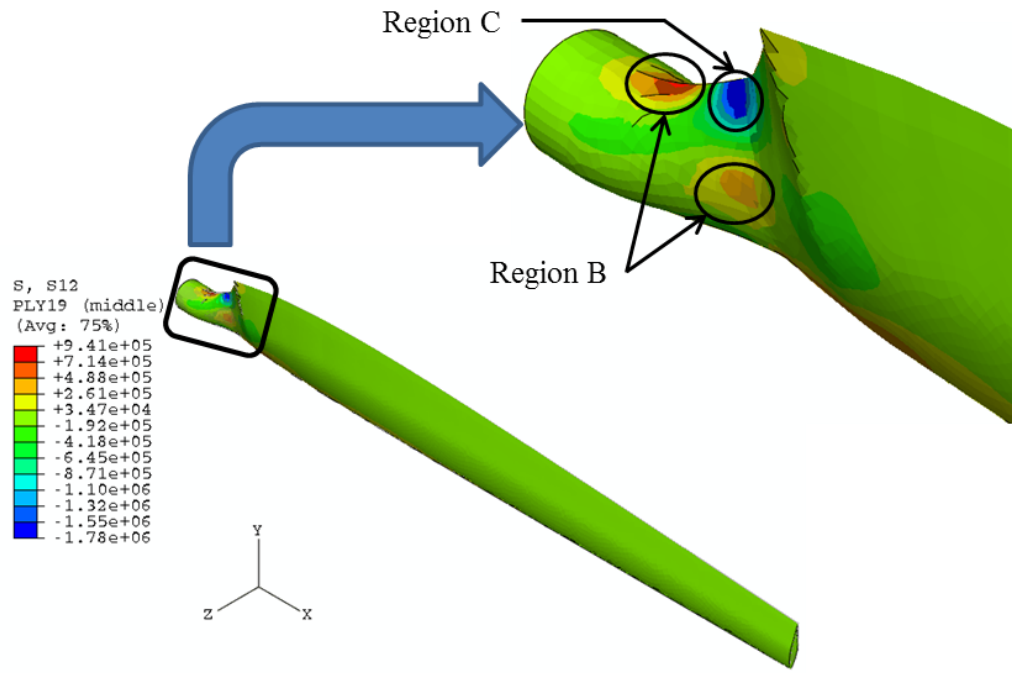

(c)

Figure 4.6. Continued.

The asymmetric airfoil cross-section leads to higher S11 stresses in the upper surface skin than the lower surface skin. The maximum value of the compressive S11 stress in the outermost fabric layer (Layer-19) of the upper skin is about 3 MPa at the transition section where the corresponding reaction moment is higher, but the section modulus is lower. The S11 stresses are much lower in the rest of the airfoil section. At any given cross-section, lower S11 stresses are seen at the leading or trailing edges. The compressive S11 stresses decrease along the local rotor radius toward the tip. However, tensile S11 stresses (about 5.41 kPa) are observed in the vicinity of the tip due to asymmetric blade geometry. The compressive highest S22 stress is 2.57 MPa at the transition. This value is close to the maximum value of the compressive S11 stress since Layer-19 is a plain weave with specially orthotropic behavior, where the Young's moduli in the 1- and 2-axes of the material coordinate system are the same. Tensile stresses develop at the root near the transition at Region A as depicted in Figure 4.6(b). Positive and negative shear stress S12 are observed in the upper skin at Region B and Region C, respectively, as shown in Figure 4.6(c). These stresses develop in response to the taper and the twist in the blade geometry, as well as the change in the cross sectional geometry from a cylinder to an airfoil. The greatest values of the positive and negative S12 stresses are 0.941 MPa and 1.78 MPa, respectively. In this layer, the maximum value of the S11 stresses is approximately two times higher than the S12 stress:

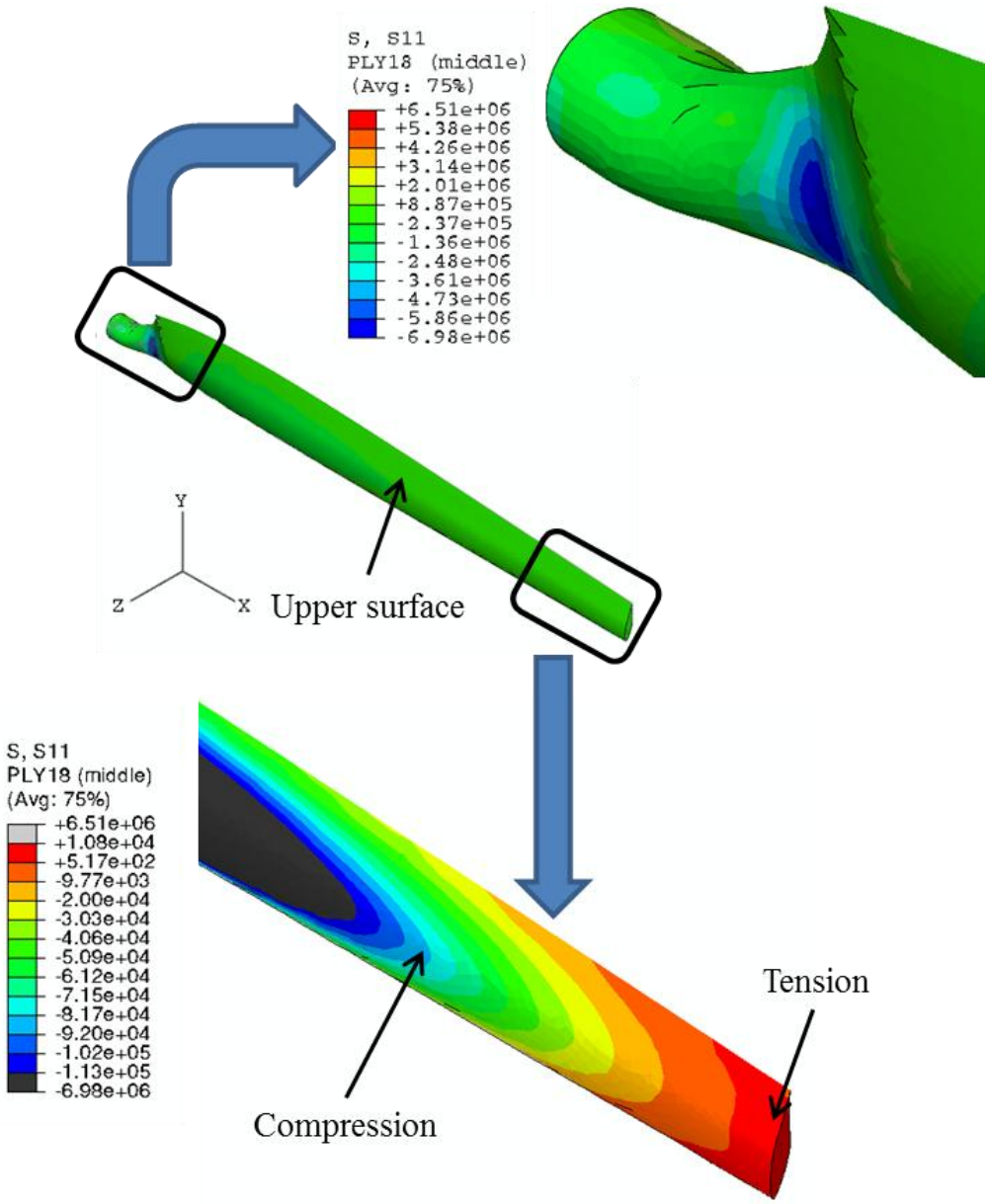

(a)

Figure 4.7. Stress contours of the second layer from the top (Layer 18) of the upper surface skin in the 5.53 m blade: (a) S11 contour, (b) S22 contour, and (c) S12 contour.

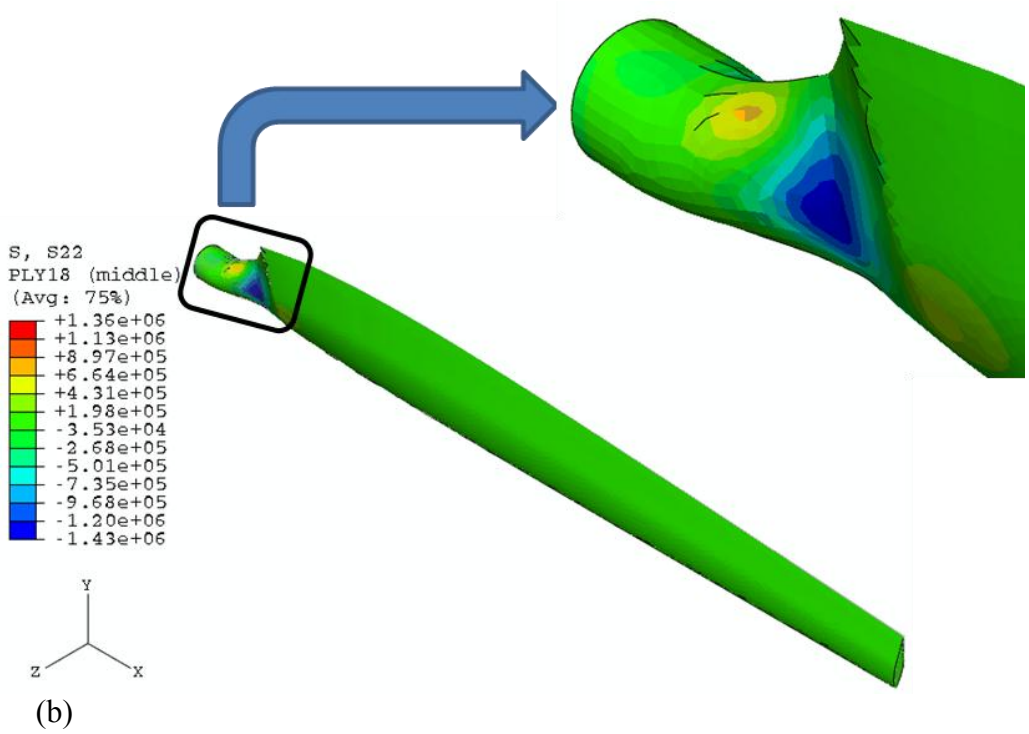

(b)

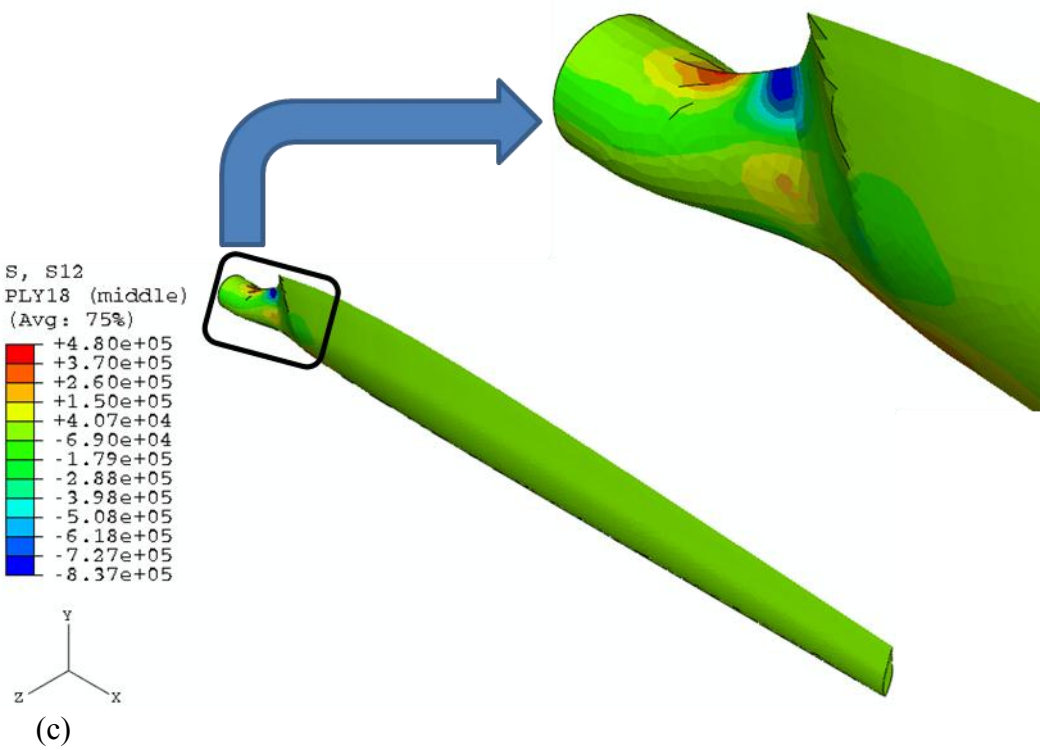

(c)

Figure 4.7. Continued.

Although Figure 4.7 shows stress fields in the 0° layer (Layer-18) of the upper surface skin, they are similar to those of the fabric layer (Layer-19). The maximum magnitude of the S11 stresses in Layer-18 of the upper skin is 6.98 MPa in compression, which is observed at the transition section. This value is approximately two times the maximum value of the S11 stresses in Layer-19 due to the 0° layer's higher in-plane stiffness. The compressive S11 stresses decrease along the local rotor radius approaching the tip. It is observed tensile S11 stresses (about 10.8 kPa) in Layer-18 in the vicinity of the tip, which is two times higher than tensile S11 stresses of Layer-19 (about 5.41 kPa). At the transition section, the highest compressive stress, S22, is 1.43 MPa as presented in Figure 4.7(b). This value is less than the maximum value of the compressive S22 stress of Layer-19, since E_2 of this unidirectional (UD) layer is less than E_2 of Layer-19. The greatest values of the positive and negative S12 stresses are obtained to be 0.480 MPa and 0.837 MPa, respectively, as shown in Figure 4.7(c). As expected, the S11 stress of Layer-18 is the highest in the all stress components.

4.1.2 Natural Frequencies

The first flapping, edge, and torsional natural frequencies of the non-rotating blade are presented in Figure 4.8, and the corresponding mode shapes are shown in Figure 4.9. The mode shapes are normalized so that the largest displacement (or rotation) entry in each vector is unity.

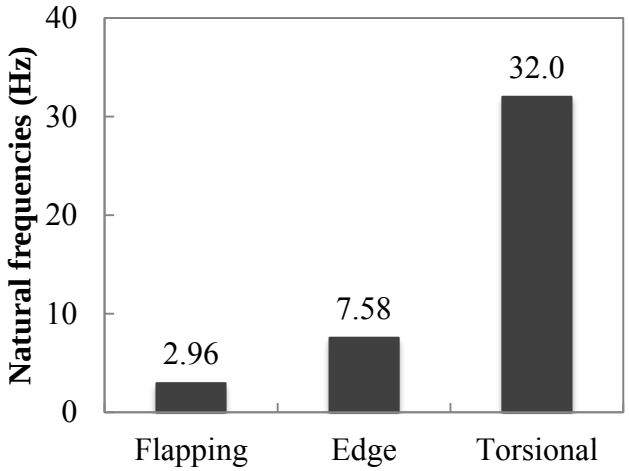

Figure 4.8. Natural frequencies comparison in flapping, edge, and torsional modes.

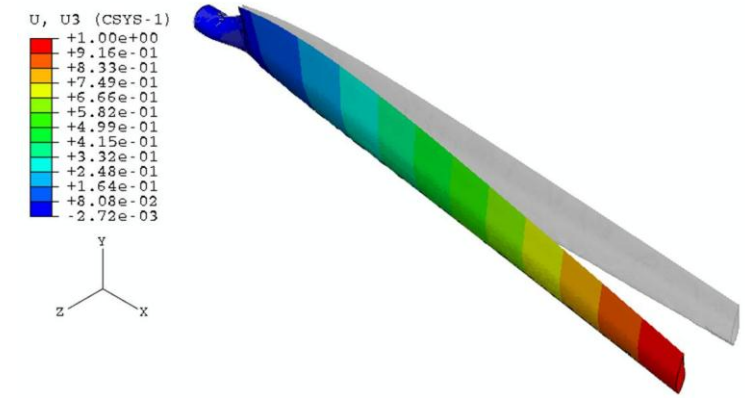

(a)

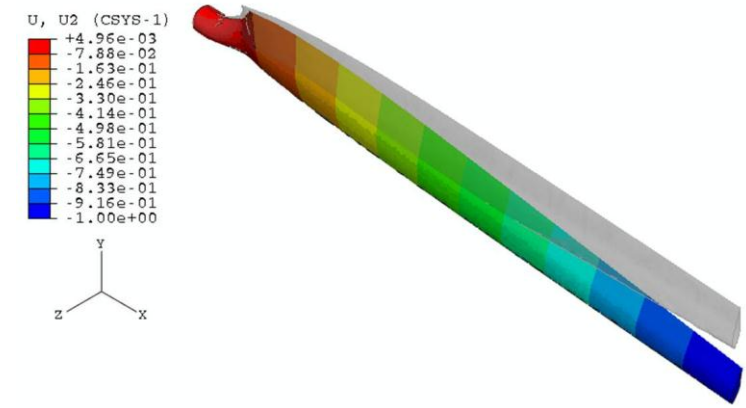

(b)

Figure 4.9. First mode shapes: (a) flapping, (b) edge, and (c) torsional.

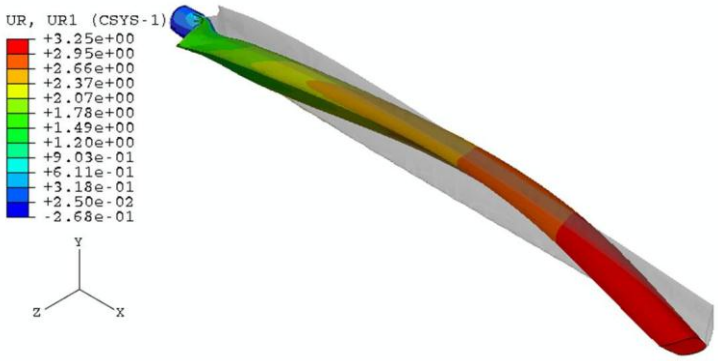

(c)

Figure 4.9. Continued.

The blade thickness and chord length dominate the area moments of inertia for flapping and edge mode, respectively. At the airfoil section, the chord length corresponds to 21% of the blade thickness, as shown in Figure 3.2(b). Thus, in transverse vibration, the flapping mode appears at lower frequency than the edge mode. The high torsional stiffness of this model places the torsional natural frequency above the natural frequencies of the transverse vibration. The lowest natural frequencies of a tower and drive train in the operational wind turbine are reported to be 1.67 Hz and 5.78 Hz, respectively [52]. The extracted lowest natural frequency (2.98 Hz) of the blade is higher than that of the tower and lower than that of the drive train. Since the blade may resonate with the drive train, the lowest natural frequency is desired to be higher than natural frequencies of the drive train. The flapping mode has a U2 displacement whose maximum value is 10% of U3 displacement. In the edge mode, the blade is positively deflected along the Z-axis (U3 displacement) as well, and the maximum magnitude

corresponds to 13% of the U2 displacement. Coupling mode (twisting and bending together) is observed at the higher natural frequencies (Figure 4.10).

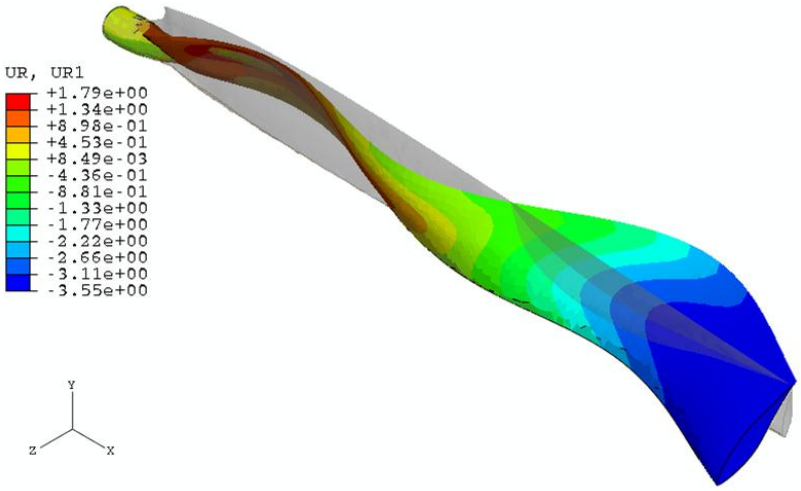

Figure 4.10. Coupling mode shape at 85.7 Hz.

4.2 Case II: P8MW-L80M Blade Results

The description of the 80 m blade models is presented in Section 3.2. The models have 80 m blade tip radius, and the blade skin are reinforced with spar caps, and shear webs or composite tubulars. In the blade models with shear web configuration (SW-91, SW-86, SW-77, and SW-63 Models), their laminate thicknesses of the skin, spar caps, and shear webs are modified. In the blade model with composite turbular configuration (the CT Model), its laminate thicknesses of the skin and spar caps are maintained the same as SW-91 Model. Sandwich constructions consisting GF face and balsa core are

usually employed in the skin and shear web. The spar caps are composed of 85% UD-GF and 15% CF fabric layer. The composite tubulars have 0.1 m in diameter with a wall thickness of 0.01 m and stack with [0/90/30/-30]. For static analyses, the blade root in all models is fully constrained, and the surface forces (dP_Z and dP_Y), as shown in Figure 3.5, are applied along the Y-axis and Z-axis.

4.2.1 Static Analysis Results

4.2.1.1 Displacements

The global U1 and U2 displacement contours for SW-91 and the CT Models are presented in Figures 4.11 and 4.12, respectively. Note that the displacement contours are obtained at the loads associated with wind speed (u_w) of 11.0 m/sec.

The maximum values of U1 displacements for SW-91 and the CT Models are reported to be 0.142 m and 0.169 m, respectively. The negative U1 tip displacements of both SW-91 and the CT Models are observed due to bending. At any cross-section, the larger U1 displacements are found at the skin and spar cap sections instead of at leading or trailing edges.

In SW-91 and the CT Models, the U2 displacements are linearly decreasing along the local rotor radius. The maximum value of U2 displacements for SW-91 and the CT Models are 0.180 m and 0.216 m, respectively.

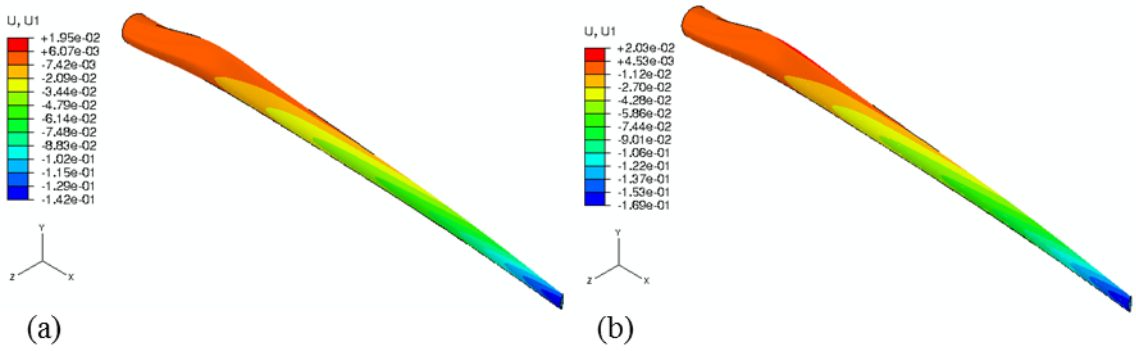

Figure 4.11. U1 (UX) displacement contours (u_w=11.0 m/sec): (a) SW-91, and (b) CT.

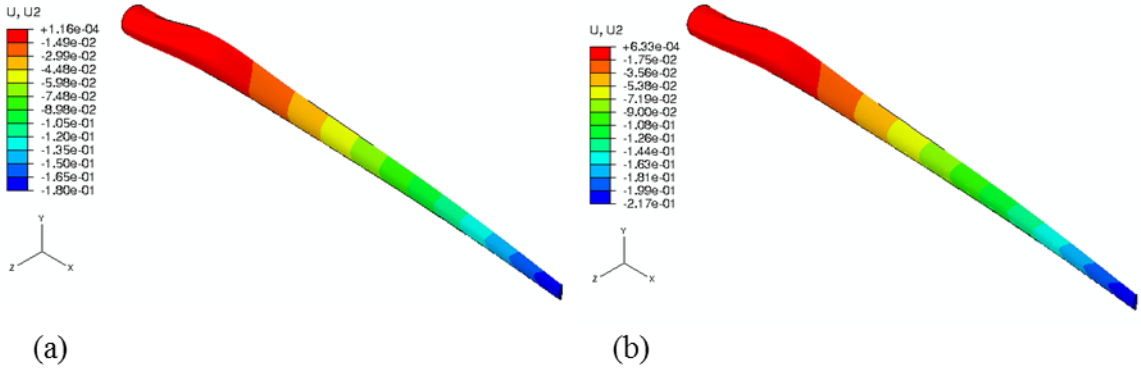

Figure 4.12. U2 (UY) displacement contours (u_w=11.0 m/sec): (a) SW-91, and (b) CT.

The global U3 displacement contours for all 80m blade models are presented in Figures 4.13. In all models SW-63 Model shows the largest U3 tip displacement of 4.27 m which corresponds to 5.62% of the blade length. The smallest U3 displacement of 3.48m is seen in SW-91 Model corresponding to 4.58% of the blade length. Thus, there are not significant differences in the U3 displacements among all the models.

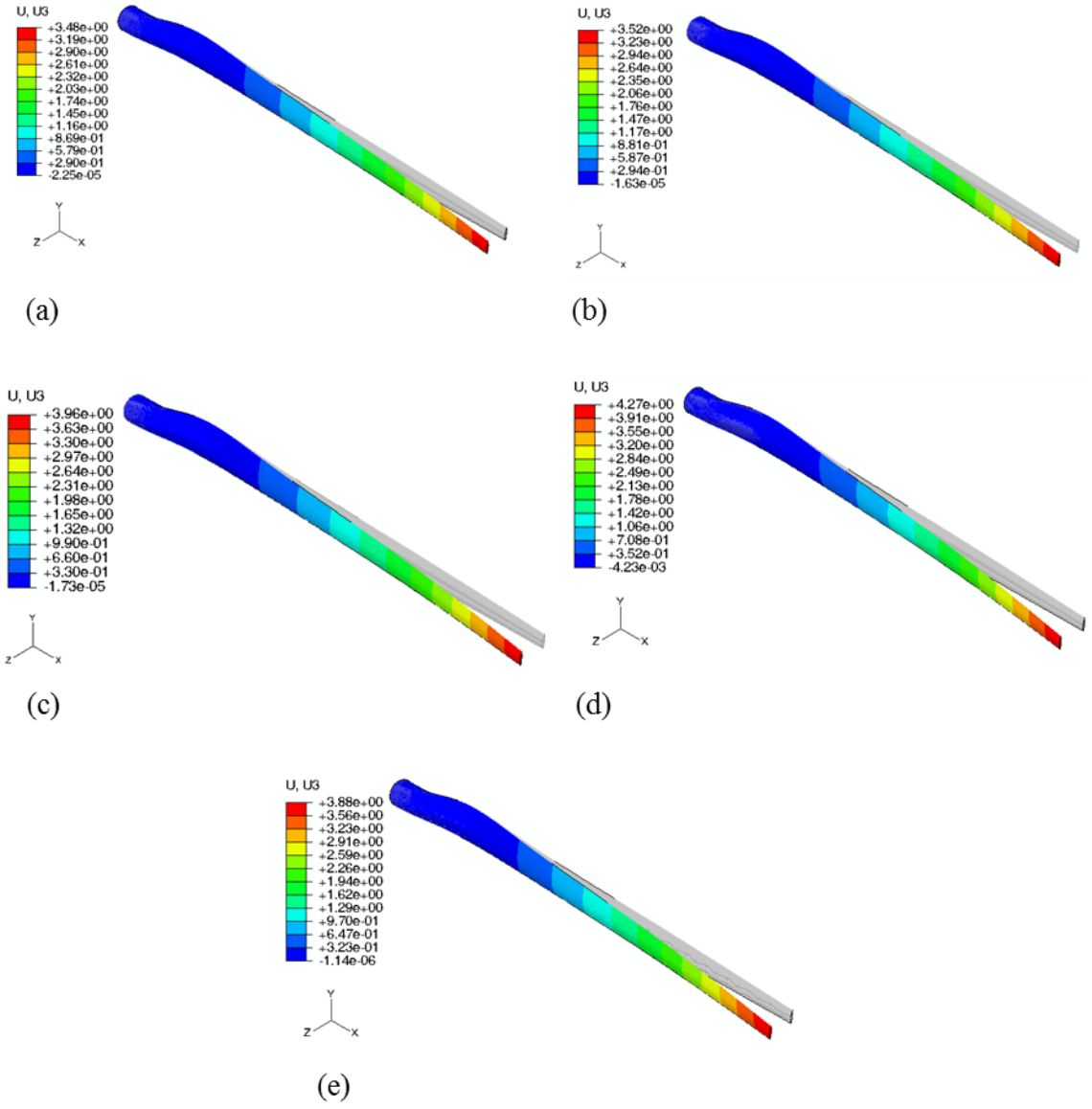

Figure 4.13. U3 (UZ) displacement contours (u_w=11.0 m/sec): (a) SW-91, (b) SW-86, (c) SW-77, (d) SW-63, and (e) CT.

The flapping (the Z-axis) bending rigidities along the local rotor radius (the X-axis) are estimated in conjunction with Figure 4.13 and Equation (2.11), and are

presented in Figure 4.14. The local rotor radius values in Figure 4.14 correspond to mid-point of eight sections depicted in Figure 3.5. For most of the models, bending rigidity near the root is about 10^5 times higher than it is in the vicinity of the tip. Once again, the rapid decline is seen immediately at the transition zone. The weight reduction contributes to decreasing the rigidity at the vicinity of the root. Note that the CT configuration does not affect the flapping bending rigidity in the airfoil section.

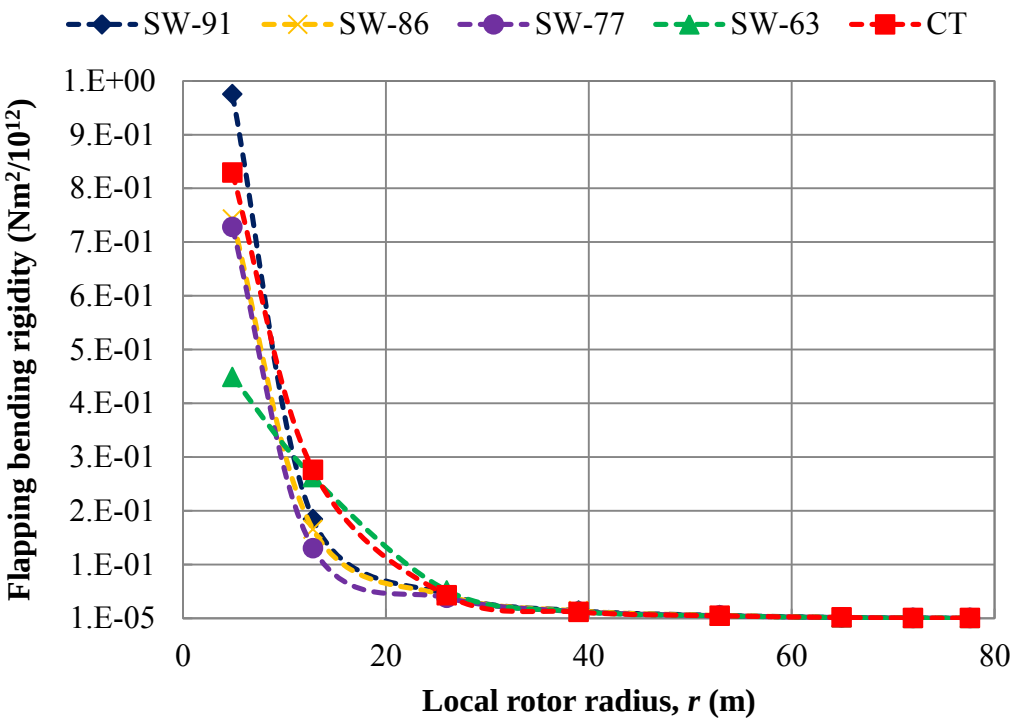

Figure 4.14. Flapping bending rigidity distribution for the five blade models.

The selected nodes for the tip displacements are presented in Figure 4.15, and the corresponding tip displacements are shown in Figure 4.16:

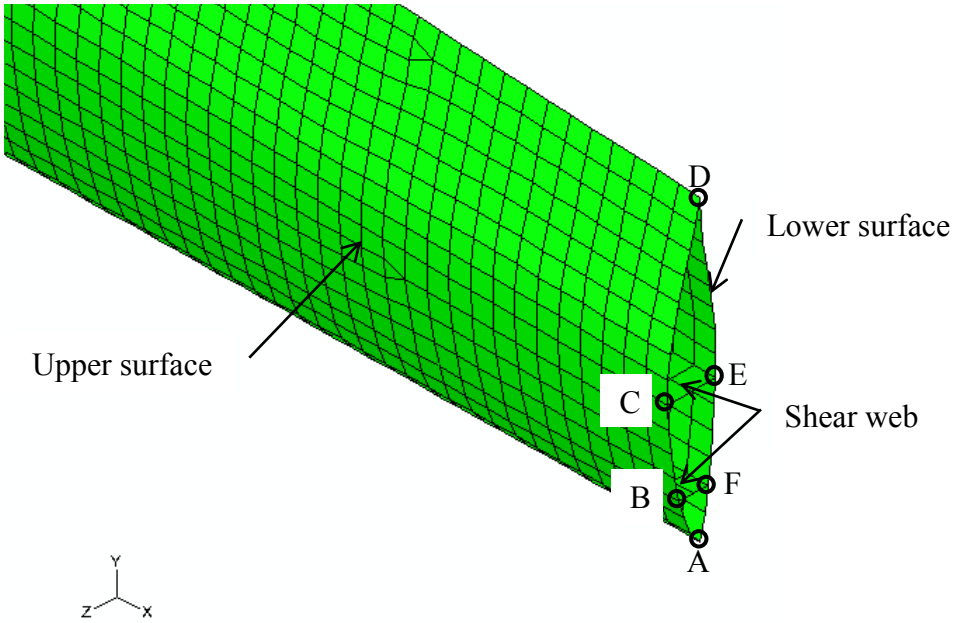

Figure 4.15. Selected nodes at the blade tip for five blade models.

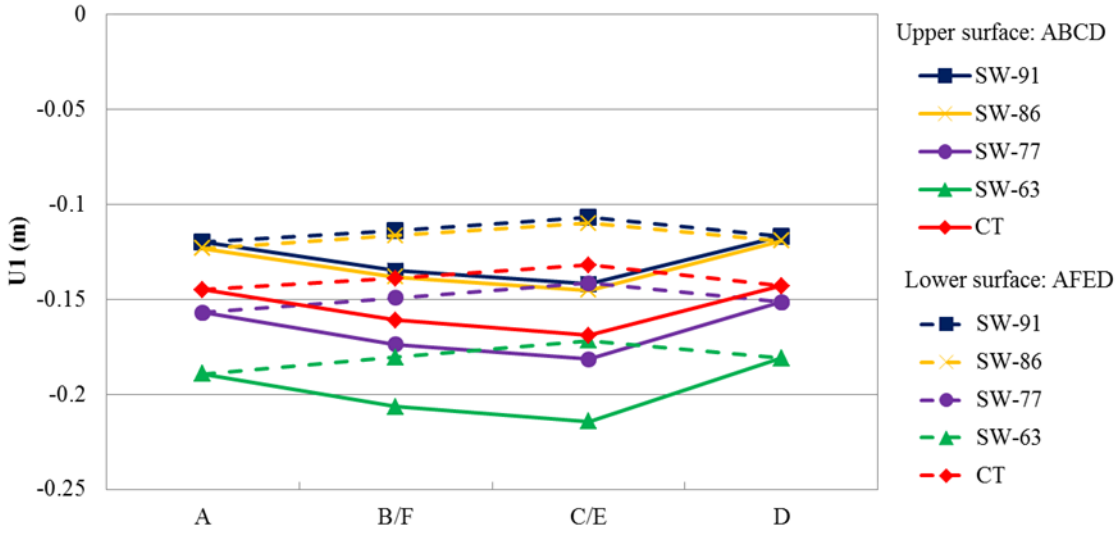

(a)

Figure 4.16. Comparison of the five blade models in tip displacement: (a) U1 (UX) displacement, (b) U2 (UY) displacement, and (c) U3 (UZ) displacement.

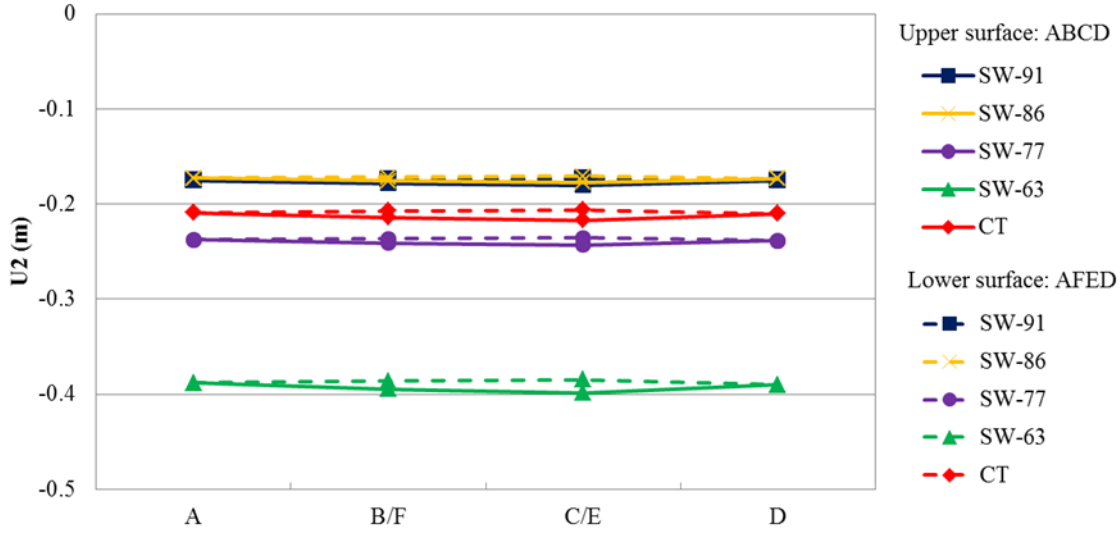

(b)

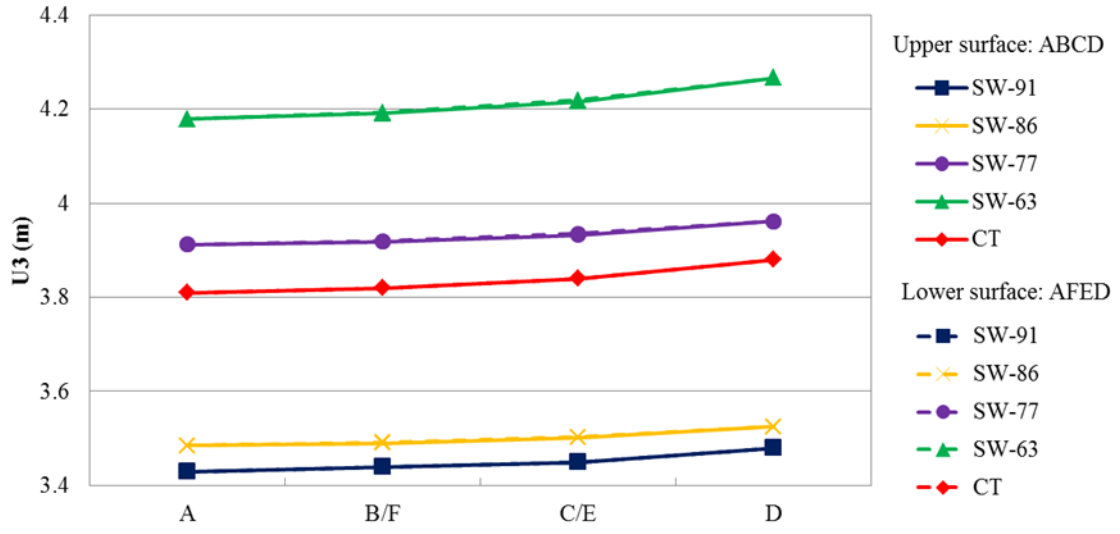

(c)

Figure 4.16. Continued.

For all models, the U3 displacements are much larger than the other displacement components. It is seen from Figure 4.16(c) that the original cross-section shape of all models is maintained after deformation. Larger displacements occur at the trailing edge (Point D in Figure 4.15) than at the leading edge (Point A in Figure 4.15); i.e., there is very small twist (up to 2.60°) about the X-axis in this model. As the model weight increases, the displacements increase. From Figure 4.16(c), the CT Model is deflected along the Z-axis less than SW-77 and SW-63 Model, and is more flexible than SW-91 and SW-86 Model. From Figure 4.16(b), the different core thickness between the forward and aft blade skin make an impact on the U2 displacements. In terms of SW-63 Model, there is a significant difference in the core thickness between the forward and aft blade skin. For the U2 displacement, the area moment of inertia about the neutral axis along the chord is strongly dependent on the distance between the neutral axis and aft blade skin location along the Y-axis. This area moment of inertia in SW-63 Model is smaller as compared with SW-91, SW-81, and SW-77 Models. Thus, the U2 displacements of SW-63 Model are much larger than those of the other models. Additionally, the tip displacements of SW-86 and SW-91 Models are close in value. Thus, the removal of the balsa core from the skin located on the spar cap may be allowed.

4.2.1.2 Stresses

Throughout these models, the stresses in the GF and CF layers are very small in comparison of their allowable strength. However, the von Mises stresses are rather high

in the balsa core of the sandwich laminates. Herein, the stress contours for the root section, the blade skin, and internal reinforcements are presented in the order of the blade models.

4.2.1.2.1 SW-91 Model

The maximum Hashin criteria in all composite layers is 0.11, which is for below the damage state value of 1. Therefore, no damage in the GF and CF layers in the root, skin, spar cap, and shear web is observed.

S11 and S22 stress contours in the outermost GF fabric layer of the root section, local rotor radius (r) of 4 m – 5.6 m, are presented in Figure 4.17. Since the root section has cylindrical cross-section, the S11 and S22 stress fields are symmetric with respect to the X-Y plane. The maximum value of the S11 stresses is 5.57 MPa and appears at the constrained end. Similarly, the maximum value of the S22 stress is 0.934 MPa at the constrained end. The surface above and below the Y-axis are subjected to compression and tension, respectively.

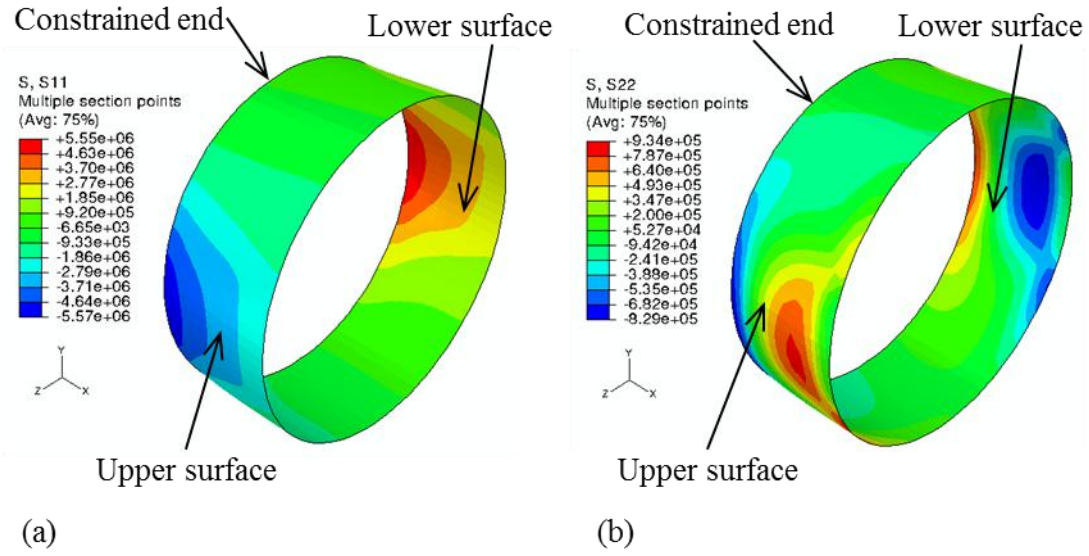

Figure 4.17. Stress contours in the outermost GF fabric layer ([**fabric**/fabric/fabric/fabric]) of the root section (4 m < r 5.6 m) for SW-91 (u_w=11.8 m/sec): (a) S11 stress, and (b) S22 stress.

The stresses in the airfoil section that follows the root section are discussed next. S11 stresses in the outermost GF fabric layer of the skin are presented in Figure 4.18. Note that overall the upper skin experiences compressive stresses while the lower skin is tension. The highest compressive and tensile S11 stress of the GF fabric layer is 36.1 MPa and 38.3 MPa, respectively, and occurs where the blade skin is attached to the spar cap between r = 20 m and r = 32 m as seen in Figures 4.18(a) and 4.18(b). These values are much smaller as compared with the allowable strength (X_T =367 MPa and X_C =549 MPa). Note that in this section, the skin has both the thicker airfoil cross-section, and thickness sandwich laminate are laminate and these dimensions affect the area moment of inertia properties leading to the higher stresses. Furthermore, S11 stresses decrease

along the length toward the tip. In the vicinity of the tip, tensile (1.36 MPa) and compressive (0.139 MPa) S11 stress appear in the upper and lower skin, respectively. The complex blade geometry of three different airfoil shapes and taped thickness leads to coexistence of tensile and compressive S11 stresses in the same surface (Figures 4.18(c) and 4.18(d)). There is not a significant difference in the S11 stress field between the upper and lower skin.

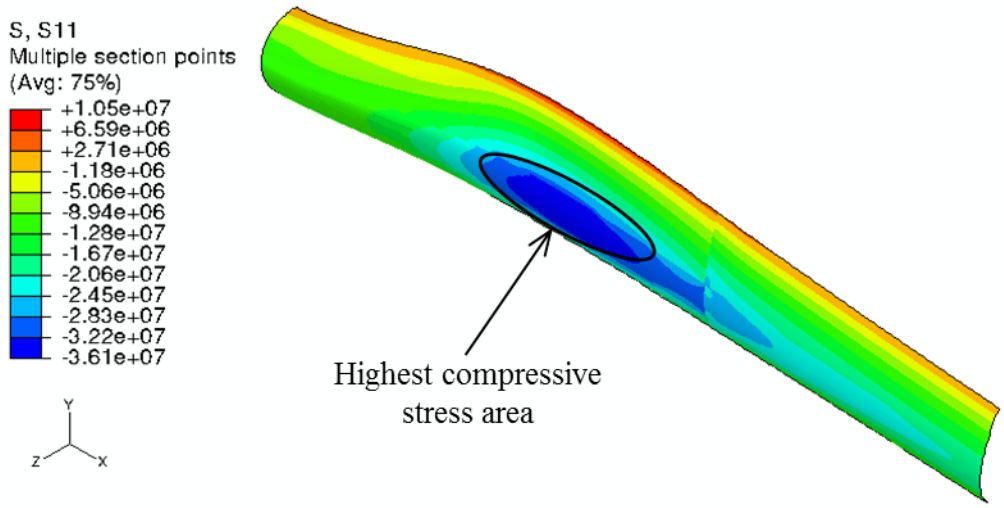

(a)

Figure 4.18. S11 stress contour in the outermost GF fabric layer ([**fabric**/core/fabric]) of the skin for SW-91 (u_w=11.8 m/sec): (a) upper skin (5.6 m < r < 46 m), (b) lower skin (5.6 m < r < 46 m), (c) upper skin (46 m < r < 80 m), and (d) lower skin (46 m < r < 80 m).

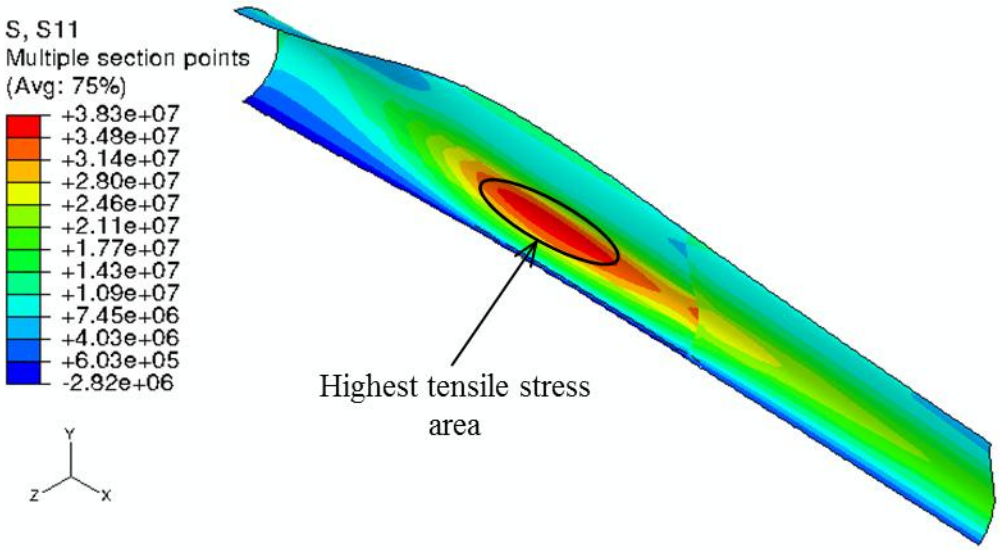

(b)

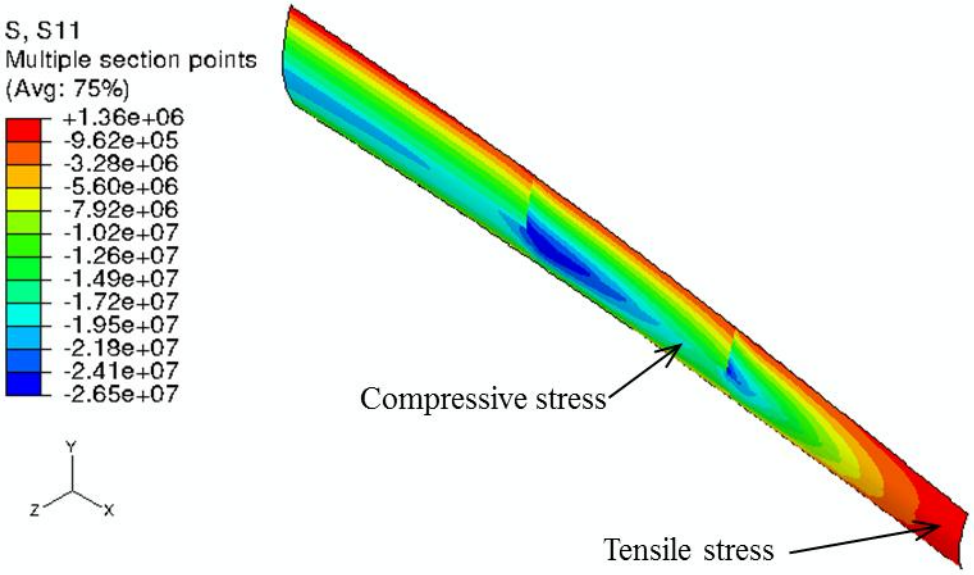

(c)

Figure 4.18. Continued.

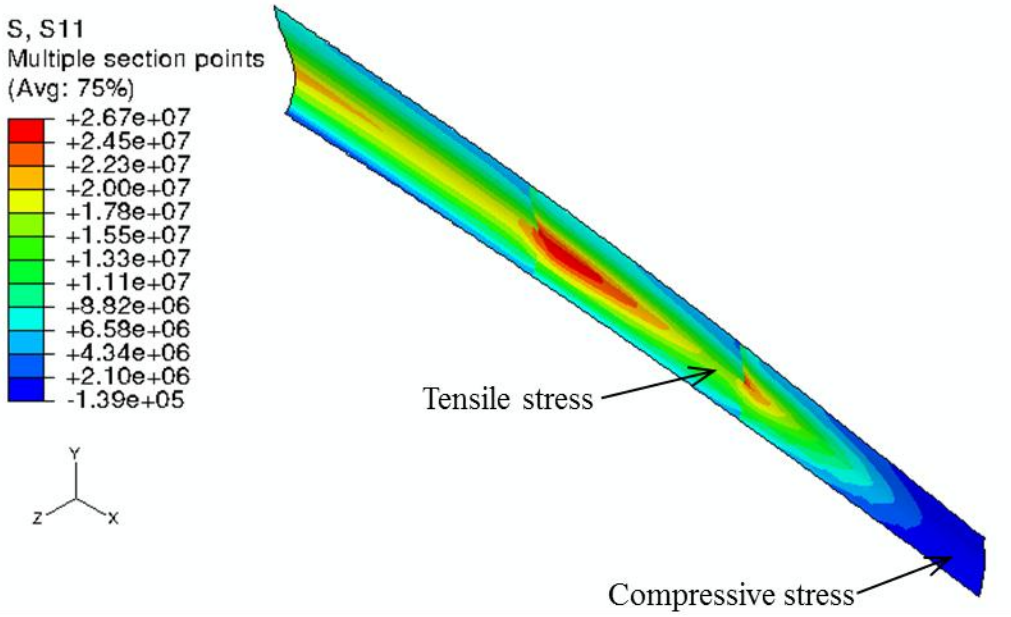

(d)

Figure 4.18. Continued.

S22 and S12 stresses of the transition region where cylindrical cross-section meets airfoil cross-section are presented in Figure 4.19. The outermost GF fabric layer of the upper skin undergoes compressive S22 stresses at the skin with spar cap reinforcement. Away from the spar caps, in the skin section, only tensile S22 Stresses occur as shown.

The positive and negative S12 stresses coexist in Region 1 where the skin is attached to the shear web as depicted in Figure 4.19(b). The surface with positive S12 stress is described by the skin with spar cap, and the negative S12 stress occurs in the skin only. Region 2 and Region 3 in the upper skin, respectively, experience positive and

negative S12 stress fields, attributed to the changes in the blade geometry; Region 2 is located at the transition, whereas Region 3 is at the airfoil.

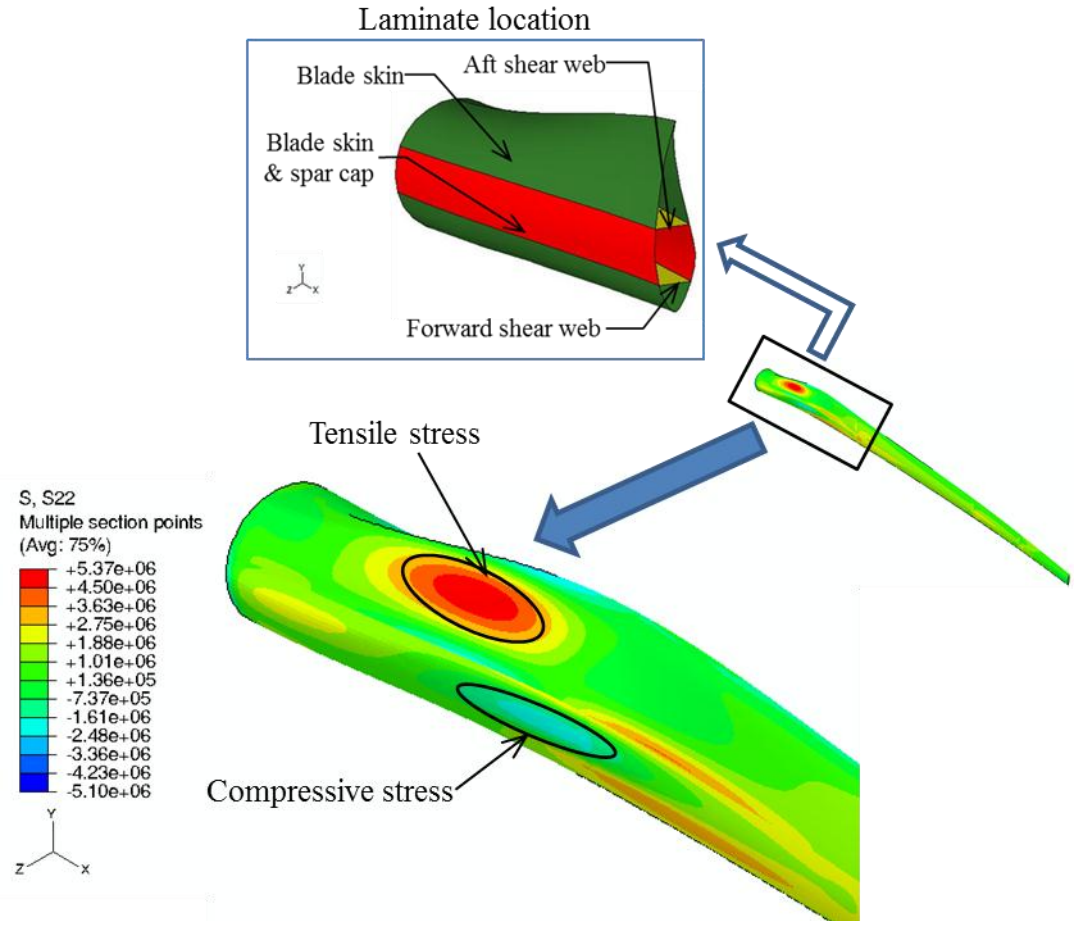

(a)

Figure 4.19. Stress contours in the outermost GF fabric layer ([**fabric**/core/fabric]) of the skin for SW-91 (u_w=11.8 m/sec): (a) S22 stress, and (b) S12 stress.

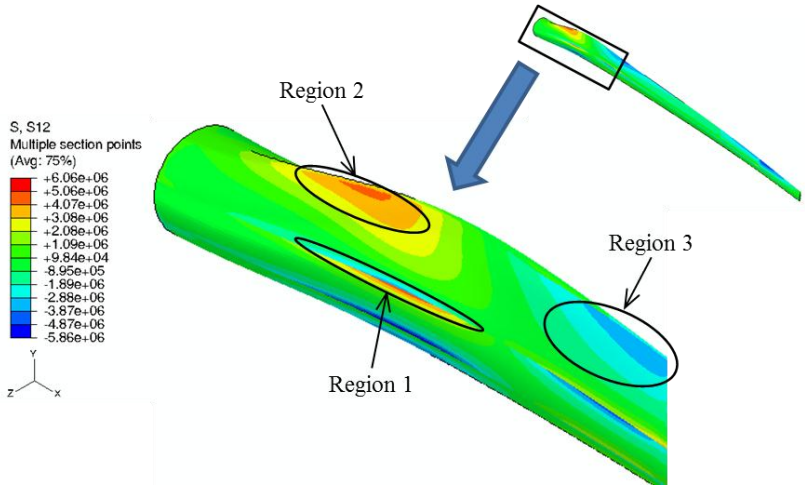

(b)

Figure 4.19. Continued.

The von Mises stresses in the balsa core of the skin are presented in Figure 4.20. The damage of the balsa core of the upper skin is initiated at wind speed of 11.8 m/sec, while the highest von Mises stress is 5.99 MPa in compression, exceeding its allowable strength (5.4 MPa). The damaged area is located at the skin and spar cap sections between r = 20 m and r = 32 m (Figure 4.20(a)). From Figure 4.20(b), the highest von Mises stress in the balsa core of the lower skin is 6.53 MPa in tension which is below its allowable strength (7 MPa). In general, there is no significant difference in the stress of the balsa core in the upper and lower skin. The von Mises stresses decrease to about 4.23 kPa at the tip.

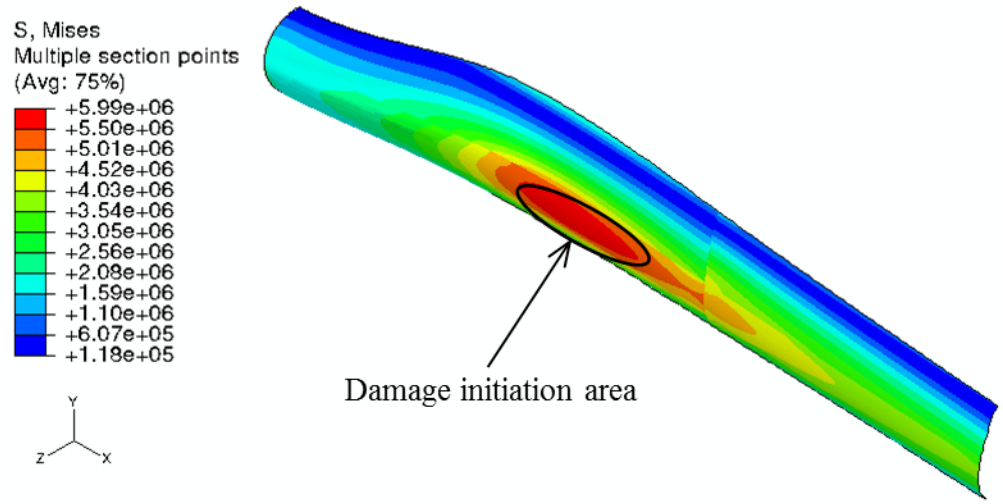

(a)

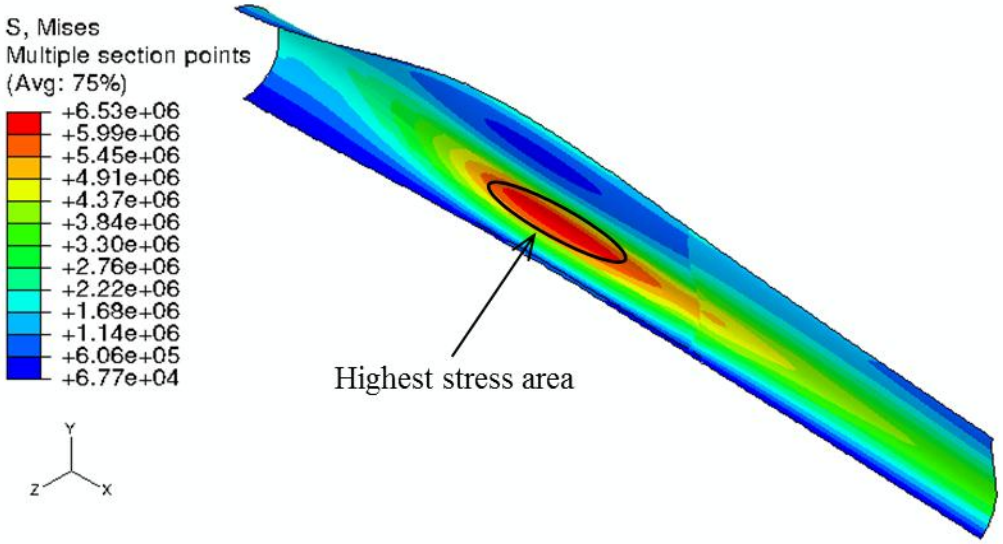

(b)

Figure 4.20. Von Mises stress contour in the balsa core ([fabric/**core**/fabric]) of the skin for SW-91 (u_w=11.8 m/sec): (a) upper skin (5.6 m < r < 46 m), (b) lower skin (5.6 m < r < 46 m), (c) upper skin (46 m < r < 80 m), and (d) lower skin (46 m < r < 80 m).

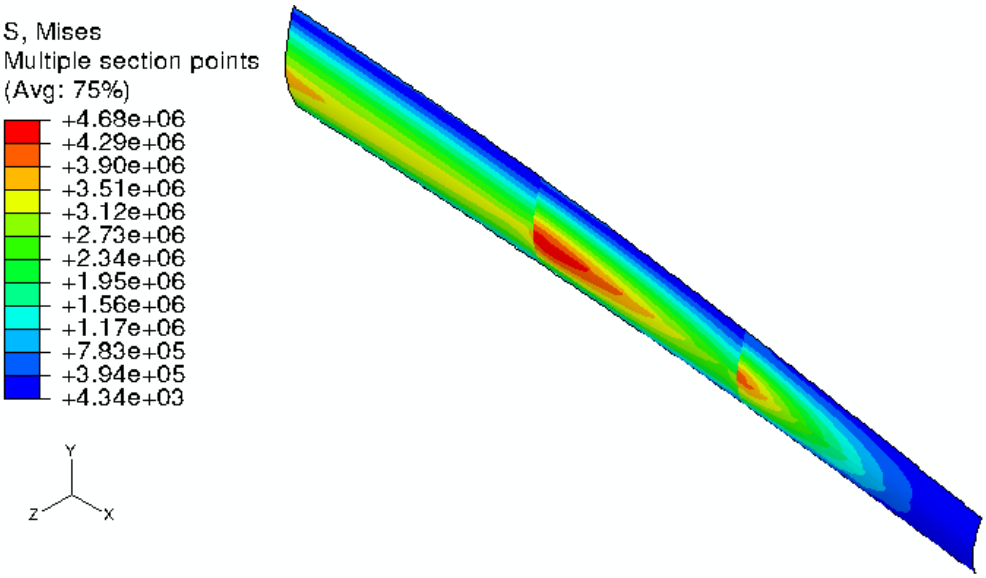

(c)

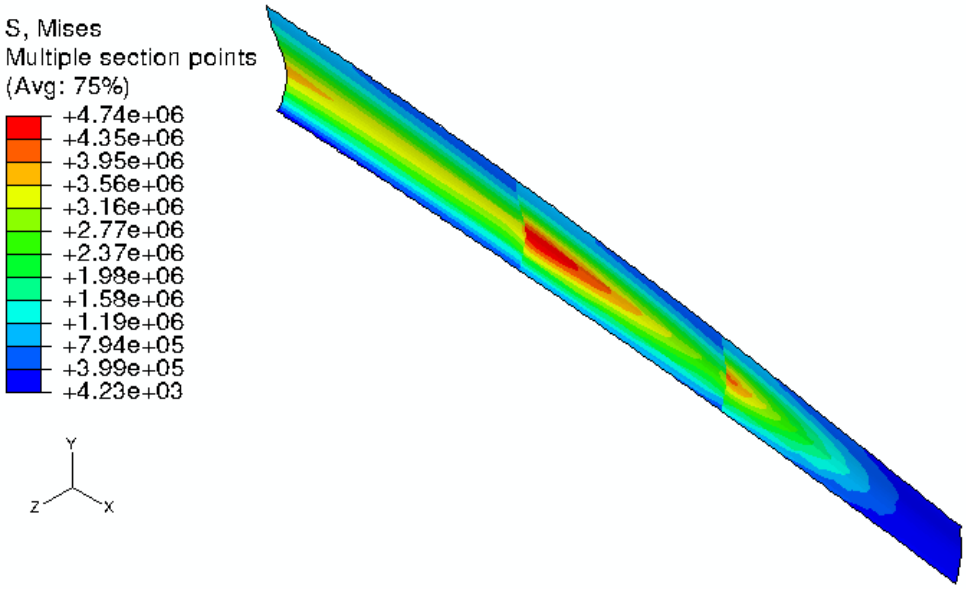

(d)

Figure 4.20. Continued.

The other location with sandwich constructions is in the shear web reinforcement. The von Mises stresses in the balsa core of the webs are presented in Figure 4.21. The surface attached to the lower skin is designated as LS and similarly, US designates the surface adjacent to the upper skin. The maximum von Mises stress in the balsa is 4.41 MPa, located between r = 20 m and r = 32 m (Figure 4.21(a)). In the webs at any local rotor radius, the higher von Mises stresses appear at all surfaces where is reinforced with spar caps. As seen before, the von Mises stresses decrease along the local rotor radius approaching the tip. The von Mises stress at the tip is about 7.05 kPa.

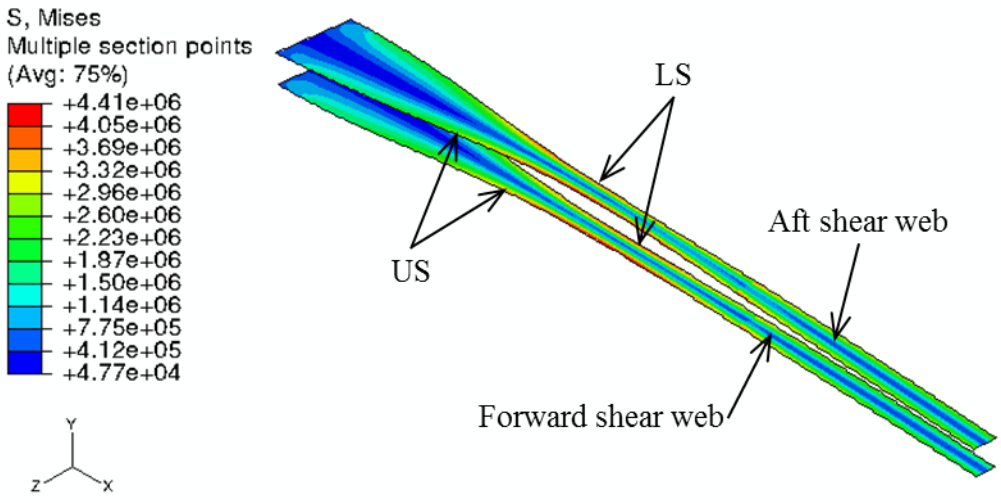

Figure 4.21. Von Mises stress contours in the balsa core ([fabric/45/-45/**core**/-45/45/fabric]) of the webs for SW-91 (u_w=11.8 m/sec): (a) 4 m < r < 46 m, and (b) 46 m < r < 80 m.

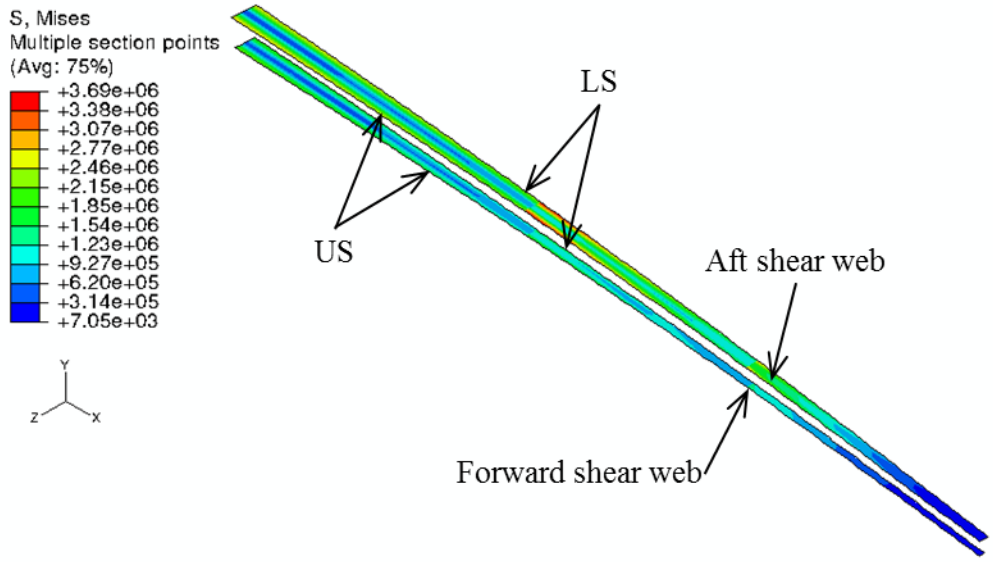

(b)

Figure 4.21. Continued.

The spar cap laminate consisting of twelve layers ([CF fabric/UD-GF/CF fabric/UD-GF/CF fabric/UD-GF]$_s$) is studied to understand the S11 stress fields. We designate layers as Layer-1, the innermost layer (CF fabric) to Layer-12, the outermost layer (again CF fabric). As shown in Figure 4.22, the highest compressive S11 stress is observed in Layer-12 to be 58.1 MPa at the upper surface, between r = 20 m and r = 32 m. This value diminishes along the blade length to 2.28 kPa at the tip. The S11 stress in Layer-12 is higher than that in the outermost GF fabric layer. This is due to two factors; the different material properties, and the difference in layer thickness of the skin (9.09 mm) and spar cap (1.5 mm).

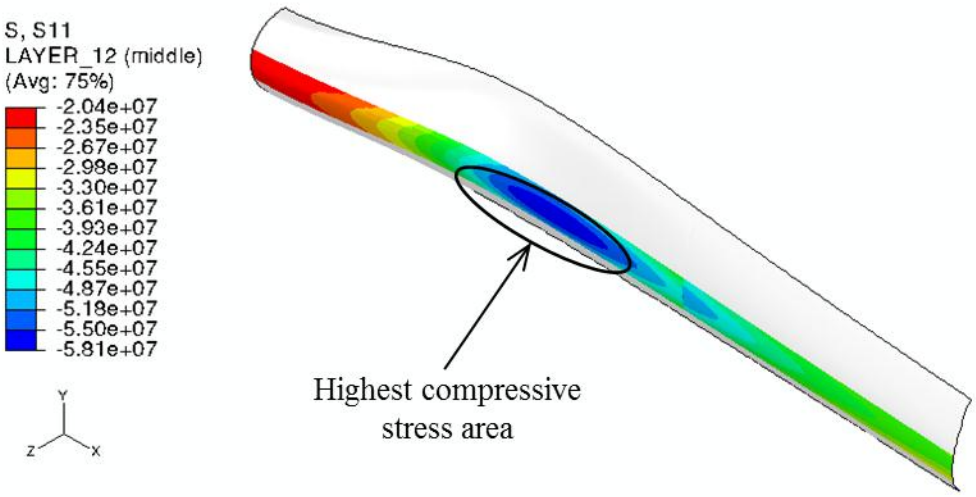

(a)

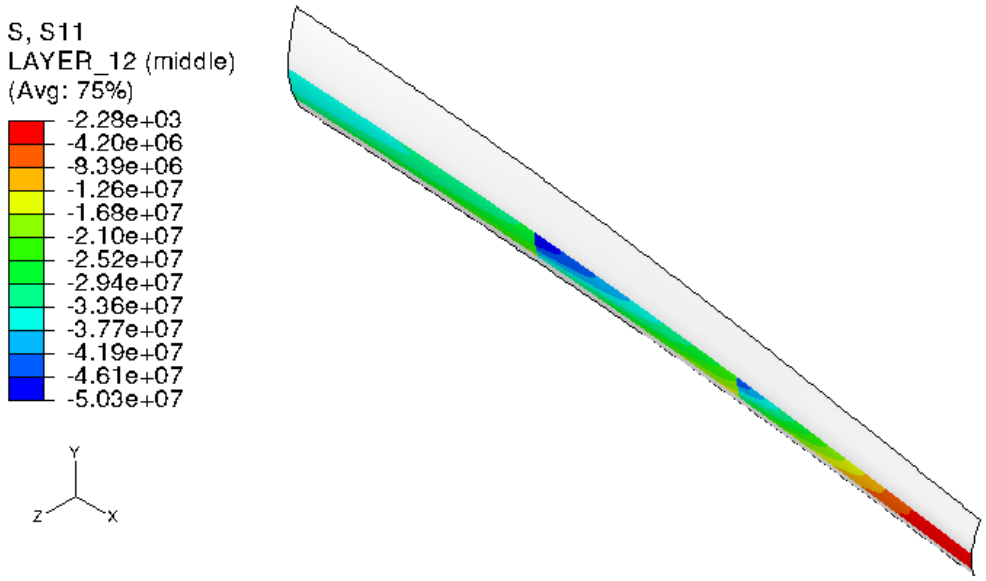

(b)

Figure 4.22. S11 stress contours in the outermost CF fabric layer (Layer-12) of the upper spar cap for SW-91 (u_w=11.8 m/sec): (a) 5.6 m < r < 46 m, and (b) 46 m < r < 80 m.

4.2.1.2.2 SW-86 Model

In this model, the balsa core is removed from the blade skin reinforced with spar caps in SW-91 Model. Only the von Mises stresses in the balsa core of the skin and webs, between r = 5.6 m and r = 32 m, are presented in Figure 4.23. Since the skin is not of sandwich construction at the spar cap, it provides much higher strength. The balsa core is presented in the forward blade skin, and is at the location where initial damage is observed at u_w=12.6 m/sec. The von Mises stress (5.57 MPa) at the damage initiation location is above its allowable strength (5.4 MPa). However, at that location, the boundary nodes are all shared skin and web, creating an inaccurate internal distribution. Additionally, the maximum von Mises stress in the core of the web is observed to be 5.09 MPa. Note that any GF and CF layers in this model are not damaged since the maximum Hashin criteria (0.15) is below the damage state value.

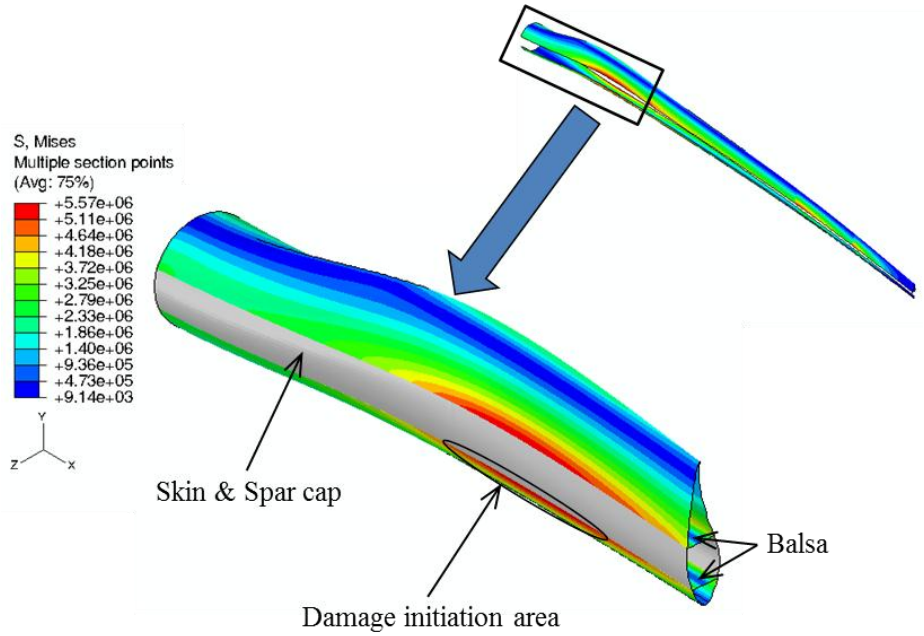

Figure 4.23. Von Mises stress contour in the balsa core ([face/**core**/face]) of the skin and webs for SW-86 (u_w=12.6 m/sec).

4.2.1.2.3 SW-77 Model

The core thickness of sandwich constructions in this model is reduced by one-third compared with the core thickness of SW-91 Model. Since it is reported that the damage initiation location of SW-91 Model is in the upper blade skin, the von Mises stresses in the balsa core of the upper skin and stress field in the outermost GF fabric layer of the upper skin are presented in Figures 4.24 and 4.25, respectively:

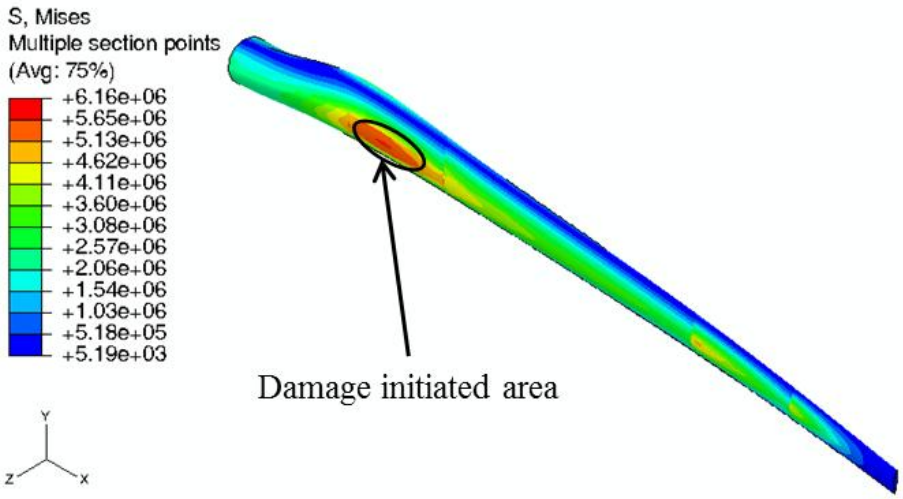

Figure 4.24. Von Mises stress contour in the balsa core ([fabric/**core**/fabric]) of the upper skin for SW-77 (u_w=11.0 m/sec).

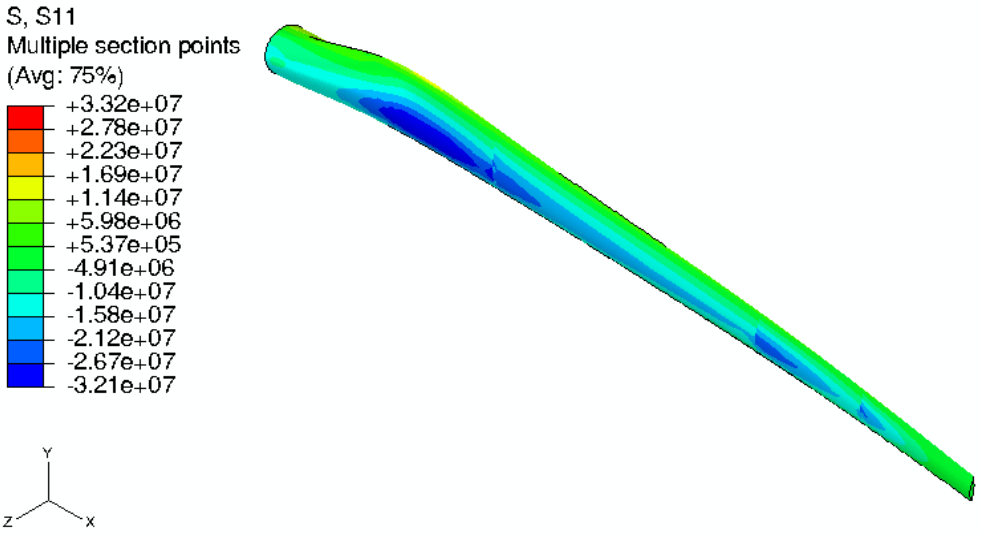

(a)

Figure 4.25. Stress contours in the outermost GF fabric layer ([**fabric**/core/fabric]) of the upper skin for SW-77 (u_w=11.0 m/sec): (a) S11 stress, (b) S22 stress, and (c) S12 stress.

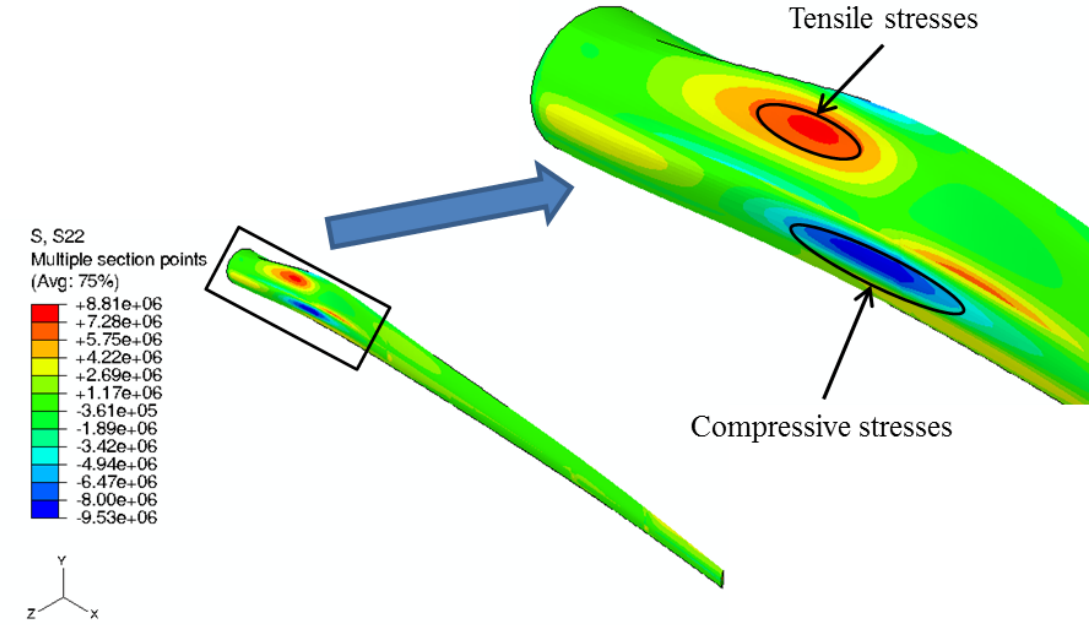

(b)

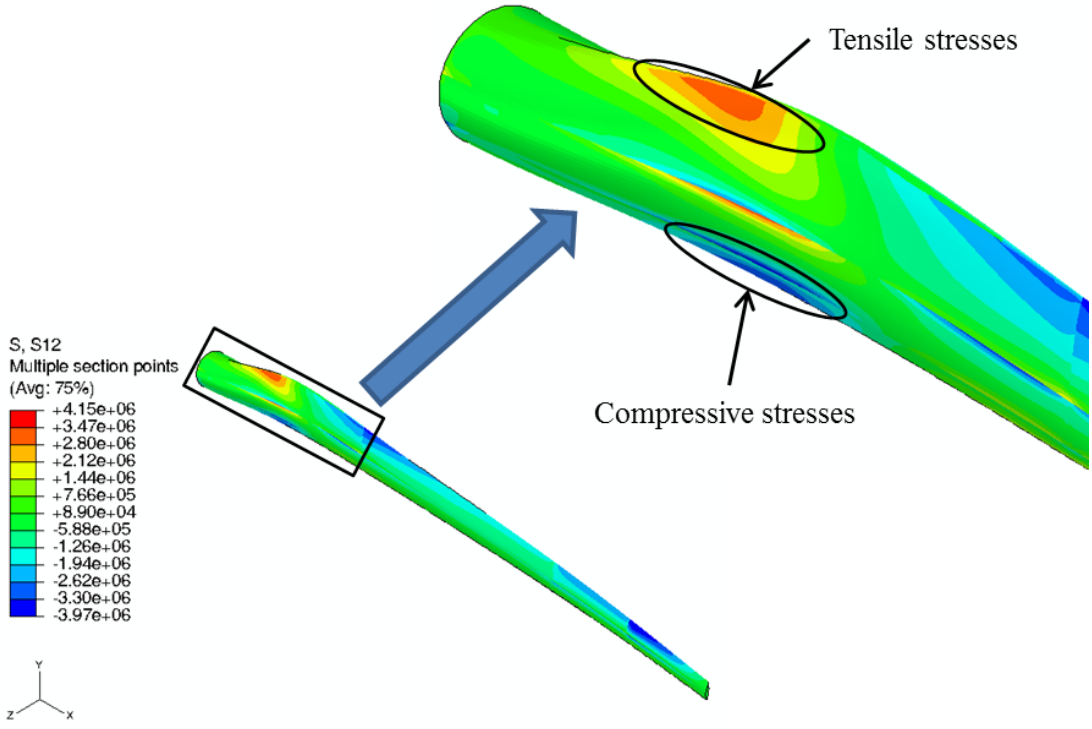

(c)

Figure 4.25. Continued.

The initial damage in the core appears at the highest von Mises stress (6.16 MPa) region of Figure 4.24 at u_w=11.0 m/sec. Due to reducing the core thickness, the area moment of inertia about the mid plane of the sandwich construction significantly decreases from SW-91 Model to this model. However, the stress distribution in the outermost layer, as shown in Figures 4.25, is similar as compared with the stress field of SW-91 Model. This thickness change is not crucial to increase the stress field in the face (GF fabric layer) of the sandwich construction. SW-77 Model has less strength than SW-91 Model. Remark that the maximum von Mises stress in the core of the web is 4.27 MPa, and the Hashin criteria in the GF and CF layers is below 0.18.

4.2.1.2.4 SW-63 Model

Laminate thicknesses in the airfoil section of this model are determined based on Griffin's blade model [11,30,31]. Furthermore, there are no balsa cores in the skin of this model whose location is the same as SW-86 Model. As discussed previously, the balsa core in the skin is initially damaged. Therefore, the von Mises stress in the balsa core of the skin is presented in Figures 4.26. The balsa core in the forward blade skin is damaged at u_w=11.8 m/sec since the von Mises stress (5.59 MPa) exceeds its allowable strength. The maximum value of the von Mises stress in the core of the web is 4.96 MPa. The damage of balsa core and composite materials in the root section, skin, spar caps, and webs are not observed. For - 45° GF layer of the web at the transition, the criteria for compressive matrix cracking mode is 0.919, as presented in Figure 4.27. This value is

much higher than the maximum Hashin criteria of the other models since the -45° GF layer (0.5 mm) is thinner than that of the other models (2.27 mm).

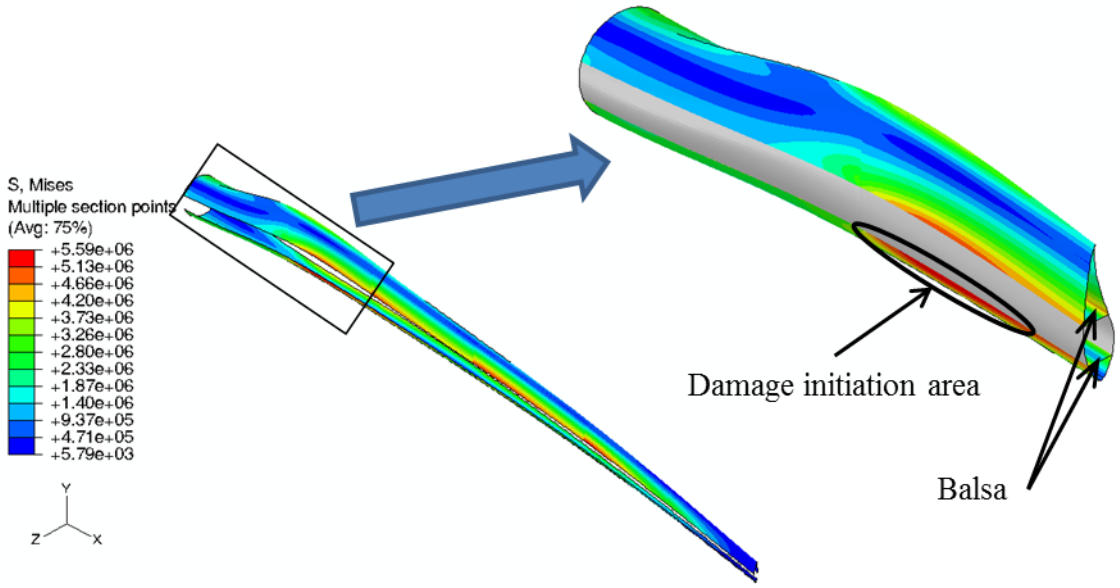

Figure 4.26 Von Mises stress contour in the balsa core ([fabric/**core**/fabric]) of the skin for SW-63 (u_w=11.8 m/sec).

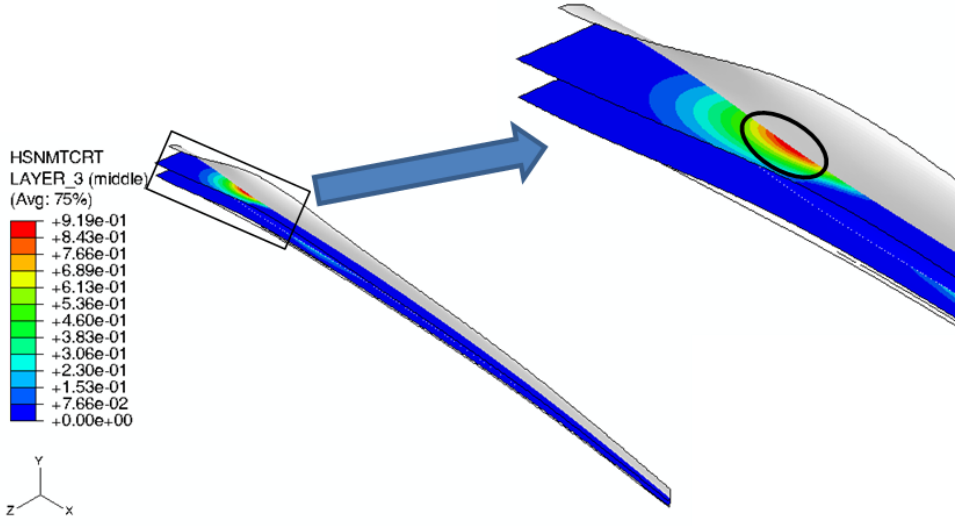

Figure 4.27. Hashin criteria contours in the -45° GF layer ([fabric/45/-**45**/core/-45/45/fabric]) of the webs for SW-63 (u_w=11.8 m/sec).

At the transition, the thickness of the skin and spar cap laminates (15.2 cm) is much thicker than thicknesses of the remaining section (2.3 cm – 7.6 cm). Thus, all stress components in the outermost GF fabric layer of the transition section are much lower since the transition is much stiffer and stronger. This can be seen in the S11 stress distribution in the outermost GF fabric layer of the skin (Figures 4.28).

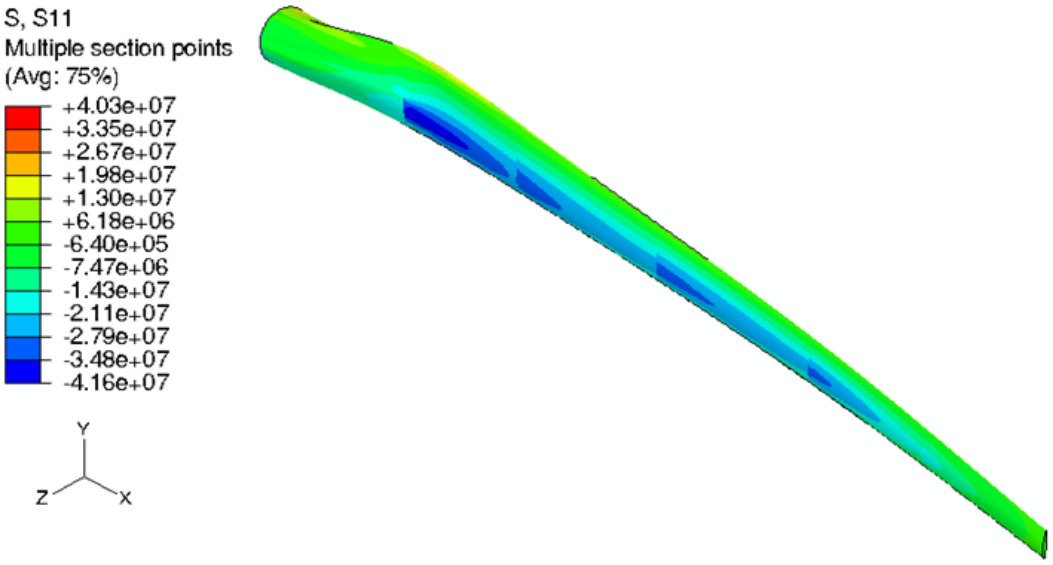

Figure 4.28. S11 stress contours in the outermost GF fabric layer ([**fabric**/core/fabric]) of the skin for SW-63 (u_w=11.8 m/sec).

4.2.1.2.5 CT Model

The von Mises stress in the balsa core of the skin is presented in Figures 4.29. The von Mises stress in the balsa core of the skin exceeds its allowable strength, while

the value for the maximum Hashin criteria in the composite layer of the skin is 0.018. The upper skin and lower skin are subjected to compressive and tensile stresses, respectively. The lower skin, between r = 5.6 m and r = 46 m, experiences the highest stress in the balsa core of 6.33 MPa almost reaching its allowable strength of 7MPa. Since the bending moments are inversely proportional to the local rotor radius, the von Mises stresses of the balsa core at the upper and lower skin at the tip decrease to 12.4 kPa and 13.2 kPa, respectively. The von Mises stress field is similar between the upper and lower skin. At the any give cross-section, the von Mises stresses are lower in the skin toward the leading or trailing edges as shown in Figure 4.29. There are two different types of damage shown: stress concentrations at the tubular-skin attachments for any layer, and higher von Mises stress in the core caused by bending in the flapping direction. Since the contact area between the tubulars and skin is small, higher von Mises stresses are generated in the skin core. In the upper skin, it is observed the balsa core exceeds its allowable strength at three different tubular-skin attachment locations shown in Figures 4.29(a) and 4.29(c). It is also noted that the core thickness tapers along the blade length leading to higher stresses.

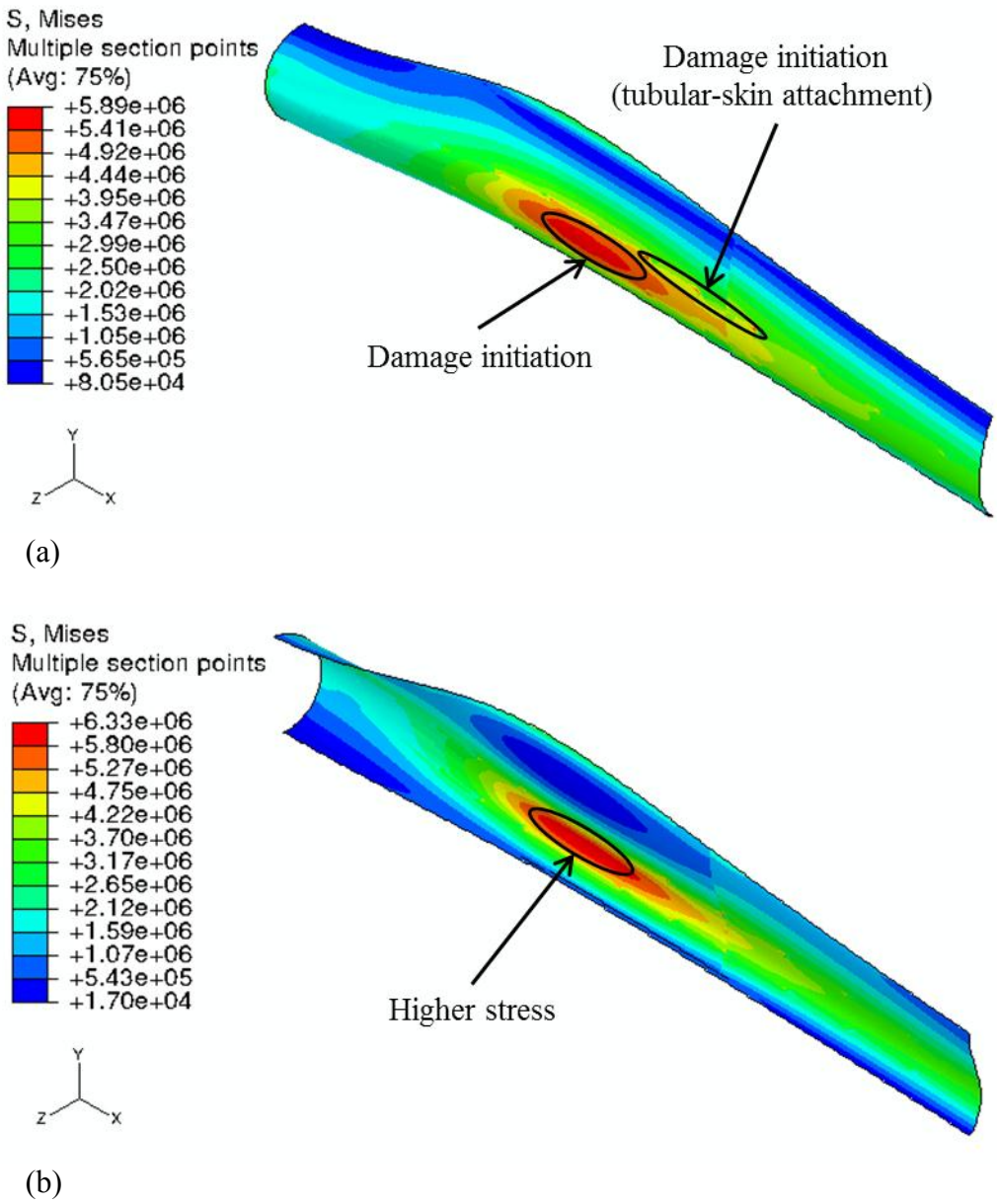

Figure 4.29. Von Mises stress contour in the balsa core ([fabric/**core**/fabric]) for CT (u_w=11.0 m/sec): (a) upper skin (5.6 m < r < 46 m), (b) lower skin (5.6 m < r < 46 m), (c) upper skin (46 m < r < 80 m), and (d) lower skin (46 m < r < 80 m).

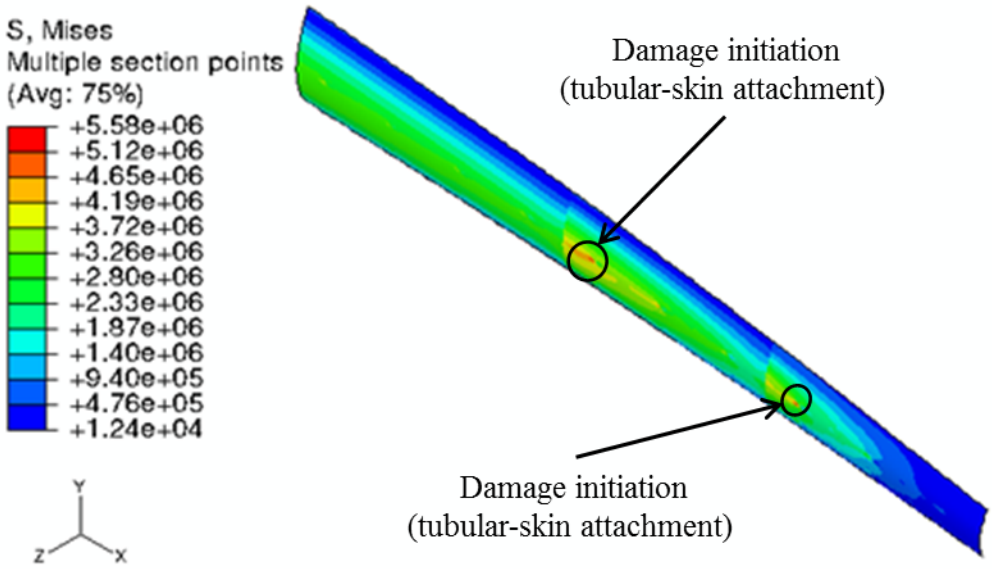

(c)

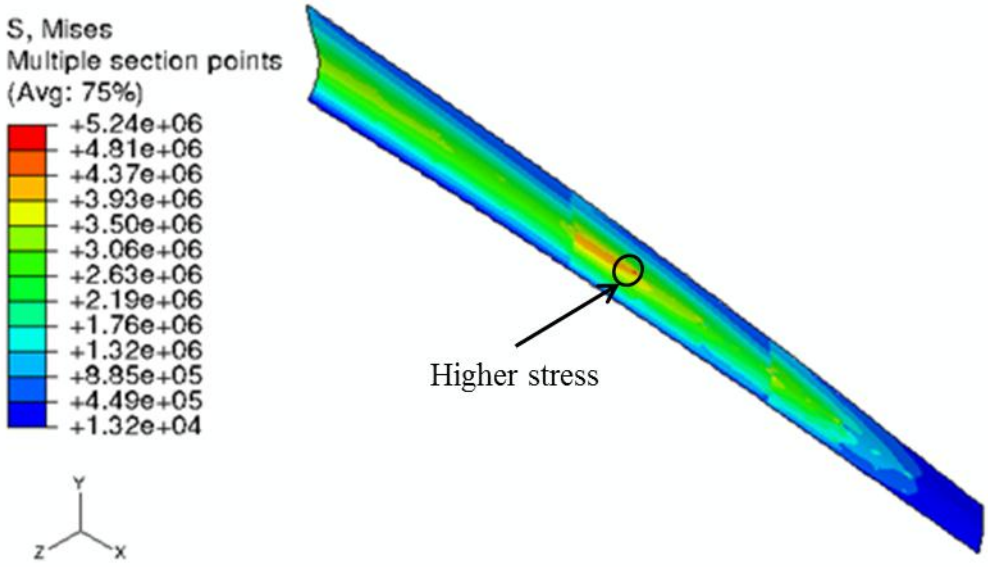

(d)

Figure 4.29. Continued.

The S11 stress in the outermost CF fabric layer (Layer-12) of the spar cap is presented in Figures 4.30:

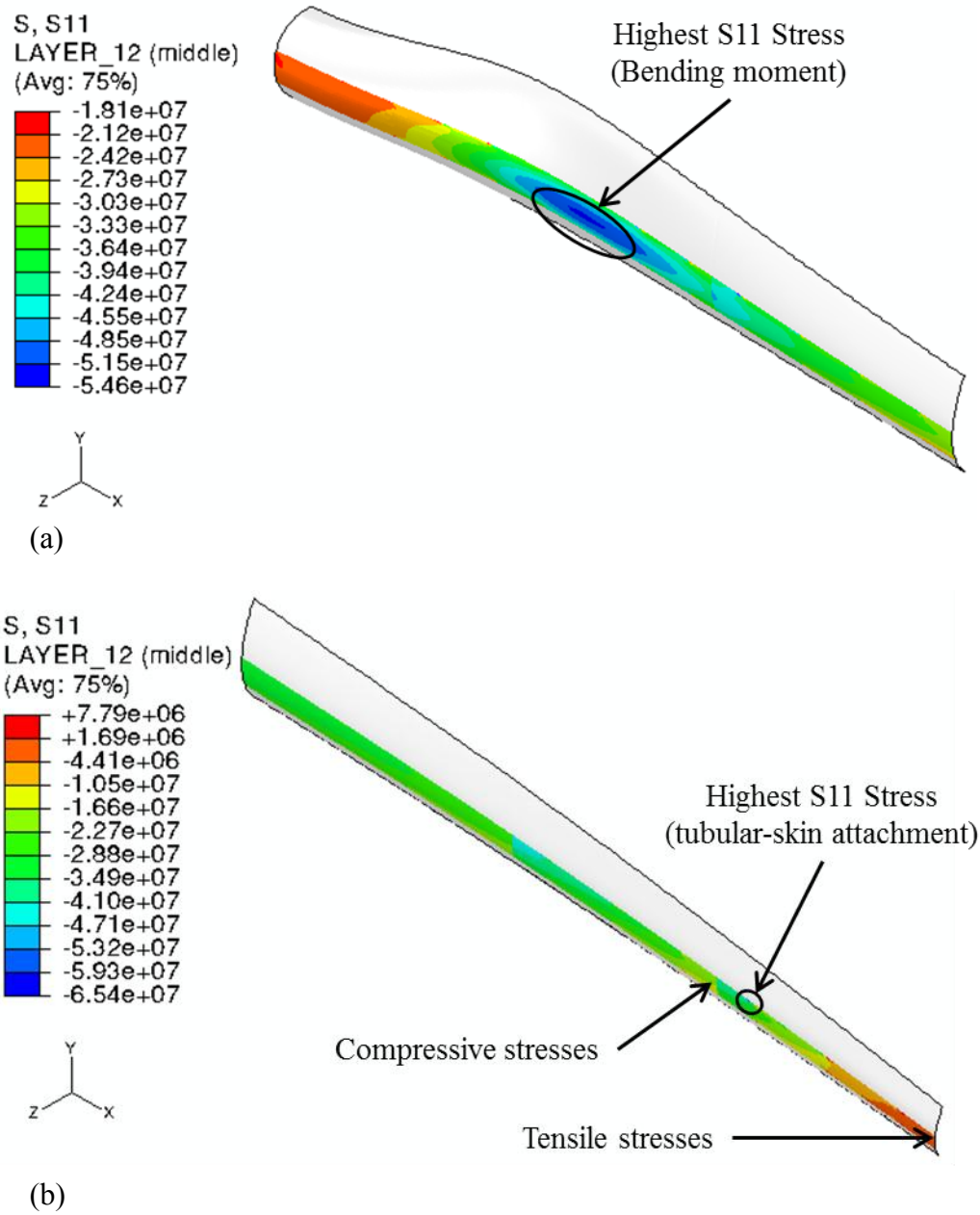

Figure 4.30. S11 stress contour in the outer most CF fabric layer (Layer-12) of the spar cap for CT (u_w=11.0 m/sec): (a) upper spar cap skin (5.6 m < r < 46 m), and (b) upper spar cap skin (46 m < r < 80 m).

The S11 stresses decreases along the local rotor radius, and there is no difference in the magnitude of S11 stress between the upper and lower spar caps. In the spar cap, between r = 5.6 m and r = 46 m, the maximum S11 stress is seen to be 54.6 MPa due to bending moments. In the spar cap, between r = 46 m and r = 80 m, the maximum value of the S11 stress is observed to be 65.4 MPa due to the tubular-skin attachments and the thinner laminate thickness. As seen in Figures 4.30(b), in the upper spar cap, the compressive S11 stress becomes tensile stress at the vicinity of the tip where combined bending moments exist.

S11 and S12 contours in the composite tubulars, between r = 5.6 m and r = 32 m, are shown in Figure 4.31. Note that S11 stress in composite tubulars is much higher than S12 stress. S11 stresses in the forward composite tubulars are lower than in the aft composite tubulars. This is attributed to the distance from leading edge which is 15% and 45% of chord length. In aft composite tubulars, between r = 15.6 m and r = 20 m, the maximum axial stress experienced is about 67.2 MPa. The diagonal tubulars carry loads and are subjected to more stress than horizontal tubulars. In the diagonal tubulars, both tensile and compressive stresses occur as seen in Figure 4.31. As discussed in Appendix E, this is dependent on the loading direction and tubular orientation. Materials with higher axial strength are preferable for diagonal tubulars.

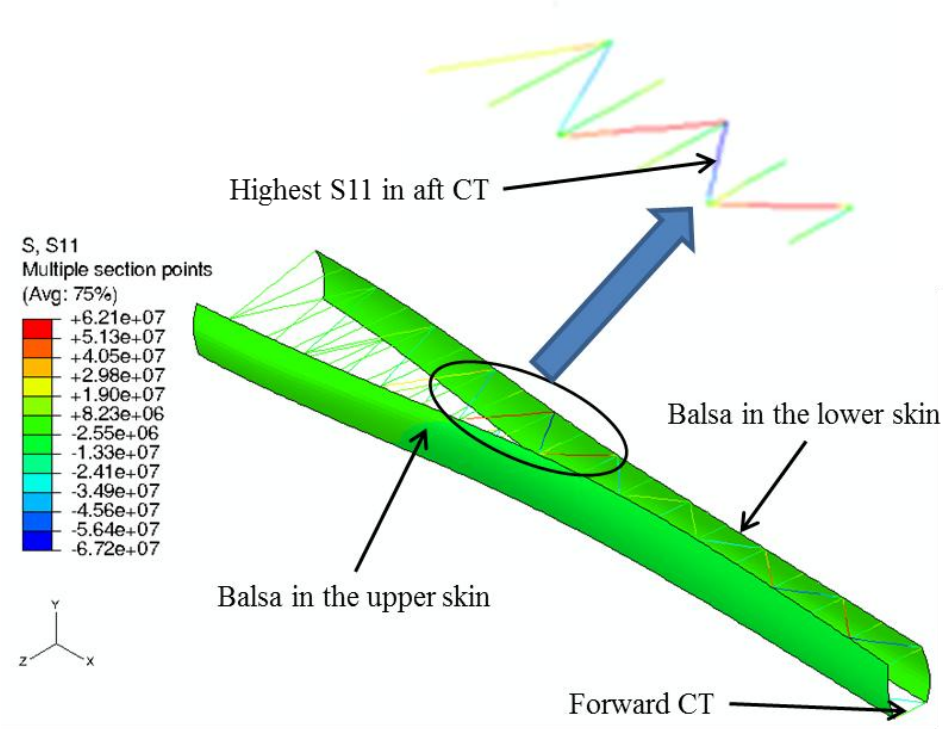

(a)

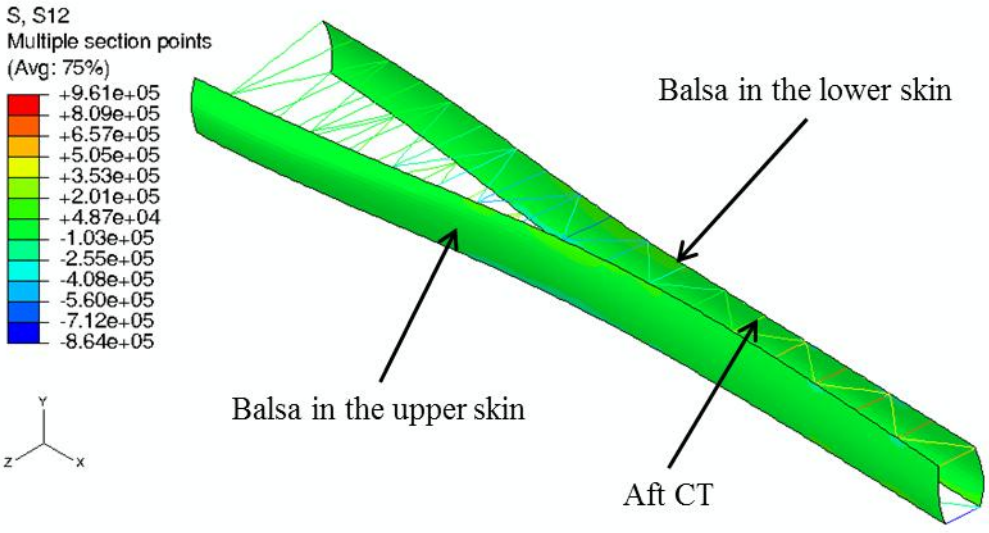

(b)

Figure 4.31. Stress contours in the composite tubulars skin (5.6 m < r < 32 m) for CT (u_w=11.0 m/sec): (a) S11 stress, and (b) S12 stress.

"*Buckling considerations*" based on Euler-column formula for fixed-fixed column are considered for composite tubulars which displayed compressive stresses [48]. For the longest tubulars of 4.2 m, the critical buckling load per unit area is 50 MPa; FEM simulation shows less than 1 MPa as shown in Figure 4.31(a). For the tubulars experiencing the highest S11 stress, the buckling load is 220 MPa which is much higher than 67.2 MPa as experience in the FEM analyses. Therefore, the compressive stresses do not cause composite tubulars to buckle.

4.2.2 Natural Frequencies

The first mode natural frequencies for the five blade models are presented in Figure 4.32, and the corresponding flapping, edge, and torsional mode shapes are shown in Figures 4.32-4.36.

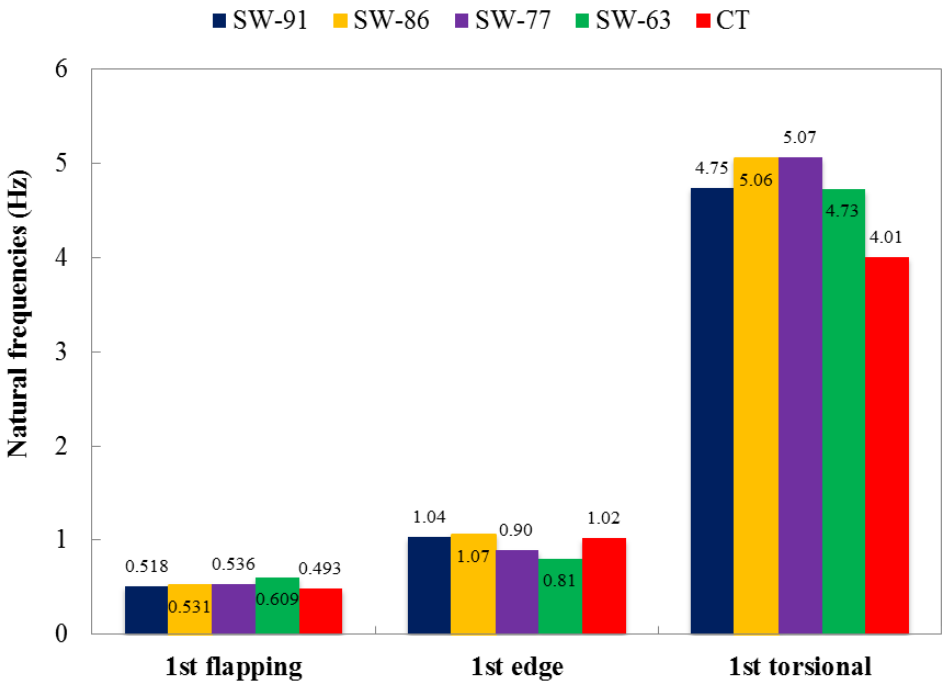

Figure 4.32. Comparison of the five models in the first mode natural frequencies.

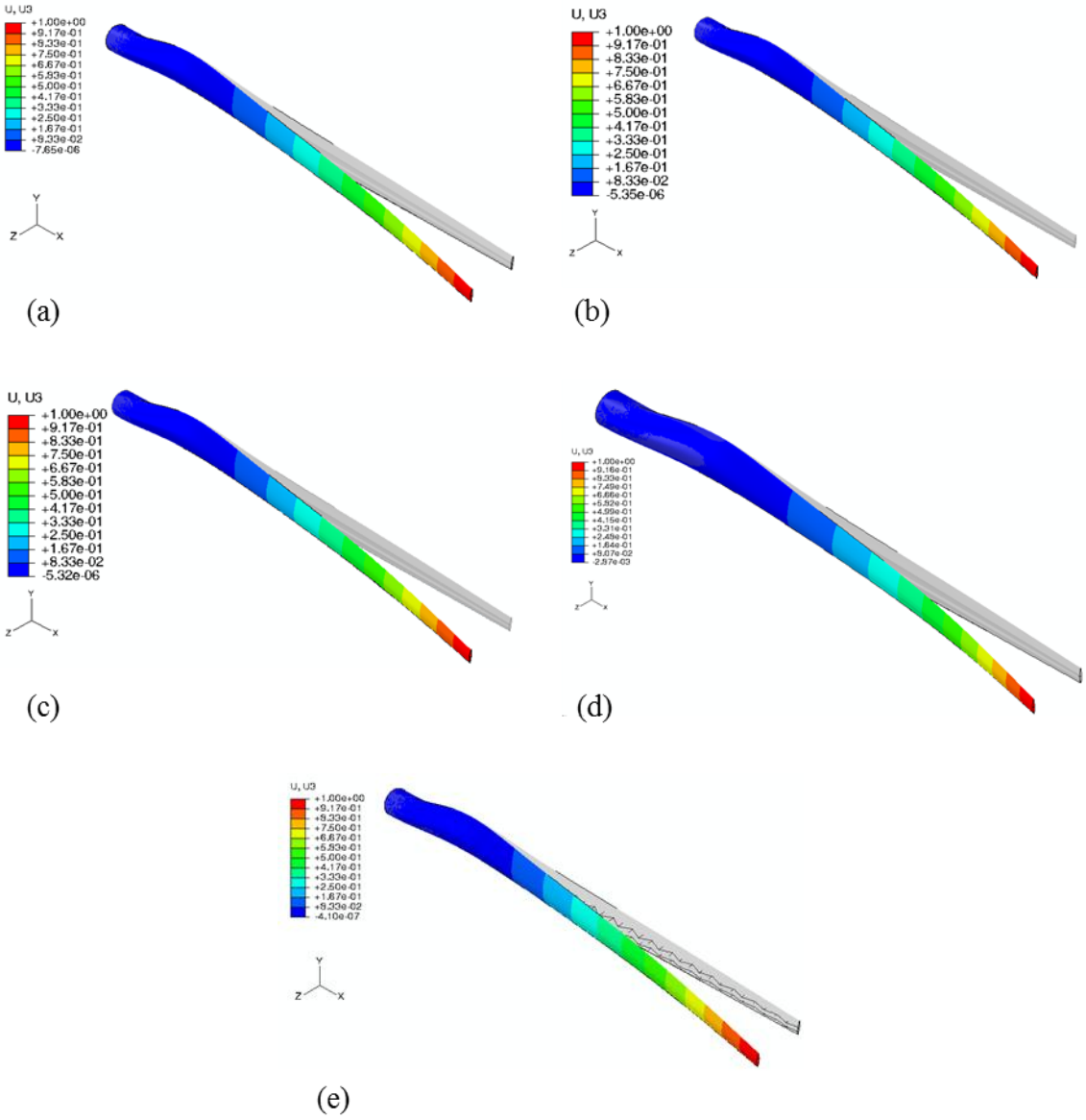

Figure 4.33. The first flapping mode shapes: (a) SW-91, (b) SW-86, (c) SW-77, (d) SW-63, and (e) CT.

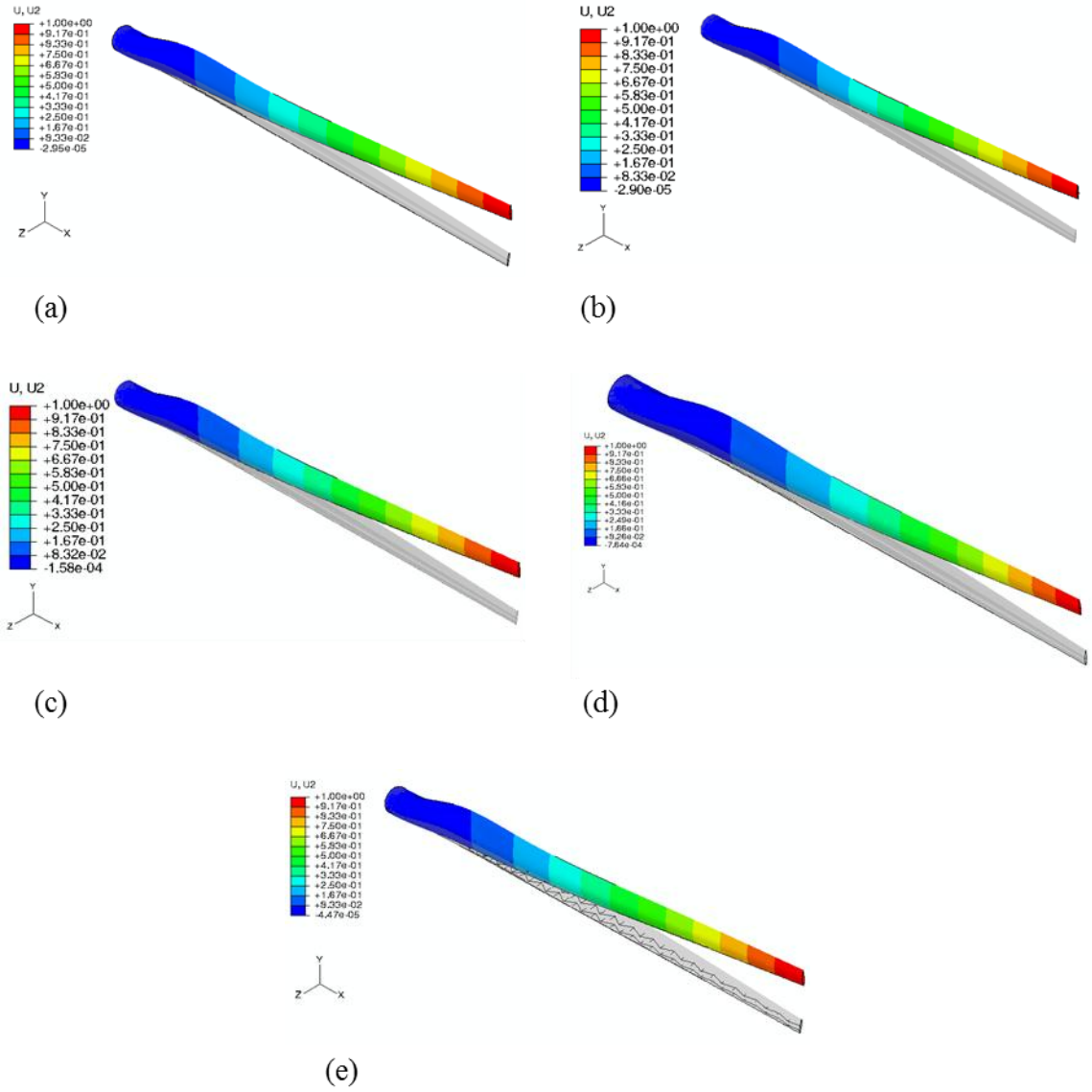

Figure 4.34. The first edge mode shapes: (a) SW-91, (b) SW-86, (c) SW-77, (d) SW-63, and (e) CT.

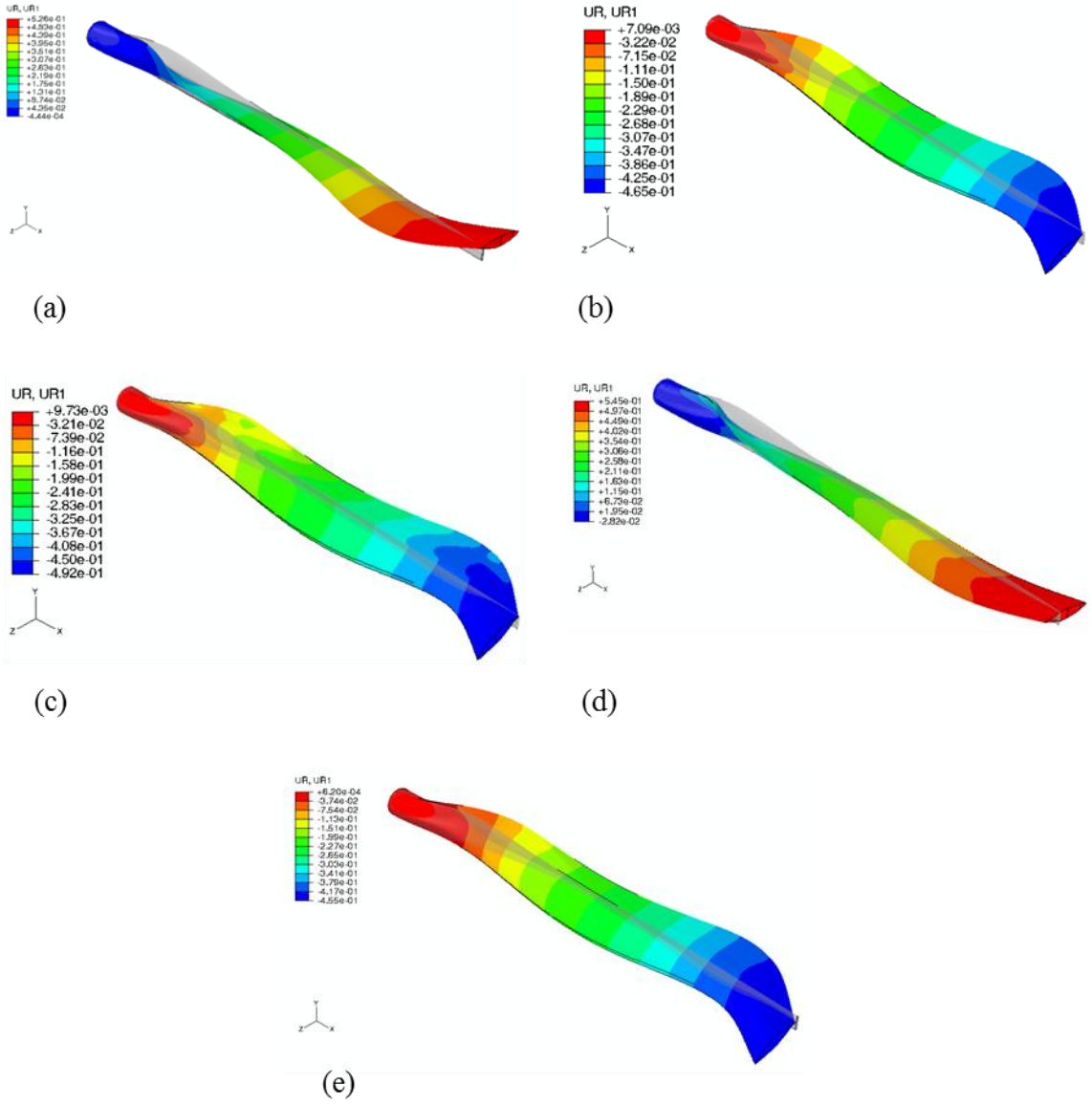

Figure 4.35. The first torsional mode shapes: (a) SW-91, (b) SW-86, (c) SW-77, (d) SW-63, and (e) CT.

Since the rotational speed of the blade ranges from 0 and 0.3 Hz, the lowest natural frequency of the blade needs to be above this range. The extracted natural frequencies in all models exceed this range. Furthermore, the lowest natural frequency can be expected to be much higher than 0.3 Hz due to influence of natural frequency of the other components such as the tower and drive train.

SW-86, SW-77, SW-63, and the CT Models are compared with SW-91 Model, which is treated as a baseline. SW-86 Model has closer flapping and edge natural frequency since the other component properties dominate in these modes. However, SW-86 Model contributes to increasing torsional natural frequency. Torsional natural frequency is generally dependent of the ratio of shear modulus to density of the materials. The balsa core of the skin in SW-86 Model is not considered. Therefore, the torsional stiffness of the blade of SW-86 Model increases.

In SW-77 Model, the change in thickness of the balsa core causes the edge natural frequency to be lower than SW-91 Model. The aft blade skin is located far away from the origin of the blade XYZ coordinate system as compared with the location of the forward blade skin. The moment of inertia and stiffness of the aft blade skin dominate the edge stiffness. As the ratio of the face to the core in the sandwich constructions is increased, their effective elastic modulus is also increased. The flapping and torsional natural frequencies of SW-77 Model are improved from SW-91 Model.

The flapping natural frequency of SW-63 Model is higher than that of the other models. The edge natural frequency of SW-63 Model is lowest in all models because of

the effect of area moment of inertia for the aft blade skin. However, the lowest natural frequency is still the flapping mode in SW-63 Model.

The CT Model provides less torsional natural frequency than the other models. Composite tubulars do not increase the edge natural frequency since the tubulars are not located far from the axis passing through the centroid of the cross-section.

Figures 4.33-35 show that the first mode shapes for each motion are pure. In the torsional mode, the mode shapes of SW-91 and SW-63 Models are positively twisted about the X-axis while the other mode shapes are negatively twisted. The coupling mode (bending and twisting) may appear in higher natural frequencies since the model does not provide substantial torsional rigidity. This is shown in the third edge mode shapes presented in Figure 4.36. The strong coupling mode appears in the CT Model. The other mode shapes show that the blade in the vicinity of the tip is twisted.

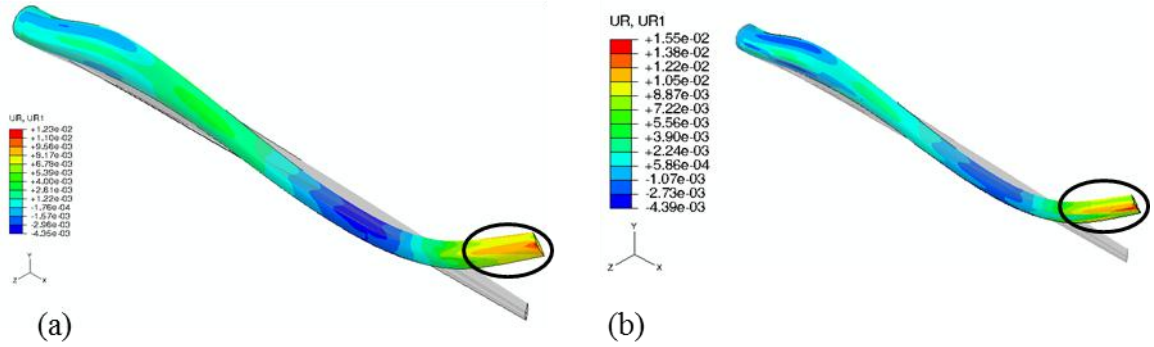

Figure 4.36. The third edge mode shapes: (a) SW-91, (b) SW-86, (c) SW-77, (d) SW-63, and (e) CT.

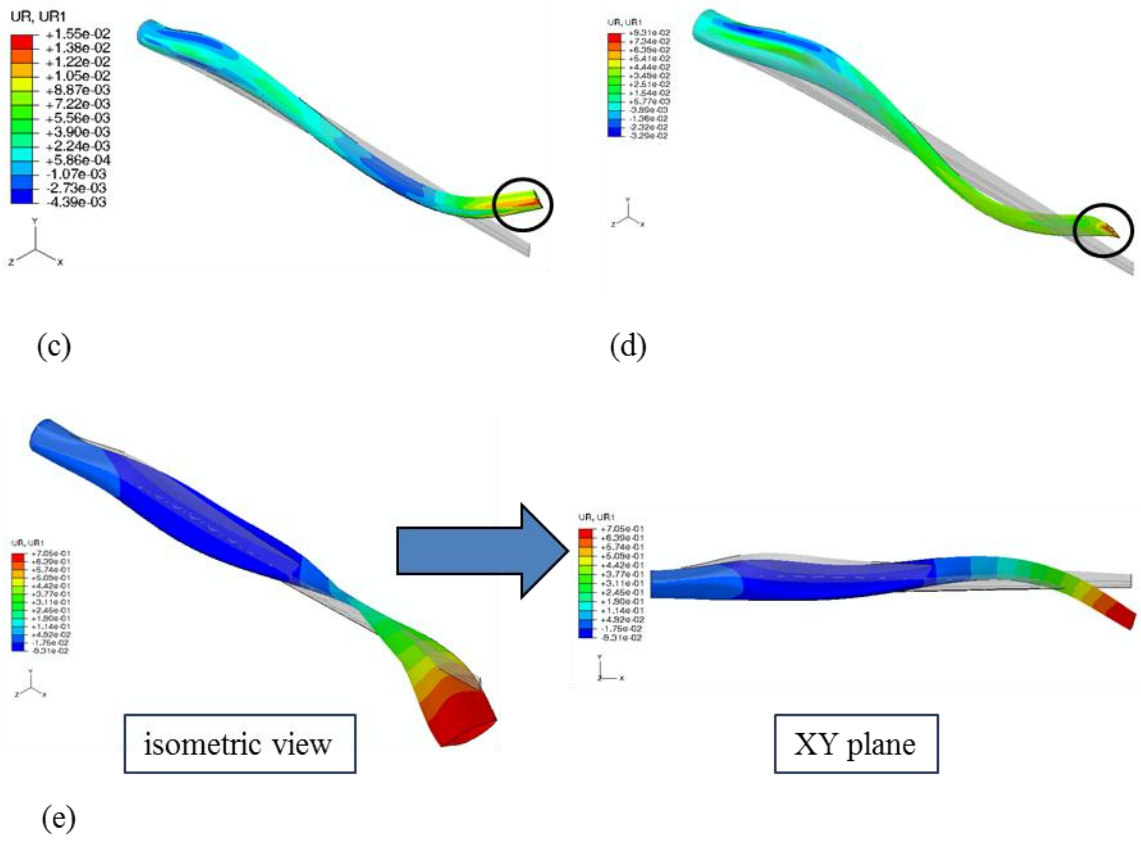

Figure 4.36. Continued.

The stiffness of the blade is based on a hinge equivalent beam theory. This is done because it is useful to analyze the structural dynamics of wind turbines with discrete blade models. The estimated values of stiffness are presented in Table 4.1. Note that the hinge spring stiffness of each mode of five blade models is calculated by Equation (2.12), using the extracted non-rotating natural frequencies and mass moment of inertia obtained from the computational analyses.

Table 4.1. Hinge spring stiffness in Nm.

Mode	SW-91	SW-86	SW-77	SW-63	CT
1st flapping	9.67×10^{8}	9.49×10^{8}	8.47×10^{8}	7.46×10^{8}	8.16×10^{8}
1st edge	3.87×10^{9}	3.82×10^{9}	2.36×10^{9}	1.31×10^{9}	3.51×10^{9}
1st torsional	2.63×10^{8}	2.93×10^{8}	2.48×10^{8}	1.65×10^{8}	1.80×10^{8}

As discussed previously, five blade models are compared from point of view of natural frequencies, SW-63 Model is observed to have the highest flapping natural frequency. However, SW-91 Model has the highest hinge spring stiffness for flapping mode. This apparent discrepancy is because the mass moment of inertia plays an important role in the stiffness given in Equation (2.12). Thus, even though SW-63 Model has a lower stiffness compared to SW-91 Model. The mass of SW-91 Model being much higher enables it to have a lower frequency than SW-63 Model. Although stiffness is usually independent of mass moment of inertia, the hinge spring stiffness is dependent. Thus, the hinge spring stiffness is usually higher as the blade weight increases.

5. CONCLUSIONS AND FUTURE WORK

The preliminary study of the 19.8 kW blade (P20KW-L5.5M Blade) highlighted the principal stress contours in the root, transition, and airfoil sections. The deformed shape and stress results depicted the dependence on the taper and the twist in the blade geometry, as well as the material orthotropy. The natural frequency calculations revealed that it may resonate with the drive train.

In the 80 m full blade models, the largest displacements were desired along the blade Z-axis where the resultant applied forces were the largest. The original cross-section shape of all the models was maintained after deformation, and exhibited very small twist angles (< 2.60°) about the blade X-axis.

Hashin criteria in all the composite layers in all the case studies remained below 1. Thus, the GF and CF layers of the blade root, skin, shear webs, and spar caps were not damaged. The balsa core of sandwich skins exceeds its allowable strength first. The removal of the balsa core from the skin at selected regions such as spar cap delayed damage initiation. In the CT Model, balsa core is damaged: (1) at the upper skin and spar cap regions due to flapping bending moments, and (2) at the tubular-skin attachments region due to stress concentrations. The tubulars carried high axial stresses, as expected. The composite tubular configurations only brought 10% weight reduction.

The natural frequency results identified the lowest natural frequency as the first flapping mode. The first torsional natural frequency was much higher than the first flapping edge mode natural frequencies. Removing balsa core from the skin and spar cap

sections led to an increase in the torsional natural frequency. The reduction in thickness of the balsa core caused a decrease in the edge natural frequency. The CT Model lower torsional natural frequency, and exhibited a strong coupling mode (bending and twisting) in its higher natural frequencies. There was not a significant change in the edge natural frequency of the models.

Laminate hybridization employed in this study is considered to enhance overall weight saving, and offers new alternatives for optimization. The future work should address blade response to impact, and fluctuating lift and drag loads to provide a complete structural assessment.

REFERENCES

1. Energy Information Administration. International Energy Outlook 2009. http://www.eia.doe.gov/oiaf/ieo/pdf/0484%282009%29.pdf. Accessed May 21, 2009.

2. Energy in U.S. Department of Energy, Energy Efficiency and Renewable. Advantages and Disadvantages of Wind Energy. http://www1.eere.energy.gov/windandhydro/wind_ad.html. Accessed May 21, 2009.

3. O'Connell, R., Pletka, R., Block, S., Jacobson, R., Smith, P., *et al.* (2007). *20 Percent Wind Energy Penetration in the United States: A Technical Analysis of the Energy Resource*, Black & Veatch, Overland Park.

4. Burton, T., Sharpe, D., Jenkins, N., and Bossanyi, E. (2001). *Wind Energy Handbook*, John Wiley & Sons, New York.

5. Archer, C. L. and Jacobson, M. Z. (2005). Evaluation of Global Wind Power, *Journal of Geophysical Research*, **110**(12): D12110.

6. U.S. Department of Energy. Energy Efficiency and Renewable. 20% Wind Energy by 2030: Increasing Wind Energy's Contribution to U.S. Electricity Supply. http://www1.eere.energy.gov/windandhydro/pdfs/41869.pdf. Accessed May 21, 2009.

7. Betz, A. (1966). *Introduction to the Theory of Flow Machines*, Pergamon Press, New York.

8. Eggleston, D. M. and Stoddard, F. S. (1987). *Wind Turbine Engineering Design*, Van Nostrand Reinhold Company, New York.

9. Enercon GmbH. WindBlatt Magazine 01/2010. http://www.enercon.de/www/en/windblatt.nsf/562a62338e7e78dcc1256e8900540f58/576d6e7ce6779761c12576c8003b3693/$FILE/WB-0110-en.pdf. Accessed August 5, 2010.

10. Brondsted, P., Lilholt, H., and Lystrup, A. (2005). Composite Materials for Wind Power Turbine Blades, *Annual Review of Materials Research*, **35**: 505-538.

11. Griffin, D. A. (2001). WindPACT Turbine Design Scaling Studies Technical Area 1: Composite Blades for 80- to 120-Meter Rotor, NREL/SR-500-29492, National Renewable Energy Laboratory, Golden, CO.

12. Ashwill, T. D. and Laird, D. L. (2007). Concepts to Facilitate Very Large Blades, In: *the 45th AIAA Aerospace Sciences Meeting and Exhibit*, Reno, Nevada**,** January 8-11.

13. Kyriazoglou, C. and Guild, F. J. (2006). Finite Element Prediction of Damping of Composite GFRP and CFRP Laminates: A Hybrid Formulation -Vibration Damping Experiments and Rayleigh Damping, *Composites Science and Technology*, **66(**3-4): 487-498.

14. American Society for Metals. (1987). *Engineered Materials Handbook; Composite*, Volume 1, ASM International Handbook Committee, Metals Park, OH.

15. Berry, D. S. (2008). Blade System Design Studies Phase II: Final Project Report, SAND2008-4648, Sandia National Laboratories, Albuquerque, NM.

16. Tangler, J. L. and Somers, D. M. (1995). NREL Airfoil Families for HAWTs, In: *AWEA Windpower '95 Conference*, Washington, DC, March 27-30.

17. Somers, D. M. (1997). Design and Experimental Results for the S809 Airfoil, NREL/SR-440-6918, National Renewable Energy Laboratory, Golden, CO.

18. Somers, D. M. (2004). The S816, S817, and S818 Airfoils, NREL/SR-500-36333, National Renewable Energy Laboratory, Golden, CO.

19. Timmer, W. A. and van Rooij, R. (2003). Summary of the Delft University Wind Turbine Dedicated Airfoils, *Journal of Solar Energy Engineering*, **125**(4): 488-496.

20. Fuglsang, P. and Bak, C. (2004). Development of the Riso Wind Turbine Airfoils, *Wind Energy*, **7**(2): 145-162.

21. Bak, C., Fuglsang, P., Sorensen, N. N., Madsen, H. A., Shen, W. Z., and Sorensen, J. N. (1999). Airfoil Characteristics for Wind Turbines, Riso-R-1065(EN), Riso National Laboratory, Roskilde, Denmark.

22. Griffin, D. A. (2000). NREL Advanced Research Turbine (ART) Aerodynamic Design of ART-2B Rotor Blades, NREL/SR-500-28473, National Renewable Energy Laboratory, Golden, CO.

23. Thomsen, O. T. (2009). Sandwich Materials for Wind Turbine Blades: Present and Future, *Journal of Sandwich Structures and Materials,* **11**(1): 7-26.

24. Todoroki. A. and Kawakami, Y. (2008). Optimal Design of Wind Turbine Blade of CF/GF Hybrid Composites, *Transactions of JSCES*, **2008**: 20080012 (in Japanese).

25. Hau, E. (2006). *Wind Turbines: Fundamentals, Technologies, Application, Economics*, **2nd edn**, Springer-Verlag, New York.

26. Jensen, F. M., Falzon, B. G., Ankersen, J., and Stang, H. (2006). Structural Testing and Numerical Simulation of a 34 m Composite Wind Turbine Blade, *Composite Structures*, **76**(1-2): 52-61.

27. De Goeij, W. C., Van Tooren, M. J. L., and Beukers, A. (1999). Implementation of Bending-torsion Coupling in the Design of a Wind-turbine Rotor-blade, *Applied Energy*, **63**(3):191-207.

28. Mohamed, M., H. and Wetzel, K., K. (2006). 3D Woven Carbon/Glass Hybrid Spar Cap for Wind Turbine Rotor Blade, *Journal of Solar Energy Engineering*, **128**(4): 562-573.

29. Hasager, C. B., Pena, A., Mikkelsen, T., Courtney, M., Antoniou, I., Gryning, S. E., Hansen, P., Sorensen, P.B. (2007). 12MW Horns Rev Experiment, Riso-R-1506(EN), Riso National Laboratory, Roskilde, Denmark.

30. Griffin, D. A. (2002). Blade System Design Studies Volume I: Composite Technologies for Large Wind Turbine Blades, SAND2002-1879, Sandia National Laboratories, Albuquerque, NM.

31. Griffin, D. A. (2004). Blade System Design Studies Volume II: Preliminary Blade Designs and Recommended Test Matrix, SAND2004-0073, Sandia National Laboratories, Albuquerque, NM.

32. Giguere, P. and Selig, M. S. (1999). Design of a Tapered and Twisted Blade for the NREL Combined Experiment Rotor, NREL/SR-500-26173, National Renewable Energy Laboratory, Golden, CO.

33. Branner, K., Berring, P., Berggreen, C., and Knudsen, H. W. (2007). Torsional Performance of Wind Turbine Blade-Part II: Numerical Validation, In: *the 16th International Conference on Composite Materials,* Kyoto, Japan, July 8-13.

34. Berring, P., Branner, K., Berggreen, C., and Knudsen, H. W. (2007). Torsional Performance of Wind Turbine Blade-Part I: Experimental Investigation, In: *the 16th International Conference on Composite Materials,* Kyoto, Japan, July 8-13.

35. Laird, D. L., Montoya, F. C., and Malcolm, D. J. (2005). Finite Element Modeling of Wind Turbine Blades, In: *the 43rd AIAA Aerospace Sciences Meeting and Exhibit, R*eno, Nevada, January 10-13.

36. International Electrotechnical Commission (2005). *IEC 61400-1 Wind Turbine Generator Systems-Part 1 Safety Requirements*, International Electrotechnical Commission, Geneva, Switzerland.

37. Jureczko, M., Pawlak,M., and Mezyk, A. (2005). Optimisation of Wind Turbine Blades, *Journal of Materials Processing Technology*, **167**(2-3): 463-471.

38. Locke, J. and Valenica, U. A. (2004). Design Studies for Twist-Coupled Wind Turbine Blades, SAND2004-0522, Sandia National Laboratories, Albuquerque, NM.

39. Mckittrick, L. R., Caims, D. S., Mandell, J., Combs, D. C., Rabern, D. A., and Van Luchene, R. D. (2001). Analysis of a Composite Blade Design for the AOC 15/50 Wind Turbine Using a Finite Element Model, SAND2001-1441, Sandia National Laboratories, Albuquerque, NM.

40. Berggreen, C., Jensen, C., and Hayman, B. (2007). Buckling Strength of Square Composite Plates with Geometrical Imperfections-Preliminary Results, In: *Proceedings of the 1st MARSTRUCT International Conference*, Glasgow, UK, March 12-14, pp. 413-420.

41. Berggreen, C., Tsouvalis, N., Hayman, B., and Branner, K. (2008). Buckling Strength of Thick Composite Panels in Wind Turbine Blades – Part I: Effect of Geometrical Imperfections, In: *the 4th International Conference on Composites Testing and Model Identification*, Dayton, Ohio, October 20-24.

42. Branner, K., Berring, P., and Berggreen, C. (2008). Buckling Strength of Thick Composite Panels in Wind Turbine Blades – Part II: Effect of Delaminations, In: *the 4th International Conference on Composites Testing and Model Identification,* Dayton, Ohio, October 20-24.

43. Chortis, D. I., Chrysochoidis, N. A., and Saravanos, D. A. (2007). Damped Structural Dynamics Models of Large Wind-Turbine Blades including Material and Structural Damping, *Journal of Physics: Conference Series*, **75**(1): 012076.

44. ABAQUS Documentation Collection, **Version 6.8**. (2008). ABAQUS, Inc., Pawtucket, RI.

45. Herakovich, C. T. (1998). *Mechanics of Fibrous Composites*, John Wiley & Sons, New York.

46. Daniel, M. D. and Ishai, O. (1994). *Engineering Mechanics of Composite Materials*, Oxford University Press, New York.

47. MatWeb. Greene Tweed Orthetek WF Polyketone, Continuous Woven Carbon Fiber, Database of Material Properties. http://www.matweb.com/search/QuickText.aspx?SearchText=woven%20carbon. Accessed January 12, 2010.

48. Norton, R. L. (2000). *Machine Design an Integrated Approach,* **2nd edn**, Prentice-Hall, New Jersey.

49. Hashin, Z. and Rotem, A. (1973). A Fatigue Failure Criterion for Fiber Reinforced Materials, *Journal of Composite Materials*, **7**(4): 448-464.

50. Hashin, Z. (1980). Failure Criteria for Unidirectional Fiber Composites, *Journal of Applied Mechanics*, **47**(2): 329-334.

51. Hibbeler, R. C. (1997). *Mechanics of Materials,* **3rd edn**, Prentice-Hall, New Jersey.

52. NREL 10-m Wind Turbine Testing in NASA Ames 80'x120' Wind Tunnel. Turbine Specifications for Model Construction. http://wind.nrel.gov/amestest. Accessed September 11, 2011.

53. Reddy, J. N. (2006). *An Introduction to the Finite Element Method,* **3rd edn**, McGraw-Hill, New York.

54. Bathe, K. J. (1996). *Finite Element Procedures*, Prentice-Hall, New Jersey.

55. Timoshenko, S., Young, D. H., and Weaver, W. (1974). *Vibration Problems in Engineering,* **4th edn**, John Wiley & Sons, New York.

APPENDIX A

The Midlin shell theory forms the relaxation of the Kirchhoff constraints: a transverse normal plane rotates with angles (ϕ_x) about the y-axis as shown in Figure A.1 [53]. The bending strain tensors are given in Equation (A.1), and the governing equations for the Midlin shell theory are expressed in Equations (A.2)-(A.4).

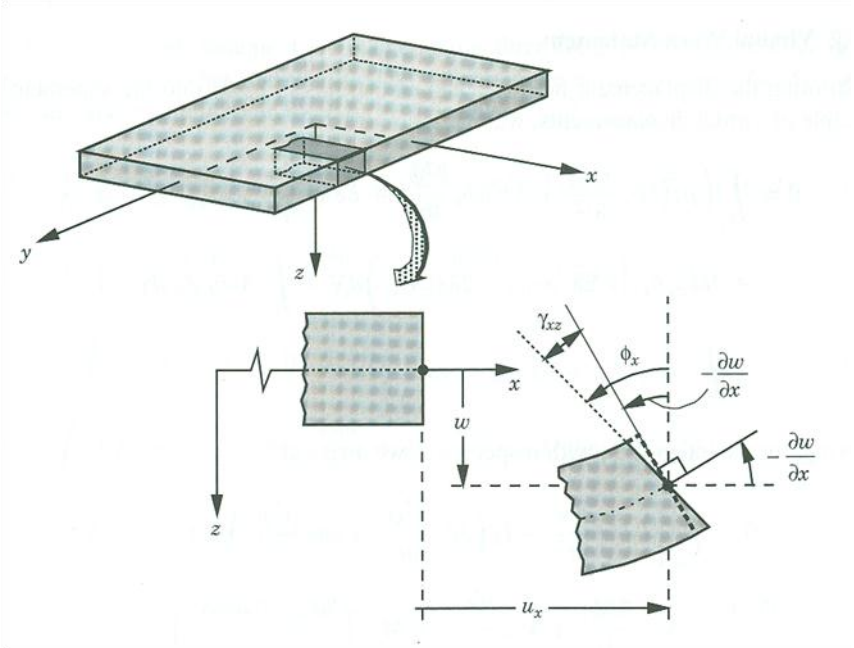

Figure A.1. Kinematics of Mindlin shell theory [53].

$$\begin{Bmatrix} \varepsilon_{xx} \\ \varepsilon_{yy} \\ 2\gamma_{xy} \\ 2\gamma_{xz} \\ 2\gamma_{yz} \end{Bmatrix} = \begin{Bmatrix} z\dfrac{\partial \phi_x}{\partial x} \\ z\dfrac{\partial \phi_y}{\partial y} \\ z\left(\dfrac{\partial \phi_x}{\partial y} + \dfrac{\partial \phi_y}{\partial x}\right) \\ \phi_x + \dfrac{\partial w}{\partial x} \\ \phi_y + \dfrac{\partial w}{\partial y} \end{Bmatrix} \tag{A.1}$$

where w is the displacement on the mid-plane in the z-axis, ϕ_x and ϕ_y the rotation of the transverse normal plane about the y-axis and the x-axis, respectively.

$$\frac{\partial Q_x}{\partial x} + \frac{\partial Q_y}{\partial y} + q = I_0 \frac{\partial^2 w}{\partial t^2} \tag{A.2}$$

$$\frac{\partial M_{xx}}{\partial x} + \frac{\partial M_{xy}}{\partial y} - Q_x = I_2 \frac{\partial^2 \phi_x}{\partial t^2} \tag{A.3}$$

$$\frac{\partial M_{xy}}{\partial x} + \frac{\partial M_{yy}}{\partial y} - Q_y = I_2 \frac{\partial^2 \phi_y}{\partial t^2} \tag{A.4}$$

Similarly, the normality assumption may be relaxed in the Timoshenko beam theory, and the kinematics of this theory are presented in Figure A.2 [53]. While the equilibrium equations of the Euler-Bernoulli beam are basically maintained in the Timoshenko beam theory, a beam involving shear deformations has to be kinematically

constrained. The governing equations for Timoshenko beams are given in Equation (A.5) and (A.6), which are coupled, partial differential equations for two variables, the out-of-plane deflection (w) and rotation about the y-axis (Ψ).

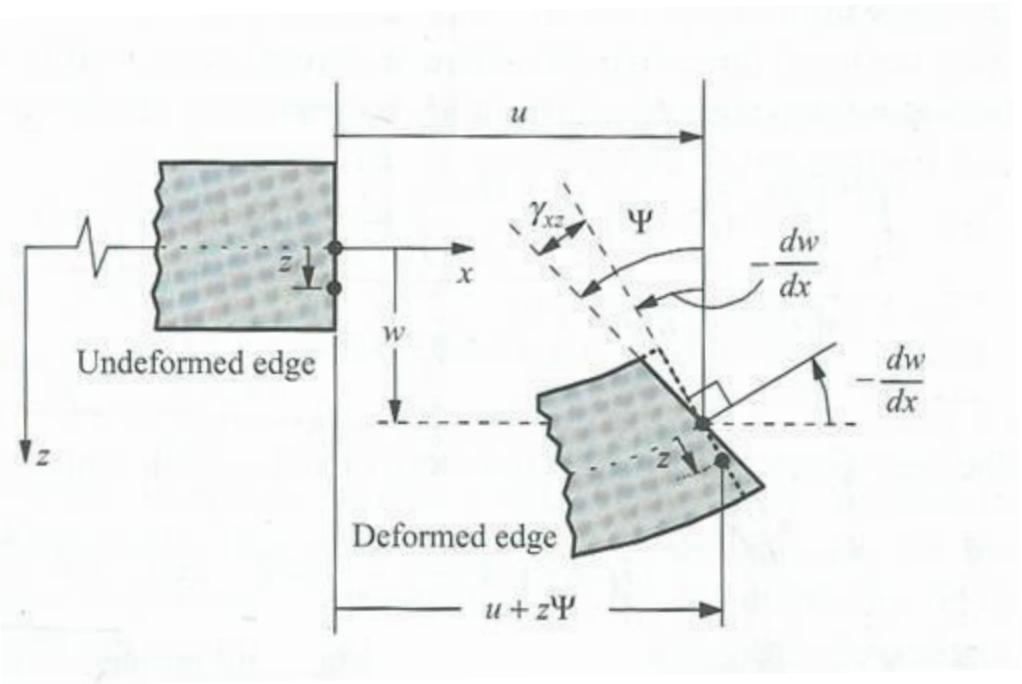

Figure A.2. Kinematics of Timoshenko beams [53].

$$-\frac{d}{dx}\left[GAK_{sc}\left(\Psi+\frac{dw}{dx}\right)\right]+c_f(x)w=q(x) \tag{A.5}$$

and

$$-\frac{d}{dx}\left(E(x)I(x)\frac{d\Psi}{dx}\right)+GAK_{sc}\left(\Psi+\frac{dw}{dx}\right)=0 \tag{A.6}$$

where G denotes shear modulus; $E(x)$, Young's modulus; $I(x)$, 2nd moment of inertia; A, the cross-sectional area; $q(x)$, the distributed transverse load; c_f (x), the elastic foundation modulus; K_{sc}, the shear correction coefficient.

APPENDIX B

The effective properties of fibrous composite materials are obtained based on the 3D constitutive equations and classical laminated plate theory [45]. Fibrous composite materials are usually categorized as orthotropic materials, for which Hooke's law can be expressed in Equation (B.1) referring to the material coordinates, where 1 is the fiber direction, 2 is transverse to the fiber, and 3 is normal to the fiber. [Q] in Equation (B.1) is the stiffness matrix and can be determined by the elastic constants. The inverted form of Hooke's law can be written in Equation (B.2) in terms of the elastic constants.

$$\{\sigma\}_1 = [Q]\{\varepsilon\}_1 \tag{B.1a}$$

or

$$\begin{Bmatrix} \sigma_1 \\ \sigma_2 \\ \sigma_3 \\ \tau_{23} \\ \tau_{13} \\ \tau_{12} \end{Bmatrix} = \begin{bmatrix} Q_{11} & Q_{12} & Q_{13} & 0 & 0 & 0 \\ Q_{12} & Q_{22} & Q_{23} & 0 & 0 & 0 \\ Q_{13} & Q_{23} & Q_{33} & 0 & 0 & 0 \\ 0 & 0 & 0 & Q_{44} & 0 & 0 \\ 0 & 0 & 0 & 0 & Q_{55} & 0 \\ 0 & 0 & 0 & 0 & 0 & Q_{66} \end{bmatrix} \begin{Bmatrix} \varepsilon_1 \\ \varepsilon_2 \\ \varepsilon_3 \\ \gamma_{23} \\ \gamma_{13} \\ \gamma_{12} \end{Bmatrix} \tag{B.1b}$$

$$\{\varepsilon\}_1 = [C]\{\sigma\}_1 \tag{B.2a}$$

or

$$\begin{Bmatrix} \varepsilon_1 \\ \varepsilon_2 \\ \varepsilon_3 \\ \gamma_{23} \\ \gamma_{13} \\ \gamma_{12} \end{Bmatrix} = \begin{bmatrix} \frac{1}{E_1} & \frac{-\nu_{12}}{E_1} & \frac{-\nu_{13}}{E_1} & 0 & 0 & 0 \\ \frac{-\nu_{12}}{E_1} & \frac{1}{E_2} & \frac{-\nu_{23}}{E_2} & 0 & 0 & 0 \\ \frac{-\nu_{13}}{E_1} & \frac{-\nu_{23}}{E_2} & \frac{1}{E_3} & 0 & 0 & 0 \\ 0 & 0 & 0 & \frac{1}{G_{23}} & 0 & 0 \\ 0 & 0 & 0 & 0 & \frac{1}{G_{13}} & 0 \\ 0 & 0 & 0 & 0 & 0 & \frac{1}{G_{12}} \end{bmatrix} \begin{Bmatrix} \sigma_1 \\ \sigma_2 \\ \sigma_3 \\ \tau_{23} \\ \tau_{13} \\ \tau_{12} \end{Bmatrix} \tag{B.2b}$$

Using tensor transformation law gives a relationship between the material coordinate system and the global xyz coordinate system of laminas as expressed in Equation (B.3). Similarly, the transformed strain tensors are given in Equation (B.4).

$$\{\sigma\}_1 = [T_1]\{\sigma\}_x \tag{B.3a}$$

or

$$\begin{Bmatrix} \sigma_1 \\ \sigma_2 \\ \sigma_3 \\ \tau_{23} \\ \tau_{13} \\ \tau_{12} \end{Bmatrix} = \begin{bmatrix} m^2 & n^2 & 0 & 0 & 0 & 2mn \\ n^2 & m^2 & 0 & 0 & 0 & -2mn \\ 0 & 0 & 1 & 0 & 0 & 0 \\ 0 & 0 & 0 & m & -n & 0 \\ 0 & 0 & 0 & n & m & 0 \\ -mn & mn & 0 & 0 & 0 & m^2 - n^2 \end{bmatrix} \begin{Bmatrix} \sigma_x \\ \sigma_y \\ \sigma_z \\ \tau_{yz} \\ \tau_{xz} \\ \tau_{xy} \end{Bmatrix} \tag{B.3b}$$

where $m = \cos\theta$ and $n = \sin\theta$.

$$\{\varepsilon\}_1 = [T_2]\{\varepsilon\}_x \tag{B.4a}$$

or

$$\begin{Bmatrix} \varepsilon_1 \\ \varepsilon_2 \\ \varepsilon_3 \\ \gamma_{23} \\ \gamma_{13} \\ \gamma_{12} \end{Bmatrix} = \begin{bmatrix} m^2 & n^2 & 0 & 0 & 0 & mn \\ n^2 & m^2 & 0 & 0 & 0 & -mn \\ 0 & 0 & 1 & 0 & 0 & 0 \\ 0 & 0 & 0 & m & -n & 0 \\ 0 & 0 & 0 & n & m & 0 \\ -2mn & 2mn & 0 & 0 & 0 & m^2 - n^2 \end{bmatrix} \begin{Bmatrix} \varepsilon_x \\ \varepsilon_y \\ \varepsilon_z \\ \gamma_{yz} \\ \gamma_{xz} \\ \gamma_{xy} \end{Bmatrix} \tag{B.4b}$$

Substituting Equations (B.3) and (B.4) to Equation (B.1) and premultiplying it by $[T_1]^{-1}$ result in Equation (B.5). The transformed stiffness matrix is defined in Equation (B.6).

$$\{\sigma\}_x = [T_1]^{-1}[Q][T_2]\{\varepsilon\}_x \tag{B.5}$$

$$[\overline{Q}] = [T_1]^{-1}[Q][T_2] \tag{B.6}$$

Upon classical laminated plate theory (CLPT), in-plane components of 3D constitutive equations are employed, and these components at the *k*th layer of a laminate are given in Equation (B.7). The in-plane strain vector is composed of the nominal strains on the reference surface and laminate curvatures throughout the thickness as shown in Equation (B.8). The relationship for stress and strain in the *k*th layer is presented in Equation (B.9).

$$\begin{Bmatrix} \sigma_x \\ \sigma_y \\ \sigma_{xy} \end{Bmatrix}_k = \begin{bmatrix} \bar{Q}_{11} & \bar{Q}_{12} & \bar{Q}_{16} \\ \bar{Q}_{12} & \bar{Q}_{22} & \bar{Q}_{26} \\ \bar{Q}_{16} & \bar{Q}_{26} & \bar{Q}_{66} \end{bmatrix}_k \begin{Bmatrix} \varepsilon_x \\ \varepsilon_y \\ \gamma_{xy} \end{Bmatrix}_k \tag{B.7}$$

$$\begin{Bmatrix} \varepsilon_x \\ \varepsilon_y \\ \gamma_{xy} \end{Bmatrix} = \begin{Bmatrix} \varepsilon_x^o \\ \varepsilon_y^o \\ \gamma_{xy}^o \end{Bmatrix} + z \begin{Bmatrix} \kappa_x \\ \kappa_y \\ \kappa_{xy} \end{Bmatrix} \tag{B.8}$$

$$\begin{Bmatrix} \sigma_x \\ \sigma_y \\ \sigma_{xy} \end{Bmatrix}_k = \begin{bmatrix} \bar{Q}_{11} & \bar{Q}_{12} & \bar{Q}_{16} \\ \bar{Q}_{12} & \bar{Q}_{22} & \bar{Q}_{26} \\ \bar{Q}_{16} & \bar{Q}_{26} & \bar{Q}_{66} \end{bmatrix}_k \begin{Bmatrix} \varepsilon_x^o \\ \varepsilon_y^o \\ \gamma_{xy}^o \end{Bmatrix}_k + z \begin{bmatrix} \bar{Q}_{11} & \bar{Q}_{12} & \bar{Q}_{16} \\ \bar{Q}_{12} & \bar{Q}_{22} & \bar{Q}_{26} \\ \bar{Q}_{16} & \bar{Q}_{26} & \bar{Q}_{66} \end{bmatrix}_k \begin{Bmatrix} \kappa_x \\ \kappa_y \\ \kappa_{xy} \end{Bmatrix}_k \tag{B.9}$$

The laminate constitutive equations are obtained by summation of forces and moments per unit length as presented in Equation (B.10). In ABD matrix, [*A*] describe the in-plane stiffness, [*B*] represents the bending-stretching coupling, and [*D*] is the

bending stiffness. [*A*], [*B*], and [*D*] matrixes are defined by Equations (B.11) - (B.13), respectively.

$$\begin{Bmatrix} N_x \\ N_y \\ N_{xy} \\ M_x \\ M_y \\ M_{xy} \end{Bmatrix} = \begin{bmatrix} A_{11} & A_{12} & A_{16} & B_{11} & B_{12} & B_{16} \\ A_{12} & A_{22} & A_{26} & B_{12} & B_{22} & B_{26} \\ A_{16} & A_{26} & A_{66} & B_{16} & B_{26} & B_{66} \\ B_{11} & B_{12} & B_{16} & D_{11} & D_{12} & D_{16} \\ B_{12} & B_{22} & B_{26} & D_{12} & D_{22} & D_{26} \\ B_{16} & B_{26} & B_{66} & D_{16} & D_{26} & D_{66} \end{bmatrix} \begin{Bmatrix} \varepsilon_x^o \\ \varepsilon_y^o \\ \gamma_{xy}^o \\ \kappa_x \\ \kappa_y \\ \kappa_{xy} \end{Bmatrix} \tag{B.10}$$

$$[A] = \sum_{k=1}^{N} \left[\bar{Q}\right]^k \left(z_k - z_{k-1}\right) \tag{B.11}$$

$$[B] = \frac{1}{2} \sum_{k=1}^{N} \left[\bar{Q}\right]^k \left(z_k^2 - z_{k-1}^2\right) \tag{B.12}$$

$$[D] = \frac{1}{3} \sum_{k=1}^{N} \left[\bar{Q}\right]^k \left(z_k^3 - z_{k-1}^3\right) \tag{B.13}$$

In order to obtain formulas for engineering constants, laminates with symmetric and uncoupled response from bending are employed. The laminate average stresses are defined by Equation (B.14). Equation (B.14) is rewritten in Equation (B.15) to obtain a compliance matrix. For convenience of notations, the laminate compliance is denoted as in Equation (B.16). Therefore, engineering constants for the laminates are summarized

in Equations (B.17) – (B.21). Since the Cartesian and cylindrical coordinate systems are orthonormal, the 3D constitutive equation and CLPT can applied for cylindrical problems.

$$\{\bar{\sigma}\} \equiv \frac{1}{2H}\{N\} = \frac{1}{2H}[A]\{\varepsilon^o\} \tag{B.14}$$

$$\{\varepsilon^o\} = 2H[A]^{-1}\{\bar{\sigma}\} = [a^*]\{\bar{\sigma}\} \tag{B.15}$$

$$[a^*] \equiv 2H[A]^{-1} = \begin{bmatrix} a_{11}^* & a_{12}^* & a_{16}^* \\ a_{12}^* & a_{22}^* & a_{26}^* \\ a_{16}^* & a_{26}^* & a_{66}^* \end{bmatrix} \tag{B.16}$$

For axial stretching, axial modulus:

$$E_x = \frac{1}{a_{11}^*} \tag{B.17}$$

Poisson ratio:

$$\nu_{xy} = -\frac{a_{12}^*}{a_{11}^*} \tag{B.18}$$

For transversely stretching, transverse modulus:

$$E_y = \frac{1}{a_{22}^*} \tag{B.19}$$

Poisson ratio:

$$\nu_{yx} = -\frac{a_{12}^*}{a_{22}^*} \tag{B.20}$$

For shear deformations, shear modulus:

$$G_{xy} = \frac{1}{a_{66}^*} \tag{B.21}$$

APPENDIX C

For in-plane stress problems, the Hashin damage initiation criteria of four different damage initiation mechanisms are represented as follows [44,49,50]:

If $\hat{\sigma}_{11} \geq 0$, fiber tension mode:

$$\left(\frac{\hat{\sigma}_{11}}{X_T}\right)^2 + \alpha_c \left(\frac{\hat{\tau}_{12}}{S_L}\right)^2 \geq 1 \tag{C.1}$$

If $\hat{\sigma}_{11} < 0$, fiber compression mode:

$$\left(\frac{\hat{\sigma}_{11}}{X_C}\right)^2 \geq 1 \tag{C.2}$$

If $\hat{\sigma}_{22} \geq 0$, matrix tension mode:

$$\left(\frac{\hat{\sigma}_{22}}{Y_T}\right)^2 + \left(\frac{\hat{\tau}_{12}}{S_L}\right)^2 \geq 1 \tag{C.3}$$

If $\hat{\sigma}_{22} < 0$, matrix compression mode:

$$\left(\frac{\hat{\sigma}_{22}}{2S_T}\right)^2 + \left[\left(\frac{Y_C}{2S_T}\right)^2 - 1\right]\frac{\hat{\sigma}_{22}}{Y_C} + \left(\frac{\hat{\tau}_{12}}{S_L}\right)^2 \geq 1 \tag{C.4}$$

In the above equations, X_T denotes the longitudinal tensile strength, X_C the longitudinal compressive strength, Y_T the transverse tensile strength, Y_C the transverse compressive strength, S_L the longitudinal shear strength, S_T the transverse shear strength, and α_c a coefficient to determine the contribution of the shear stress to the fiber tensile mode. Using the proposed model by setting $\alpha_c = 0$ and $S_T = Y_C/2$ or the model with $\alpha_c = 1$, the fiber tensile mode can be specified [49,50].

APPENDIX D

An undamped system equation is expressed in Equation (D.1). It is assumed that the stiffness matrix is symmetric and positive-semidefinite. In this case, the generalized eigenvalue problem for this system of a finite element model is expressed in Equation (D.2).

$$[M]\{\ddot{u}\}+[K]\{u\}=\{0\} \tag{D.1}$$

where [M] the symmetric positive-definite mass matrix, [K] the stiffness matrix, and [u] the displacement vector.

$$\left(-\omega^2[M]+[K]\right)\{\phi\}=\{0\} \tag{D.2}$$

where ω is the eigenvalue and $\{\phi\}$ the eigenvector.

Lanczos method transforms the generalized eigenvalue problem into a standard form with a tridiagonal coefficient matrix as in Equations (D.3) - (D.9). Frequency shift (θ_L) is introduced to the generalized eigenvalue problem for extraction of natural frequencies in interesting ranges.

$$\omega^2=\frac{1}{\theta_L}+S_L \tag{D.3}$$

where S_L is the eigenvalue.

Substituting Equation (D.3) into Equation (D.2) and simplifying it give

$$[M]\left([K]-S_L[M]\right)^{-1}[M]\{\phi\}=\theta_L[M]\{\phi\} \tag{D.4}$$

The eigenvector is transformed by using $[U]$ which is defined as the orthonormal matrix of $[M]$. Due to the orthonormality, we have Equation (D.6). Note that $[I]$ is the identity matrix.

$$\{\phi\}=[U]\{\tilde{\phi}\} \tag{D.5}$$

$$[U]^T[M][U]=[I] \tag{D.6}$$

Substituting Equation (D.5) to Equation (D.4) and premultiplying it by $[U]^T$ lead to

$$[U]^T[M]\left([K]-S_L[M]\right)[M][U]\{\tilde{\phi}\}=\theta_L[U]^T[M][U]\{\tilde{\phi}\} \tag{D.7}$$

Using Equation (D.6), Equation (D.7) can be rewritten as

$$[T]\{\tilde{\phi}\} = \theta_L \{\tilde{\phi}\} \tag{D.8}$$

where

$$[T] = [U]^T [M]([K] - S_L [M])[M][U] \tag{D.9}$$

It is well known that [T] become a tridiagonal matrix since [U] satisfies the orthonormality of the mass matrix. The eigenvalues of Equation (D.8) are the reciprocals of the eigenvalues of Equation (D.2). Equation (D.5) shows the interdependence in Equation (D.2) and (D.8). Therefore, solutions of the standard eigenvalue problem provide the eigenvalues and eigenvectors of the undamped system, and Equation (D.9) can be solved by the Houeholder and Q-R algorithms [44,54].

APPENDIX E

E.1 Partial Blade Model Descriptions

To study two types of internal reinforcement constructions in the blade, a partial section of the 80 m blade is selected as shown in Figure E.1 since the geometric transition zone is subjected to high stresses.

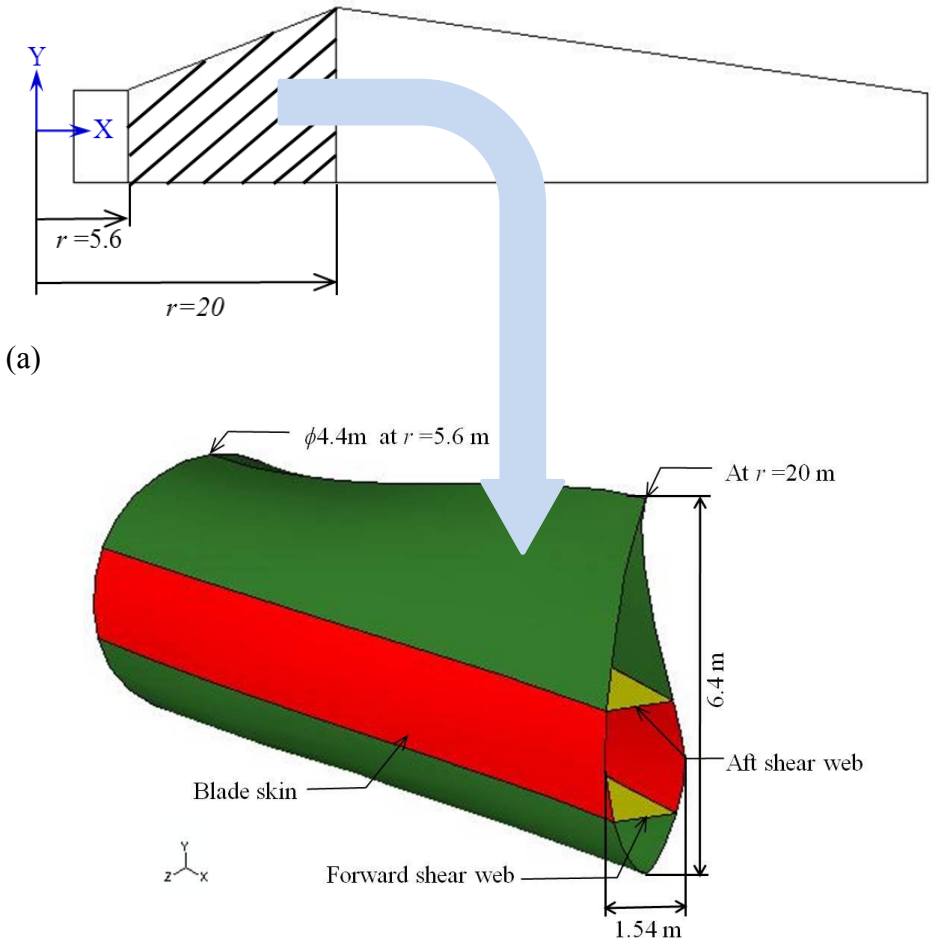

Figure E.1. A partial section of an 80 m blade: (a) Location of the partial blade in a full blade, and (b) a partial blade between r =5.6 m and r =20 m.

The partial blade section is located between r = 5.6 m and r = 20 m of the 80m blade (Figure. E.1). The cross-section at r = 5.6 m is a circle with a diameter of 4.4 m. The cross-section at r = 20 m is the S818 airfoil with a chord length of 6.4 m and blade thickness of 1.54 m. For understanding shear web and tubular truss reinforcements, there are no spar caps in Figure E.1(b). Sandwich constructions consisting of balsa cores and GF fabric are utilized for the blade skin. The ratio of balsa core to GF is 10:1 [24]. The skin has a uniform thickness of 10 cm (Table E.1).

Table E.1 Lay-up for the skin.

Ply	**Material**	**Orientation (º)**	**Ply Thickness (cm)**
1	GF fabric	0	0.4545
2	Balsa	0	9.091
3	GF fabric	0	0.4545

E.1.1 Model-I: Shear Web

Model-I as shown in Figure E.2 consists of sub-sectional skin and shear webs. These components are shown as yellow (shear web) and red (blade skin) surfaces in Figure E.1(b). Sandwich construction with a laminate thickness of 10 cm is utilized for the webs. A lay-up for the webs is presented in Table E.2.

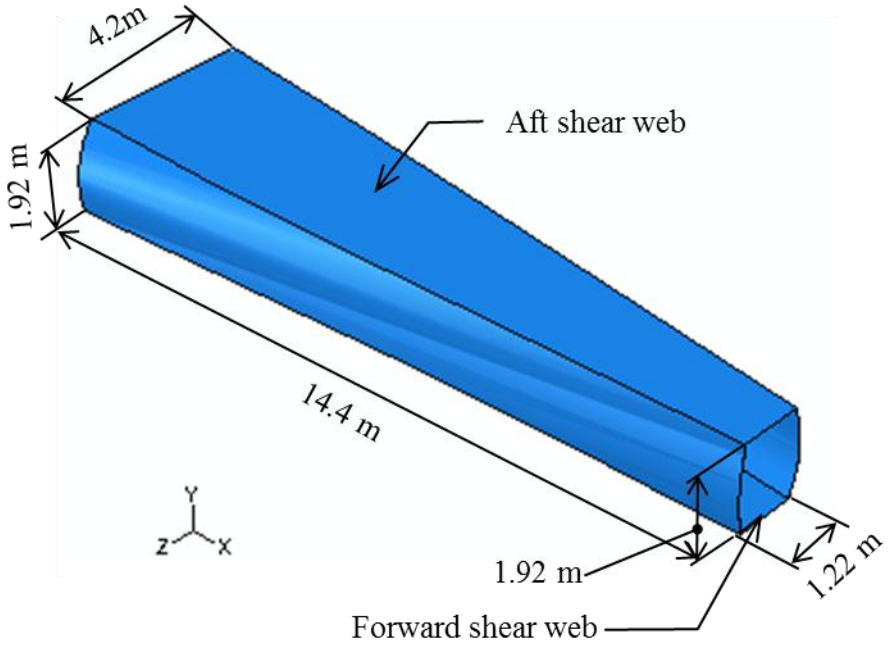

Figure E.2. Model-I; Sub-sectional skin with shear webs.

Table E.2. Lay-up for shear webs.

Ply	Material	Orientation (°)	Ply thickness (cm)
1	GF fabric	0	0.2273
2	UD-GF	45	0.1136
3	UD-GF	-45	0.1136
4	Balsa	0	9.091
5	UD-GF	-45	0.1136
6	UD-GF	45	0.1136
7	GF fabric	0	0.2273

In static and vibration analyses, the three rotations and displacements are constrained at edges of the cross-section as shown in Figure E.3. In the static analyses, dP_Y are applied to both the upper and lower blade skin, and dP_Z is applied to the lower

blade skin (Figure E.3). The maximum values of dP_Y and dP_Z in Table 3.5 are simply taken as magnitudes of the applied loads to this model. Thus, this model is subjected to the following loading conditions: surface pressure of 10.8 kPa in the Z-axis and surface pressure of 0.432 kPa in the Y-axis.

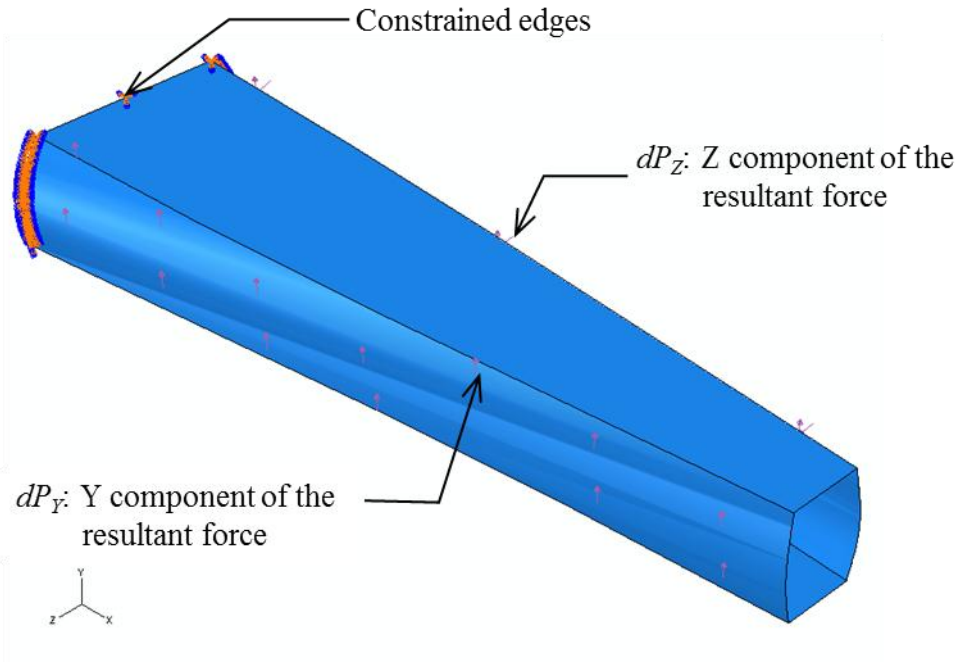

Figure E.3. Constraint conditions for Model-I.

E.1.2 Model-II: Composite Tubular

In order to save weight, tubular truss configurations are adopted and modeled in lieu of shear webs as presented in Figure E.4. The tubulars are arbitrarily attached to the

surface of the skin at intervals of approximately 2 m. The tubulars are treated as Timoshenko beams and are modeled with linear beam elements (B31H).

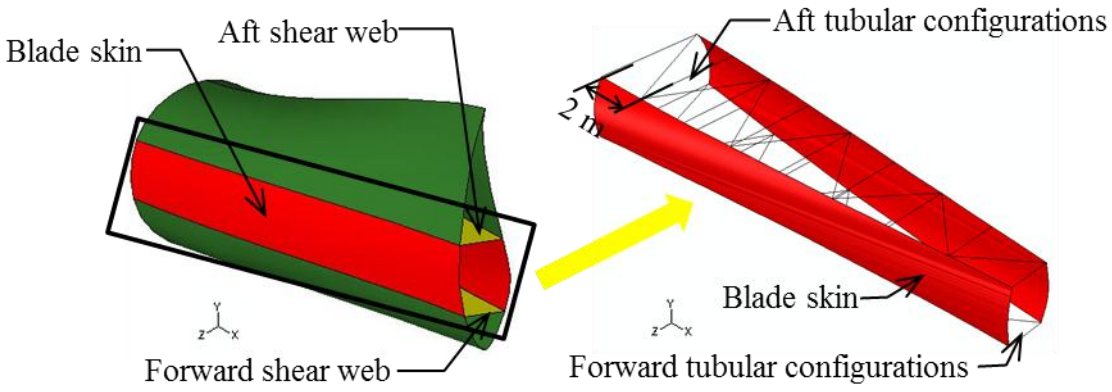

Figure E.4. Composite tubular model.

The candidate geometries for the tubulars with circular cross-section (Figure E.4) are given in Table E.3. Dimensions of Tube-A and Tube-B in Table E.3 are selected to have the same cross-sectional area. GF are employed for composite tubulars with a lay-up of [0/90/30/-30] since tubulars are mainly subjected to high axial stresses arising from the loading conditions. The equivalent laminate properties are shown in Table E.4. Recall that the laminate for the blade skin is the same as Model-I. The sub-sectional skin with Tube-A and Tube-B are named as Model-IIA and Model-IIB, respectively. The boundary and constraint conditions are held the same as Model-I.

Table E.3. Candidate geometries for tubulars.

Geometry type	Cross-section	Diameter (cm)	Wall thickness (cm)
Tube-A	Hollow	10	1
Tube-B	Solid	6	3

Table E.4. Equivalent elastic laminate properties for tubulars.

	Values
ρ_m (kg/m^3)	2,100
E_1 (GPa)	21.8
E_2 (GPa)	15.4
E_3 (GPa)	9.32
G_{12} (GPa)	5.59
G_{13} (GPa)	3.53
G_{23} (GPa)	3.34
v_{12}	0.335
v_{13}	0.270
v_{23}	0.318

E.2 Assessment of Web Replacement study: Partial Blade Model

The sub-section model (14.4 m in axial length) is extracted from the 80m blade, as described in Section E.1, and subjected to the following loading conditions: surface pressure of 10.8 kPa in the Z-axis, and surface pressure of 0.432 kPa in the Y-axis. Model-I consists of the partial skin and shear web as shown in Figure E.2, and the web is replaced with composite tubulars in Model-II, as shown in Figure E.4. In these sandwich constructions, balsa wood is selected for the core and GF fabric is utilized for the face sheets of the skin and the web, as presented in Tables E.1 and E.2. In Model-II, two different glass fiber reinforced composite tubulars (Tube-A and Tube-B) with a stacking sequence of [0/90/30/-30] are employed as shown in Tables E.3 and E.4. Both tubes

have the same cross-sectional area. The skin models with Tube-A and Tube-B are called Model-IIA and Model-IIB, respectively.

E.2.1 Static Analyses of Model-I

The displacements presented in Table E.5 are taken from the nodes specified in Figure E.5, and correspond to the load ratio (L_d/L_a) of 0.6 since the load is applied incrementally. The load ratio describes the ratio of the load at the given step to the assigned load values.

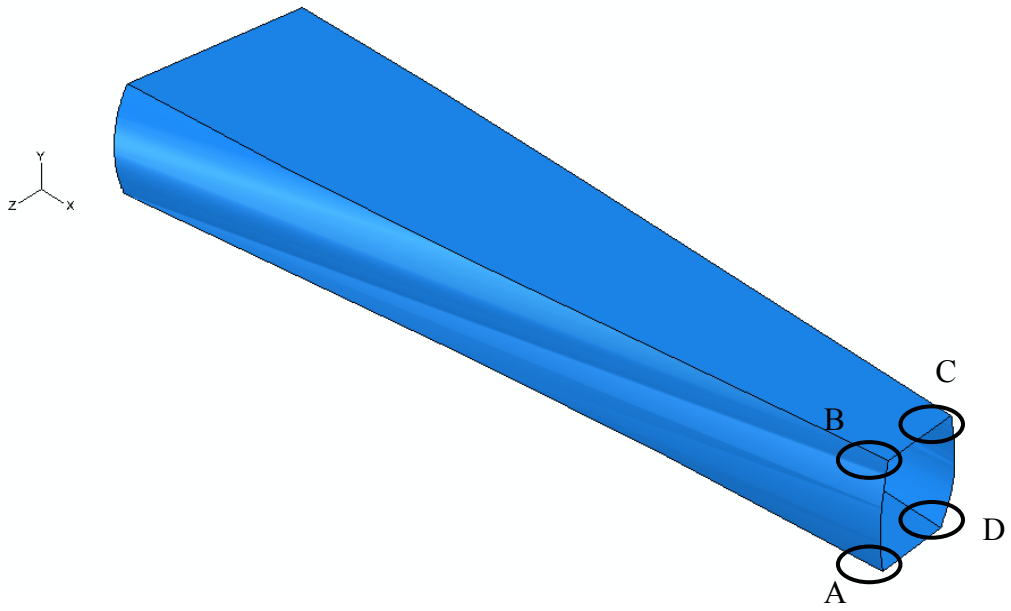

Figure E.5. Selected nodes for displacement presentation.

Table E.5. The displacements of free edge in Model-I at points ABCD.

Node point	Displacement (m/10^{-3})		
	UX	**UY**	**UZ**
A	-0.285	1.66	8.56
B	-0.563	1.76	8.36
C	0.259	1.95	8.36
D	0.537	1.61	8.56

Since the magnitude of dP_Z is twenty-five times as much as that of dP_Y, Model-I experiences the largest displacement along the Z-axis. However, the displacements are small, and fall within liner deformation; the largest UZ displacement corresponds to 0.7% of the axial dimension (14.4 m). Curvature over the partial skin and the applied loads along the Y- and Z-axis produce unequal displacements in the Y direction at the corner nodes.

The stresses generated in GF layer are much lower than its allowable material strength throughout this subsection. The von Mises stress contour in the balsa core of the skin and shear web is presented in Figure E.6. The highest stress seen is 1.06 MPa appears at the corner near the constrained end. The maximum von Mises stress in the balsa core of the skin is observed to be 1.6 MPa at by 100% magnitude of the applied load. The allowable material strength for balsa is 5.4 MPa. Thus, the core does not fail at the maximum applied loads.

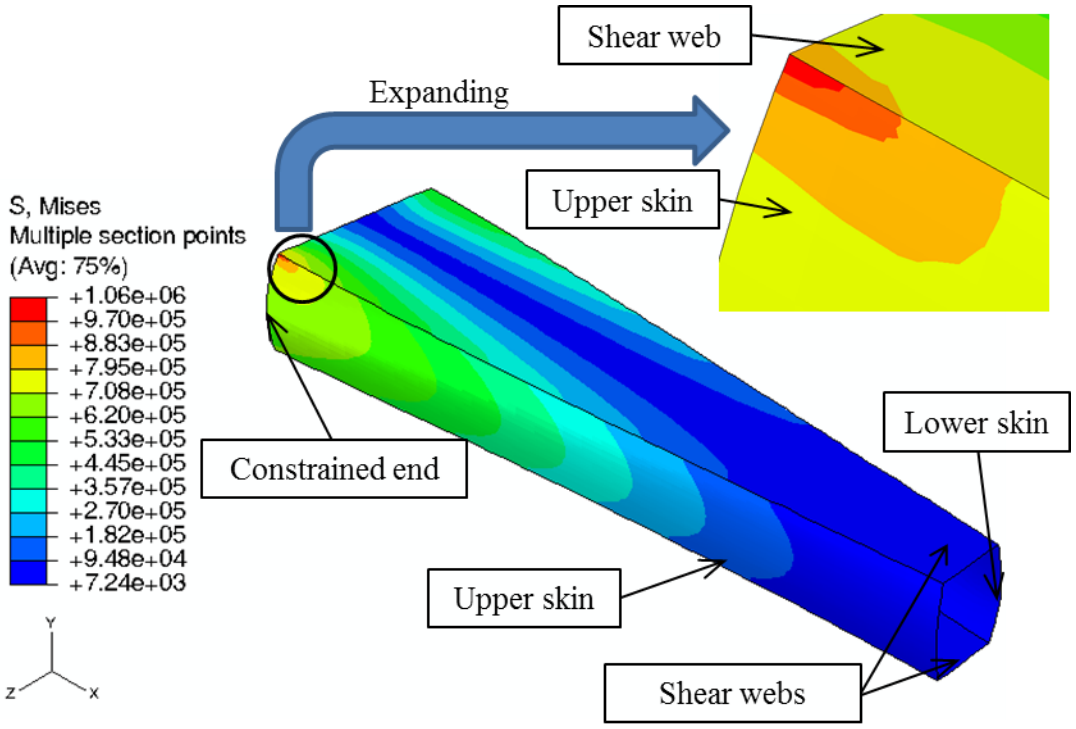

Figure E.6. Von Mises stress contour in the balsa core ($L_d/L_a = 0.6$).

E.2.2 Natural frequency response of Model-I

The first mode natural frequencies of Model-I are presented in Figure E.7, and the corresponding mode shapes are shown in Figure E.8, where the normalization of the largest displacement or rotation is employed. At any given cross-section, the area moment of inertia about the Y-axis is greater than that about the Z-axis. Thus, Model-I is stiffer about the Y-axis and exhibits higher frequency amplitude for the flapping mode.

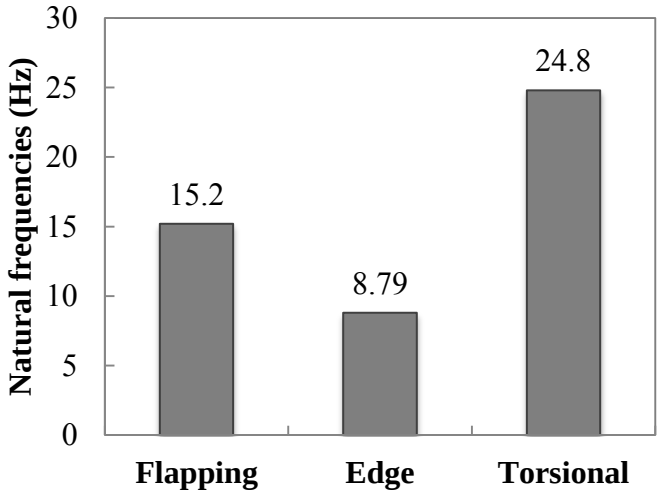

Table E.7. First mode natural frequencies of Model-I.

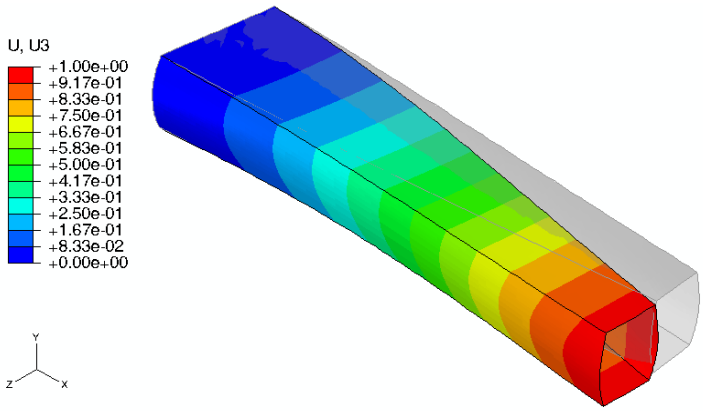

(a)

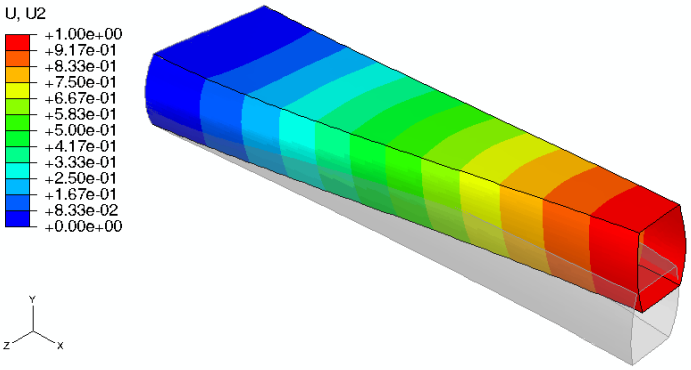

(b)

Figure E.8. First mode shapes of Model-I: (a) flapping, (b) edge, and (c) torsional.

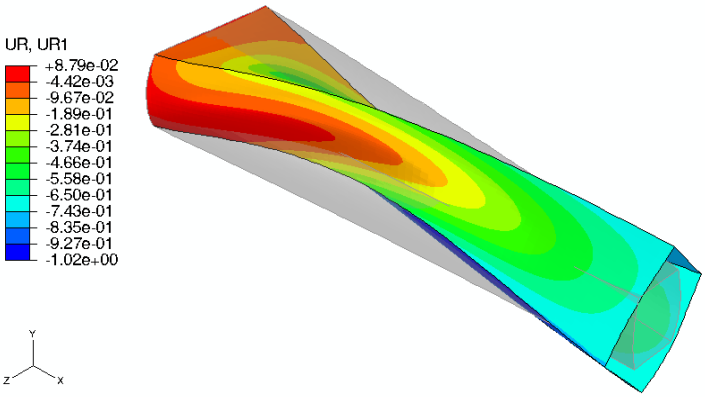

(c)

Figure E.8. Continued.

E.2.3 Static Analyses of Model-II

The corner nodes in Figure E.5 are defined to report displacements at the free edge. The displacements for Model-IIA and Model-IIB are shown in Tables E.6 and E.7, respectively.

Table E.6. Displacements in Model-IIA ($L_d/L_a = 0.6$).

Node point	**Displacement ($m/10^{-3}$)**		
	UX	**UY**	**UZ**
A	0.874	8.75	20.4
B	-0.561	8.89	20.0
C	-1.10	8.47	20.0
D	0.506	7.29	20.4

Table E.7. Displacements in Model-IIB ($L_d/L_a = 0.55$).

Node point	Displacement ($m/10^{-3}$)		
	UX	**UY**	**UZ**
A	0.813	8.67	18.4
B	-0.506	8.74	18.8
C	-1.03	7.18	18.8
D	0.440	5.96	18.5

The displacements for these models are greater than those for Model-I. For example, the UZ displacement of Model-IIA and Model-IIB are 2.4 and 2.2 times UZ displacement of Model-I, respectively. Specifically, Model-IIA and Model-IIB deformed easier along the Y- and Z-axes, indicating that the tubulars were not as stiff. Model-IIA employs tubulars with a hollow cross-section, while Model-IIB employs solid cross-section tubulars; both sets of tubes have the same cross-sectional area. There is 10% difference in the UZ displacements between two models: however, the different geometries of tubes do not play an important role in preventing these deformations. In general, the ratio between the tubes' deformations to their length is less than 0.01.

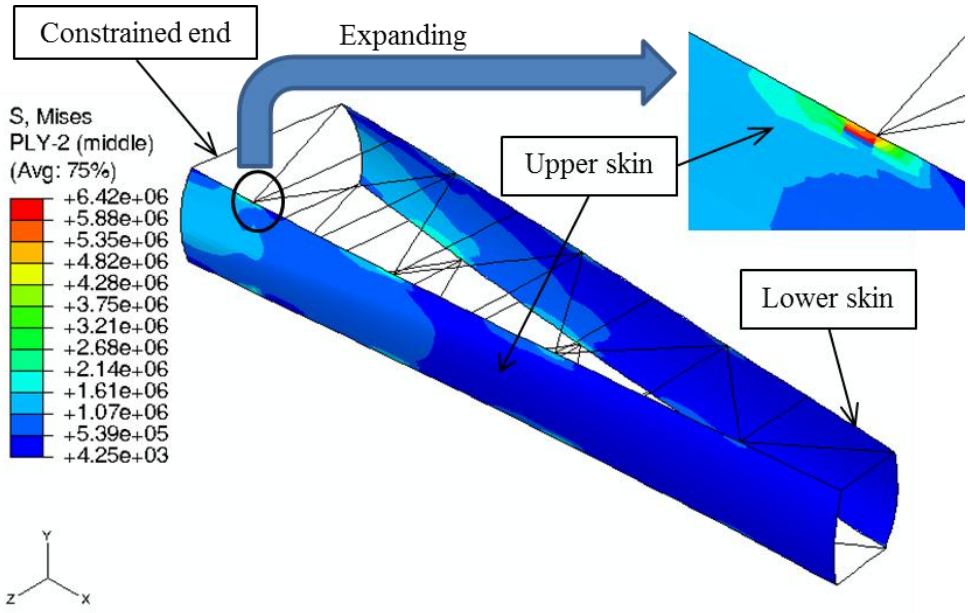

Figure E.9. Von Mises stress contour in the balsa core of the skin in Model-IIA (L_d/L_a = 0.6).

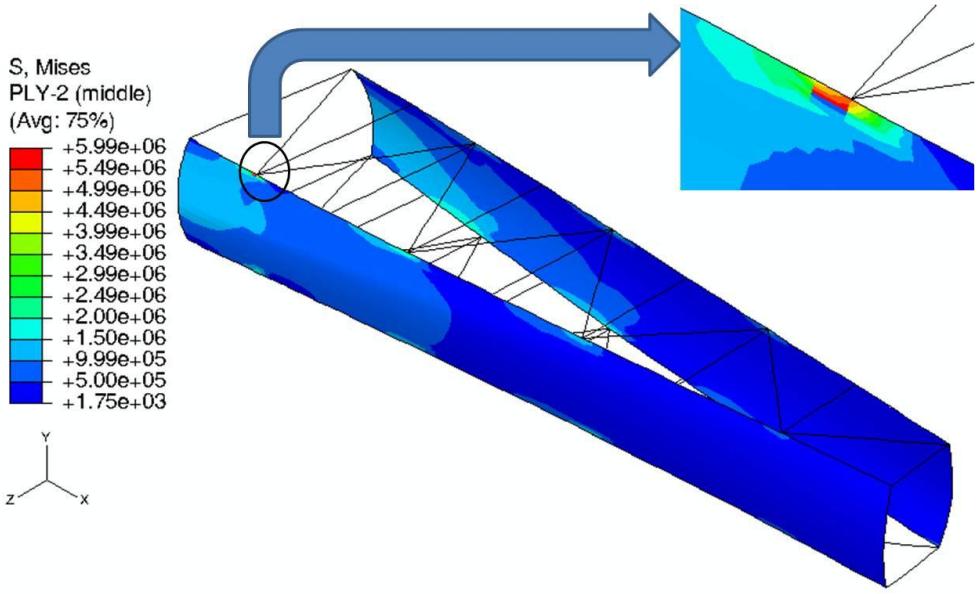

Figure E.10. Von Mises stress contour in the balsa core of the skin in Model-IIB (L_d/L_a = 0.55).

Von Mises stress contour in the balsa core of Model-IIA is presented in Figure E.9. Note that the stress concentration occurs at the nodes where the tubulars are attached to the skin. The von Mises stresses of the balsa core locally exceeded its allowable strength at these locations. The other areas on the skin, away from the attachment nodes, experience much lower von Mises stresses. The higher von Mises stress at the joints appear close to the constrained edges since the maximum reaction moments are generated at the constrained edges. The von Mises stress state of the balsa core mentioned above is demonstrated in Model-IIB, and presented in Figure E.10. The damage of the balsa core of the skin in Model-IIB is initiated under the loads which are lower in their magnitude than Model-IIA.

S11 and S12 stress contours in the balsa and in the tubes for Model-IIA and Model-IIB are shown in Figures E.11 and E.12, respectively. The stresses in the tubes for the models, as observed in the above figures, show that the tubes of both models experience much higher S11 stresses than S12 stresses. The diagonal tubes are subjected to more stress than horizontal tubes. In diagonal tubes, tensile and compressive stresses are alternatively experienced (Figures E.11 and E.12). This is dependent on the loading direction and tube orientation. For example, in Figure E.11(a), the first diagonal tube from the constrained end experiences tension, because the model bends along the positive Z-axis. This causes the first tube to stretch. Conversely, the orientation of the second diagonal tube ensures that, on the bending of the model, it undergoes compression. Material with higher strength is preferable for diagonal tubes in the tubular truss model. The maximum axial stresses in tubes of Model-II and Model-III are found

to be 19.7 MPa and 18.2 MPa, respectively. The tubes located near the constrained end sustain greater stresses than tubulars near the free end. The tubulars are connected to the innermost layer of the upper skin, this leads to higher stresses at the innermost layer.

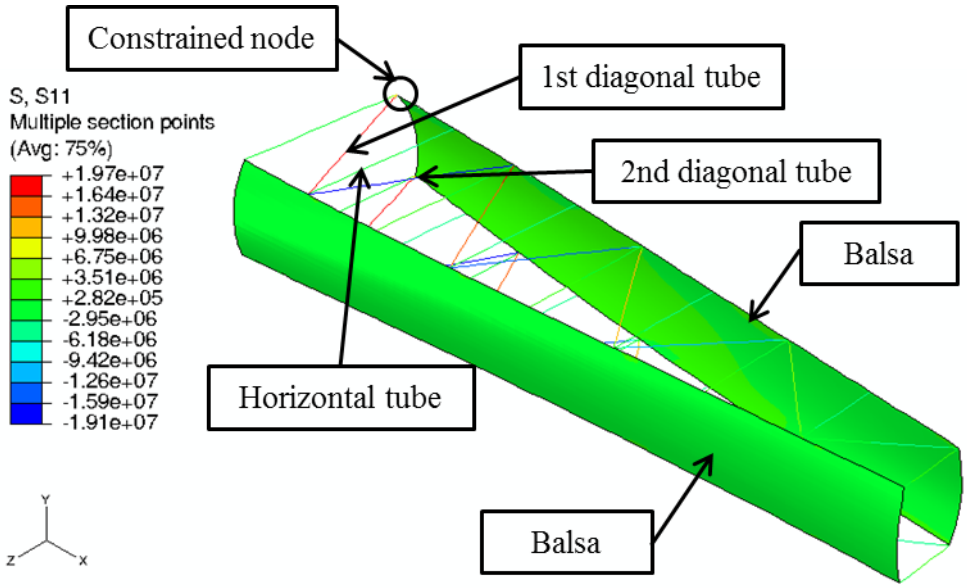

(a)

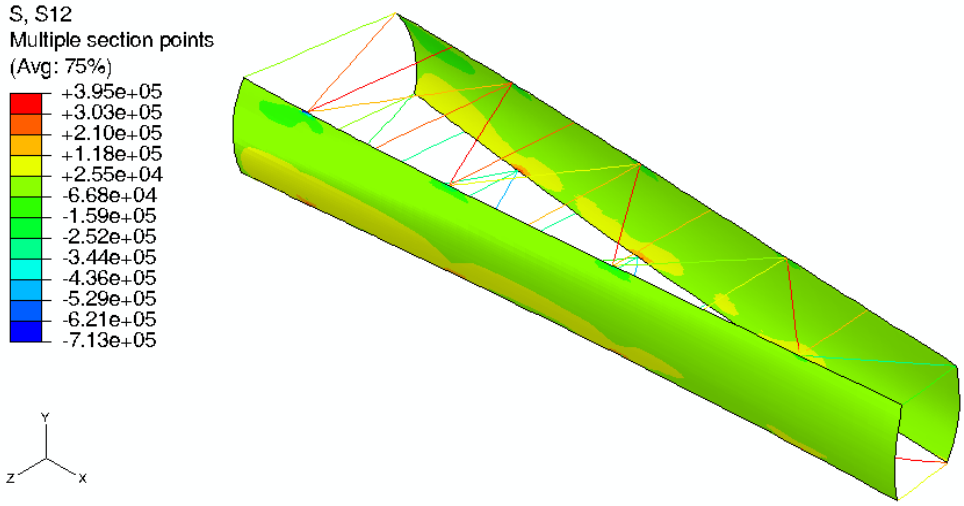

(b)

Figure E.11. Stress contours in the balsa in the tubes for Model-IIA: (a) S11 contour, and (b) S12 contours ($L_d/L_a = 0.6$).

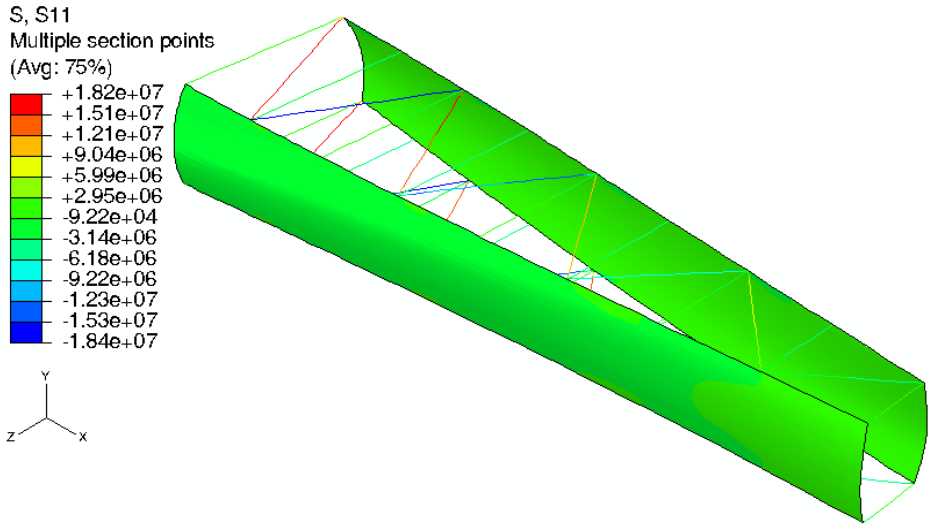

(a)

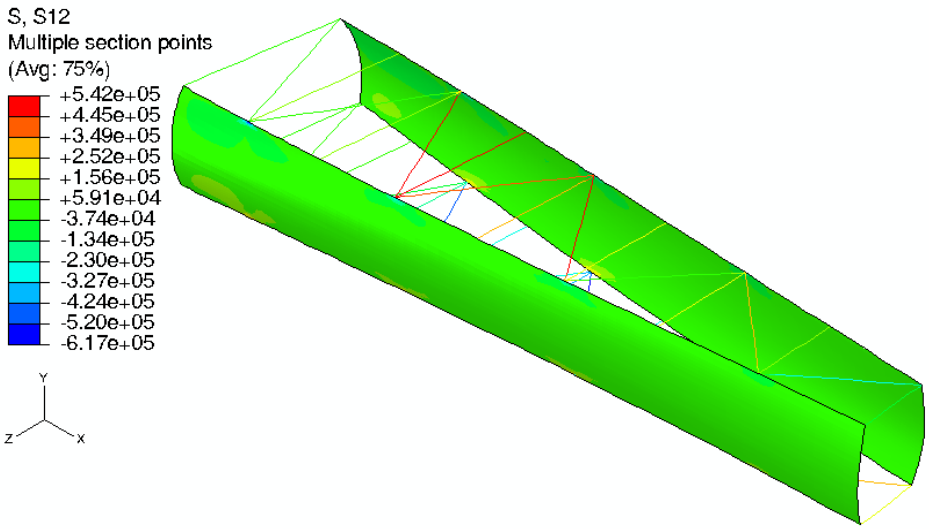

(b)

Figure E.12. Stress contours in the balsa and in the tubes for Model-IIB: (a) S11 contour, and (b) S12 contours ($L_d/L_a = 0.55$).

E.2.4 Natural Frequency response of Model-II

The first mode natural frequencies of Model-II and Model-III are presented in Figure E.13, and the corresponding mode shapes are shown in Figure E.14. Note that mode shapes in Figure E.14 are normalized.

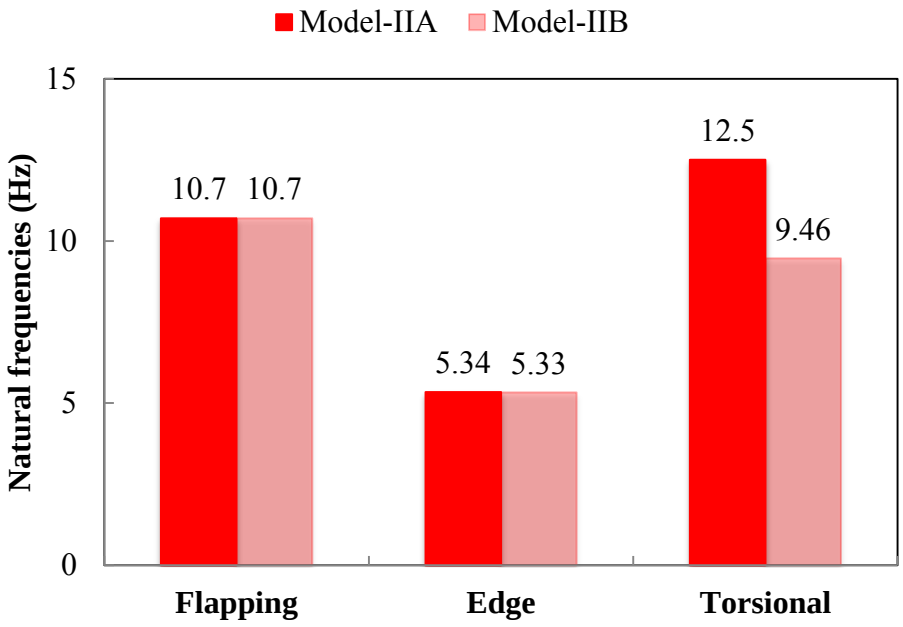

Table E.13. First mode natural frequencies in Model-IIA and Model-IIB.

The lowest natural frequency in the tubular truss models appears in the edge direction (Y-axis) since the entire structure of the tubular configuration has the lowest stiffness and inertia properties in that direction. Even though the flapping and edge natural frequency in the both models are similar, Model-IIA has higher torsional frequency. In Figure E.14(b), the model is deflected negatively in the flapping direction

(the Z-axis), and tubes in Model-III are abnormally deformed. Tubes in Model-IIB have lower moment of inertia about their central axes compared to tubes in Model-IIA. It is observed that the torsional natural frequency in Model-IIA is higher than in Model-IIB. Consequently, tubes in Model-IIA are better than tubes in Model-IIB since abnormal deformation of tubes is generated in the flapping mode shape in Model-IIB.

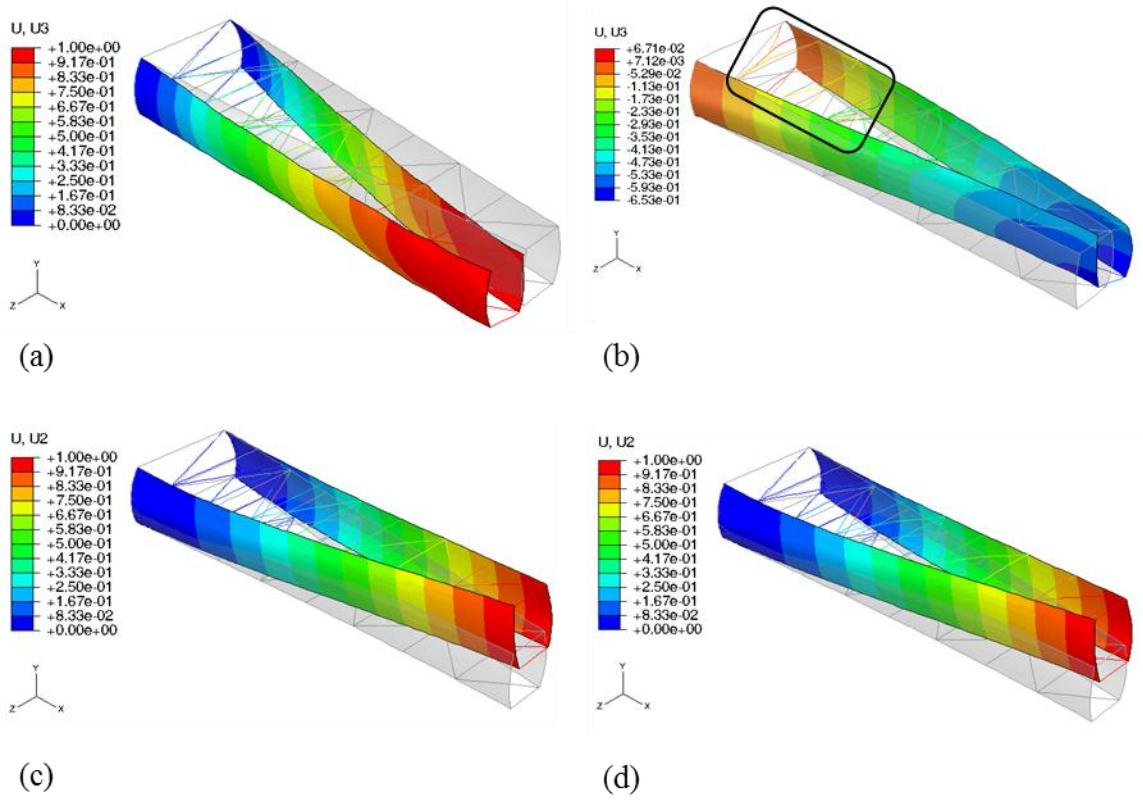

Figure E.14. First mode shapes in Model-IIA and Model-IIB: (a) flapping in Model-IIA, (b) flapping in Model-IIB, (c) edge in Model-IIA, (d) edge in Model-IIB, (e) torsional in Model-IIA, and (f) torsional in Model-IIB.

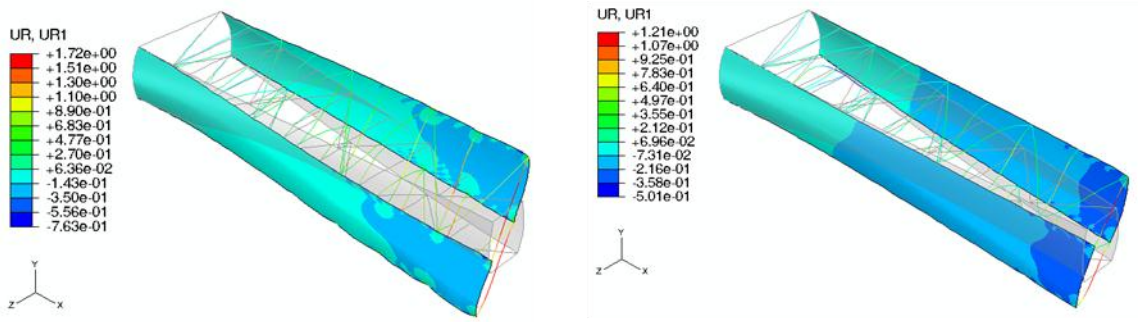

(e) (f)

Figure E.14. Continued.

APPENDIX F

The closed-form solutions to tip displacements and natural frequencies of the blade with isotropic material (Al2024) are performed based on its equivalent cantilever beam model [51,55].

When the uniformly distributed load (P) is applied to the cantilever, the tip displacement (w_{tip}) is given by

$$w_{tip} = \frac{PL^4}{8EI} \tag{F.1}$$

where E denotes Young's modulus; I, area moment of inertia; L, the cantilever beam length.

The governing equation for transverse free vibration of a cantilever beam is given by

$$\rho A \frac{\partial^2 w}{\partial t^2} + \frac{\partial^2}{\partial x^2}\left(EI \frac{\partial^2 w}{\partial x^2} \right) = 0 \tag{F.2}$$

where ρ denotes density; A, the cross-sectional area; w, the transverse deflection.

When the Young's modulus and area moment of inertia are uniform, natural frequencies of the vibration is given by

$$\omega_n = \left(\frac{n\pi}{L} \right)^2 \sqrt{\frac{EI}{\rho A}} \tag{F.3}$$

where L denotes the cantilever beam length; $n = 1,2,\cdots \infty$.

The area moments of inertia of the blade at locations along the blade length are obtained from Solidworks or bending rigidity distributions of the blade. The area moments of inertia are averaged to find uniform area moments of inertia for the cantilever. Since the surface forces are used in the static analyses, they are converted to a distributed line load. Therefore, the tip displacement and natural frequencies are analytically calculated to verify computational procedure.

VITA

Norimichi Nanami received his Bachelor of Engineering degree from Nihon University in March, 2007. He was also awarded an Honor Graduate of Nihon University and Hatakeyama Prize of the Japan Society of Mechanical Engineers in 2007. He enrolled the English Language Institute (ELI) at Texas A&M University between the summer of 2007 and the spring of 2008. Afterward, he entered the Department of Mechanical Engineering at Texas A&M University in May, 2008, and began research with Dr. Ozden Ochoa to pursue his Master of Science degree in Mechanical Engineering. He completed his Master's degree in December 2010. After his graduation, he plans to continue working with Dr. Ozden Ochoa to pursue Ph.D degree at Texas A&M University.

Norimichi may be reached at jhonn-2@tamu.edu or through Dr. Ozden Ochoa, Department of Mechanical Engineering, 3123 TAMU, College Station, TX 77843, USA.